Surface Force Measurement at High Hydrostatic Pressure

Dissertation

zur Erlangung des Grades
„Doktor
der Naturwissenschaften“
am Fachbereich Physik, Mathematik und Informatik
der Johannes Gutenberg-Universität
in Mainz

Dominik Waldemar Pilat
geboren in Frankfurt am Main

Mainz, den 30. Mai 2016

Tag der Prüfung: 06.12.2016

"If I have seen further, it is by standing on the shoulders of giants."

Isaac Newton

Contents

Nomenclature

ϵ	Dielectric constant, page 77
ϵ_0	Vacuum permittivity, page 77
η	Dynamic viscosity, page 44
λ	Wavelength, page 11
$\lambda_\mathrm{B}(D)$	Wall-correction factor of the Stokes equation, page 45
λ_D	Debye length, page 14
ψ_0	Surface potential, page 77
σ_s	Surface charge density, page 78
τ	Sampling time, page 68
$\vec{F}_\mathrm{gr}$	Gradient force, page 12
c_0	Salt concentration, page 36
c_i	Concentration of i-th ion sort, page 78
D	Distance between bead and wall, page 14
D_eq	Equilibrium distance, page 15
e	Elementary charge, page 77
F_bead	Force pushing the bead against the wall, page 15
F_b	Buoyancy, page 15
F_DL	Electrostatic double-layer force, page 13

Zusammenfassung

Unter Normalbedingungen sind Oberflächenkräfte weitgehend verstanden. Es besteht jedoch kaum Wissen über Oberflächenkräfte bei Hochdruck. Dies ist hauptsächlich darauf zurückzuführen, dass aufgrund von technischen Schwierigkeiten, die mit der Erzeugung von Hochdruck einhergehen, kein geeignetes Messgerät vorhanden ist. Es existiert jedoch eine Vielzahl von Systemen, in denen Oberflächenkräfte relevant sind, die in Umgebungen mit hohem Druck vorkommen. Solche Umgebungen sind z. B. die Tiefsee oder Bohrlöcher bei der Ölgewinnung. Es ist daher erstrebenswert, das wissenschaftliche Gebiet der Oberflächenkräfte bei Hochdruck experimentell zu erschließen.

Im Rahmen der vorliegenden Arbeit habe ich ein wissenschaftliches Messgerät entwickelt um Oberflächenkräfte bei Hochdruck zu messen. Das Messgerät setzt sich aus einer optischen Falle, einem Interferometer und einer optischen Hochdruckzelle zusammen. Oberflächenkräfte wurden gemessen zwischen einer Glaswand und einer kolloidalen Glaskugel in wässrigen Lösungen. Die Kugel wurde mittels optischer Falle gegen die Wand gedrückt. Der Abstand zwischen Kugel und Wand wurde anhand der Interferenz von Reflektionen an Kugel und Wand bestimmt. Das System aus Kugel, Wand und Probenflüssigkeit befand sich in der optischen Hochdruckzelle, welche die Erzeugung von Drücken bis zu 1 kbar ermöglichte. Dies entspricht dem höchsten Druck in der Tiefsee.

Das Messgerät wurde zur Untersuchung der Druckabhängigkeit der Kraft zwischen zwei Oberflächen angewendet, deren elektrochemische Doppelschichten überlappen, engl.: electrostatic double-layer force. Kraft-Abstands-Kurven wurden mit Subnanometer Abstandsauflösung und maximalen Kräften in der Größenordnung von 0,1 nN aufgenommen. Es konnte nachgewiesen werden, dass Druckänderungen die gemessene Wechselwirkung nur geringfügig beeinflussen. Die druckabhängigen Änderungen konnten mithilfe der Druckabhängigkeit der Permittivität von Wasser erklärt werden. Weitere mögliche druckbedingte Änderungen der Wechselwirkung, z. B. durch eine Änderung des ζ-potentials der elektrochemischen Doppelschichten konnten ausgeschlos-

sen werden. Die Messung von nur geringfügigen und erklärbaren Druckeffekten belegt die Zuverlässigkeit des Messgeräts bei Hochdruck.

Des Weiteren wurde die brownsche Bewegung der Kugel in der Nähe der Wand untersucht. Es konnte gezeigt werden, dass mit dem hier entwickelten Messgerät die brownsche Bewegung kolloidaler Kugeln bei Hochdruck mit Nanometer-Abstandsauflösung untersucht werden kann. Diese einzigartige Fähigkeit bietet die Möglichkeit eine Vielzahl von Wechselwirkungen bei Hochdruck zu untersuchen und insbesondere die Kraftauflösung bis auf Femtonewton zu verbessern.

Die hier erzielten Ergebnisse demonstrieren, dass das entwickelte Messgerät ein geeignetes Werkzeug zur Untersuchung von Oberflächenkräften bei Hochdruck ist. Das Messgerät ist auf eine Vielzahl von Wechselwirkungen anwendbar und wird in Zukunft mit Sicherheit unser Verständnis kolloidaler Systeme bei Hochdruck erweitern.

Abstract

Surface forces are well understood at standard ambient conditions, but there is very little understanding about surface forces at high hydrostatic pressure. The main cause for the lack of understanding is the absence of a proper tool, most likely due to technical difficulties associated with high pressure. However, many systems that are dominated by surface forces occur in high pressure environments. Such environments are e.g. the deep sea or bore holes for oil recovery. Thus, it is desirable to open up the research field of surface forces at high pressure to experimental investigation.

In this work I developed a scientific instrument for surface force measurement at high hydrostatic pressure. The instrument is a combination of a long-working-distance optical trap, an interferometer and an optical high-pressure cell. Surface forces were measured between a glass wall and a colloidal glass bead in aqueous solutions. The bead was pushed against the wall by the optical trap. The distance between bead and wall was determined by evaluation of the reflection interference between bead and wall. The entire system was placed inside the optical high-pressure cell that allowed for the realization of up to 1 kbar of pressure, which corresponds to the highest pressure encountered in the deep sea.

The instrument was applied to the investigation of the pressure dependence of the electrostatic double-layer force. Force-distance curves were recorded with sub-nanometer distance resolution and a maximum force of the order of 0.1 nN. It could be shown that the effect of pressure on characteristics of the electrostatic double-layer force is minor. The pressure effect could be traced back to the pressure dependence of the dielectric constant of water. Other pressure effects, e.g. due to a change in the ζ-potentials of the electric double-layers were excluded. The observation of only minor and explainable changes in the recorded force curves with pressure demonstrates that the instrument works reliably at high pressure.

Furthermore, the thermal motion of the bead close to the wall was investigated. It was found that the thermal motion of a colloidal bead can be recorded with nanometer resolution at high pressure with the developed instrument. This unique capability gives the possibility for widening the range of interactions that can be studied at high pressure and improving the force resolution to the order of femtonewton.

The results demonstrate that the developed instrument is a suitable tool for the investigation of surface forces at high hydrostatic pressure. The instrument is applicable to a multitude of interactions and will certainly deepen our understandings of colloidal systems in high pressure environments.

1 Introduction

The concept of forces is one of the fundamental and most general concepts in physics. In real life, anything that moves does it owing to forces. Anything that stands still does it owing to forces. Forces can be categorized by the length-scales on which they are relevant. For example, on the microscopic length-scale, i.e. dimensions smaller than a nanometer, as in the case of atoms and small molecules like e.g. hydrogen, the relevant forces are three of the four fundamental forces of nature, i.e. the electromagnetic, the weak nuclear and the strong nuclear force. The fourth fundamental force, i.e. gravity, is negligible on the microscopic lengths-scale. However, gravity is relevant on the macroscopic length-scale, i.e. dimensions larger than a few micrometers. Relevant forces on this length-scale furthermore include frictional and inertial forces.

Surface forces are the forces relevant on the length-scale "in between" the micro- and the macroscopic length-scale, i.e. the *mesoscopic* length-scale. Hans-Jürgen Butt and Michael Kappl pragmatically define surface forces as

> "all forces that are relevant in systems, that have a small characteristic length scale, and whose structure and dynamics are dominated by interfaces rather than gravitation and inertia." [BK10]

Here, "small" denotes dimensions in the order of nanometers up to micrometers. Systems dominated by surface forces are very common in every day life, e.g. milk [FM06] or blood [FCBC11]. Milk is an emulsion, where micrometer-sized liquid milk fat globules are dispersed in liquid skim-milk. The surface force stabilizing the globules is steric repusion [FM06]. Blood is a sol, where among others micrometer-sized solid red blood cells are dispersed in liquid blood plasma. The blood cells are stabilized by repulsive electrostatic forces [FCBC11]. The general term of such two-phase systems, "in which one phase has dimensions in the order of 1 nm to 1 μm" [BK10] is *colloidal system*, or simply *colloid*.

Multiple methods enable the investigation of surface forces. With the surface force apparatus, surface forces can be measured between two macroscopic surfaces [TS69; IT72]. The colloidal probe technique allows for the measurement of forces between the surface of a colloidal bead that is attached to a scanning probe microscopy cantilever pushed against another surface [But91b; DSP91]. By using total internal reflection microscopy the contactless measurement of surface forces between a colloidal bead and a wall is possible [PLL87]. Optical trapping techniques allow to conduct force measurements between colloidal particles using focused laser light [Ash70; Gri97].

Surface forces are studied for nearly one century, and nowadays surface forces are well understood at standard ambient conditions [BK10; Isr11]. In particular, almost all studies of surface forces were performed at hydrostatic pressures not larger than atmospheric pressure.

The pressure p is defined as a force F acting perpendicular over an area A, i.e.

$$p := \frac{F}{A} \,. \tag{1.1}$$

The term *hydrostatic pressure* is used for isotropic pressure, i.e. pressure that could be caused by placing the system under investigation at a certain depth of a column of water. The SI-unit of pressure is pascal ($1\,\mathrm{Pa} = 1\,\mathrm{N\,m^{-2}}$). The most commonly used metric unit is bar, i.e. $1\,\mathrm{bar} = 10^5\,\mathrm{Pa}$. The use of this unit is convenient, since 1 bar is approximately atmospheric pressure.

Many colloids are present in high-pressure environments. Approximately 70.9 % of the surface of the earth is covered with water [Wor]. The oceans have an average depth of 3.8 km, corresponding to an average hydrostatic pressure of 380 bar [Moz+96]. The deepest part of the oceans is the Mariana Trench, with a depth of 10 924 m [Wor]. Thus, the water covered surface of earth is a high pressure environment where the hydrostatic pressure reaches up to 1.1 kbar, i.e. three orders of magnitude higher than atmospheric pressure.

One colloidal system present in the oceans is colloidal organic carbon [WG91; WG93; WG94], which is "one of the largest reservoirs of organic carbon on the planet" [Kep94]. Wells and Goldberg have investigated the removal of colloidal organic carbon from

bulk sea water at a depth of up to 5 km, which corresponds to a hydrostatic pressure of 0.5 kbar [WG93]. They found that the removal of colloidal organic carbon from bulk seawater mainly takes place by aggregation into larger colloids followed by sedimentation of the larger colloids to the sea floor. From the structure of the aggregates the authors concluded that there was a repulsive force between the colloids that needed to be overcome in order to form aggregates. Ultimately, the strength of this repulsive force determines the removal rate.

Furthermore, the deep sea is home to multiple living organisms, e.g. marine fish [Yan+14]. The stability of proteins in aqueous solutions depends on surface forces [Chi+03]. It is known that the structure of proteins is affected by hydrostatic pressure of the order of 1 kbar [Moz+96].

High hydrostatic pressure also occurs during oil recovery. For example, drilling muds are used for lubrication and cooling of drill bits [Bri]. For more than a decade, the rheology of water-based drilling muds at down-hole conditions, i.e. hydrostatic pressure up to 1 kbar, has been under investigation [Ald+88]. Drilling muds are suspensions of e.g. charged, micrometer-sized clay platelets in water. The rheology of suspensions is determined by the interactions of the individual particles [ZSB01].

In order to gain a fundamental understanding of the structure and dynamics of drilling muds, deep-sea animal cells or marine colloids, surface forces at high hydrostatic pressure need to be investigated. However, until now there was no instrument that allowed the measurement of surface forces at hydrostatic pressures up to 1 kbar.

To the best of my knowledge, the only direct measurements of surface forces at high hydrostatic pressure were reported by Schurtenberger and Heuberger [SH11; SH12]. The authors used an extended surface force apparatus enclosed in an autoclave. Here, the force between two macroscopic mica surfaces was measured in an environment of pressurized carbon dioxide. The authors investigated the critical Casimir effect along the supercritical pressure-temperature ridge of carbon dioxide [SH12]. The authors reported on multiple technical difficulties: Since the mica surfaces were in mechanical contact with metal and glass parts, due to deformation of these parts the surface separation changed with the pressure inside the autoclave by more than $10\,\mathrm{nm\,bar^{-1}}$ [SH11]. In order to effectively measure surface forces, the pressure drift in the autoclave was

reduced to less than 2 mbar h^{-1}. Durations for equilibration after pressurization between 10 h and two weeks were reported [SH11; SH12]. Since the autoclave was filled with the fluid under investigation, the authors reported on an extensive cleaning procedure before each experiment. Finally, the pressure range accessible with the method was limited to a maximum pressure of 170 bar, which is nearly one order of magnitude smaller than the largest hydrostatic pressure that occurs on the surface of our planet.

Thus, the research field of surface forces at high hydrostatic pressure is practically unexplored. The reason for this seems to be the lack of scientific instruments, most likely due to the technical difficulties involved with high pressure experiments. The only existing instrument poses several operational challenges and has a limited pressure range.

The aim of this work was to open up the research field of surface forces at high hydrostatic pressure to experimental investigation. Thus, a new scientific instrument was developed.

In order to find a suitable realization of a high hydrostatic pressure environment for surface force measurements, it is beneficial to take a look at existing solutions from fields of research where instruments for measurements at high hydrostatic pressure are well established. For the investigations of biological samples at pressures of the order of 1 kbar, the use of optical high-pressure cells is common [Vas+10]. Such cells allow for light to be transmitted through a small (mostly smaller than 1 ml) pressurized sample volume. For investigations of matter at ultra-high pressures, i.e. up to 1 Mbar, mostly optical diamond anvil cells are used [Lov12]. Optical high-pressure cells are for example used for experiments with light microscopy [Rec+98; DT02; Har+03; Rab+06; MDT06; Vas+10; Bao+10; DB11; KC12; Vas+13], X-ray reflectivity [Wir+14] or dynamic light scattering [ADT01; Deg+06].

As mentioned above, optical trapping techniques allow for the investigation of forces between colloidal particles using light [Gri97]. A purely optical technique for surface force measurement would allow the use of optical high-pressure cells without modification. The most common and commercially available optical trapping technique is a "single-beam gradient force optical trap" [Ash+86], generally referred to as *optical tweezers*. Since most optical trapping literature deals with optical tweezers, I will explain the principles of optical trapping with regard to this technique and then distinguish the

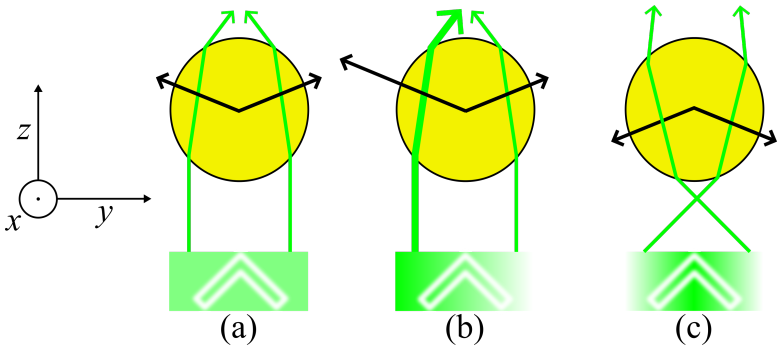

Figure 1.1: Forces exerted on a bead by a laser beam. White arrows denote direction of beam propagation. Green lines are exemplary rays. Black arrows are corresponding forces on the bead. Figure based on [NB04].

optical trapping technique used in this work. A single laser beam, commonly with Gaussian TEM_{00}-profile is tightly focused by a high-numerical-aperture objective (typically NA = 1.2 − 1.4) [NB04; Ash+86]. The description of the optical forces on a bead with radius R depends on the relation of bead radius to the wavelength λ of the laser light [NB04; MP02]. For $R << \lambda$, the conditions for Raleigh scattering are satisfied. For $R >> \lambda$ the optical forces can be described by a ray optics approach. In case of $R \approx \lambda$, neither description of the optical forces is correct [NB04], but a more rigorous approach is needed [RGG94]. In this work, R was larger than λ by approximately one order of magnitude.

Regardless of its justification, the ray optics approach is very instructive: Let's consider a dielectric bead whose refractive index n_{bead} is larger than the refractive index n_{medium} of the medium surrounding it, illuminated by a laser beam of uniform intensity profile (fig. 1.1 (a)). When a single ray passes the bead off-center, it will be refracted towards the center of the bead when it enters and exits the bead, since $n_{\text{bead}} > n_{\text{medium}}$. Due to refraction, the momentum of the photons is changed and, consequently, the momentum of the bead is changed to the opposite direction. Many photons are refracted by the bead over time, giving rise to a force exerted on the bead (black arrows in fig. 1.1 (a)).

The amount of photons interacting with the bead is the same for the left and the right side of the bead, resulting in a cancellation of the lateral components (x and y) of the force. The remaining force acts on the bead in direction of beam propagation (z-direction). This force is referred to as radiation pressure force F_{rp}. The radiation pressure force is proportional to the number of photons that are refracted by the bead, and thus it is proportional to the power of the laser beam P [NB04]

$$F_{\text{rp}} \propto P \, . \tag{1.2}$$

Let us now consider a laser beam profile with an intensity gradient (fig. 1.1 (b)). Here, more photons are refracted by the bead on the left side. Thus, the lateral components of the force on the bead do not cancel each other out. The remaining lateral force drives the bead towards higher intensities. Since this force is caused by a gradient in the intensity of the laser beam, it is referred to as gradient force $\vec{F}_{\mathrm{gr}}$ [1]. The gradient force is proportional to the intensity gradient of the laser beam [NB04]

$$\vec{F}_{\mathrm{gr}} \propto \nabla I \, . \tag{1.3}$$

In the case of fig. 1.1 (b), there is a lateral (x-, y-direction) intensity gradient, but no intensity gradient in z-direction. Thus, $F_{\mathrm{gr,z}} = 0$.

Finally consider a tightly focused beam with Gaussian beam profile (fig. 1.1 (c)). The intensity of the beam is largest on-axis, thus any lateral displacement, e.g. in x-direction would cause a restoring force $F_{\mathrm{gr,x}}$ in the opposite direction, hence centering the bead on the beam. Due to the tight focusing, there is an additional intensity gradient in the direction of beam propagation, which results in a non-zero component of the gradient force in z-direction $F_{\mathrm{gr,z}}$ directed towards higher intensity. The bead is thus forced towards the focus of the beam.

In case $F_{\mathrm{gr,z}} < F_{\mathrm{rp}}$, the tight focusing allows for three-dimensional trapping of the bead. At the same time, the high NA needed for focusing limits the working distance, i.e. the distance between the focus of the beam and the front lens of the objective, to $\approx 0.1\,\mathrm{mm}$ [NB04]. Windows in optical high-pressure cells however are usually ticker than 1 mm [Vas+10]. Although a prototype of an optical high-pressure cell was reported, where a cover-slip with a thickness of $\approx 0.2\,\mathrm{mm}$ for a window was used at pressures up to 1.2 kbar [Vas+13], a technique that aims to be generally applicable to the use with high-pressure cells must overcome the restraint of a short working distance.

Long-working-distance optical traps precede optical tweezers by more than a decade [Ash70]. Here, a Gaussian beam is moderately focused, thus losing the intensity gradient in direction of beam propagation and yielding $F_{\mathrm{gr,z}} << F_{\mathrm{rp}}$. Hence, the bead is accelerated in direction of beam propagation by the radiation pressure force F_{rp} and

[1] Note: The underlying cause of $\vec{F}_{\mathrm{gr}}$ is as well radiation pressure. However, for reasons of clarity it is beneficial to distinguish between $\vec{F}_{\mathrm{gr}}$ and F_{rp}.

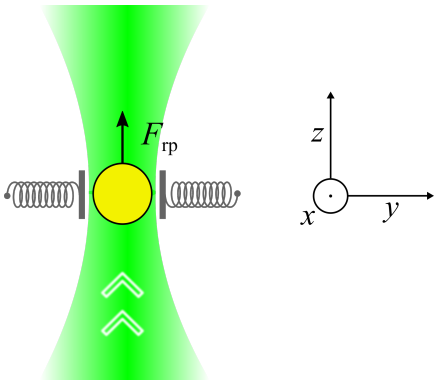

Figure 1.2: Long-working-distance optical trapping. Springs denote lateral trapping due to $\vec{F}_{gr}$.

trapped in lateral direction by the gradient force (fig. 1.2). Since the laser beam is moderately focused, working distances of the order of centimeters can be realized [AD71]. Bowman *et al.* demonstrated that long-working-distance optical trapping works effectively inside an optical high-pressure cell [Bow+13a; Bow+13b]. They used an optical trap to determine the bulk viscosity of water at hydrostatic pressures of up to 13 kbar.

1.1 Principle of Surface Force Measurement at High Hydrostatic Pressure

In this work I utilized long-working-distance optical trapping in order to perform surface force measurements inside an optical high-pressure cell. I applied this method in order to investigate one of the most common surface forces, the *electrostatic double-layer force* F_{DL}. In particular, this force is present between any charged surfaces that are immersed in aqueous solutions, including blood-cells, proteins and clay-platelets. The electrostatic double-layer force is well understood at ambient pressure, but has never directly been measured at high hydrostatic pressure. The pressure dependence of the electrostatic double-layer force between colloidal particles in hydrothermal water is subject to controversial discussion [GT08; DM09; Gho09]. Other reports, based on electrophoresis and rheology experiments indicate a substantial weakening of the electrostatic double-layer force with pressure [RA06; AOS11]. One aim of this work is to elucidate the pressure dependence of the electrostatic double-layer force.

Experiments were performed with an optical high-pressure cell that allowed for pressurization of the sample volume to a pressure of up to 1 kbar (fig. 1.3). For the separation of

the sample solution from the pressure transmitting water, a capillary capsule was developed. A rectangular glass capillary was filled with an aqueous solution with dispersed colloidal glass beads. The ends of the capillary were sealed with a highly viscous sealing paste, thus separating the pressure transmitting water from the aqueous sample solution while at the same time allowing pressure to be transmitted. Due to the rectangular shape of the the capillary the transmitted light was not distorted. The force between a colloidal glass bead and the upper inner wall of the glass capillary was measured.

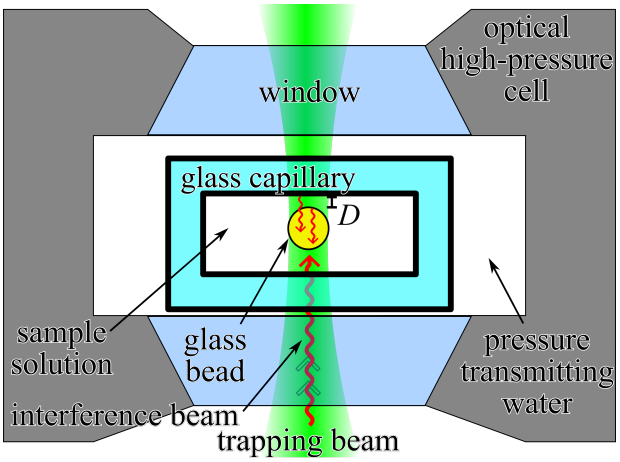

Figure 1.3: Surface force measurement inside an optical high-pressure cell. ©2016 American Physical Society [Pil+16]

Any force between two bodies depends on the distance between the bodies. For example, the force-distance dependence of the electrostatic double-layer force F_{DL} between the bead and the wall is given by

$$F_{\mathrm{DL}}(D) = F_0 \exp\left(-\frac{D}{\lambda_{\mathrm{D}}}\right). \tag{1.4}$$

The force is repulsive, since both glass surfaces are negatively charged in water [BG01; Lam+08]. The force decays exponentially with increasing distance between bead and wall D. The decay constant characteristic for the system under investigation is the *Debye length* λ_{D}. F_0 is the amplitude of the force. Equation (1.4) will be discussed in more detail in chapter 6.

Hence, forces are characterized by force-distance curves (short: force curves). The

here used method for force-distance measurements is a combination of long-working-distance optical trapping with a reflection interference technique, based on a method presented by Nadal *et al.* [Nad+01]. The reflection interference technique was used for distance measurement and is similar to reflection interference contrast microscopy [RS92; LS09]. The reflection interference measurement was realized by illumination of the sample by a laser beam (fig. 1.3, red interference beam). This beam was reflected at the surface of the bead and the capillary wall. The reflected rays interfered. The intensity of the reflection interference signal I_{RI} was a measure of D.

The bead was pushed against the wall by means of a moderately focused Gaussian beam (fig. 1.3, green trapping beam). The force pushing the bead against the wall F_{bead} was given by

$$F_{\mathrm{bead}} = -F_{\mathrm{rp}} + F_{\mathrm{g}} - F_{\mathrm{b}} \; . \tag{1.5}$$

Here F_{g} and F_{b} are gravity and buoyancy. The bead moved against the wall until F_{bead} was balanced by the electrostatic double-layer force

$$F_{\mathrm{bead}} = -F_{\mathrm{DL}}\Big(D_{\mathrm{eq}}\Big) \, , \tag{1.6}$$

where D_{eq} is the equilibrium distance. Since the radiation pressure force F_{rp} is proportional to the power of the trapping beam P, changing P allowed for probing the force-distance dependence of F_{DL}.

1.2 Outline

In **chapter 2** I will present the instrument and the experimental procedure that I developed in order to realize the above described principle of measurement. I will at first present and characterize the optical setup that consists of an optical trap, an interferometer and an inverse optical microscope. I will then discuss the optical cell that was used to realize a high-pressure environment. Furthermore, the experimental procedure developed in order to perform high-pressure experiments in a defined environment will be presented. Finally, the automated procedure of recording a force curve will be discussed and the gained data will be presented.

The **chapters 3, 4 and 5** lay the groundwork for the analysis of the experimental data. In **chapter 3** the trajectory of the bead pushed against the wall will be analyzed based on the wall-hydrodynamics between bead and wall. In particular, an appropriate analytical equation of motion will be derived and validated. By determining the hydrodynamic drag on the bead the force pushing the bead against the wall will be derived. Furthermore, by exploiting the distance dependent hydrodynamic interaction between bead and wall a calibration for the absolute distance will be obtained.

After the determination of the force pushing the bead against the wall in **chapter 3**, the following **chapter 4** deals with the analysis of this force. It will be shown, both qualitatively and quantitatively that the force pushing the bead against the wall is given by the sum of the radiation pressure force, gravity and buoyancy. Furthermore, it will be argued that effects of the non-conservatism of the radiation pressure force are negligible for the experiments performed in this thesis.

Thermal motion around the equilibrium position where the force pushing the bead against the wall is balanced by the electrostatic double-layer force necessitates a statistical treatment of the recorded bead-wall distance (**chapter 5**). An approximation of the equation of the probability density of the bead's position will be derived and validated. The statistical data analysis will be discussed and special care will be taken in order to account for instrument noise.

The two **chapters 6 and 7** present the main scientific findings of this thesis. In **chapter 6** the pressure dependence of the electrostatic double-layer force will be investigated. Experiments at ambient pressure will be discussed in order to validate the here used method for surface force measurements. It will be shown, that force curves were recorded with sub-nanometer precision. The first systematic study of the electrostatic double-layer force at different hydrostatic pressures will be presented. The observed pressure effects will be traced back to pressure induced changes of material properties. It will be shown, that with the here developed instrument precise measurements of surface forces at high hydrostatic pressures can be realized.

In order to widen the range of applicability of the here developed instrument, an alternative approach of determining surface forces is applied in **chapter 7**. The electrostatic double-layer force is derived directly from analysis of the thermal motion of the bead

around equilibrium. The gained results will be compared to results gained with the hydrodynamic approach. Differences between the two techniques will be traced back to the effect of instrument noise on the analysis of thermal motion. It will be discussed, that with the here presented instrument the analysis of the thermal motion of a colloidal bead is possible with nanometer resolution at high hydrostatic pressures.

Finally, I will present the conclusions drawn form my work in **chapter 8**. Furthermore I will give an outlook of the possible future exploration of the research field of surface forces at high pressure.

2 Instrument for Surface Force Measurement at High Hydrostatic Pressure

In this chapter the setup and experimental procedure are presented that were developed in order to realize surface force measurements at high hydrostatic pressure.

2.1 The Optical Setup

The optical setup presented here is based on the optical setup constructed by Bernard Pouligny that is located at the Centre de Recherche Paul Pascal, Pessac, France [AP93; Nad+01; Mih+12; Sur+13]. The setup consisted of a two-beam long-working-distance optical trap (2.1, green beam), an interferometer (red beam) and an inverted optical microscope (yellow beam). All components were mounted on an optical table that stood on four heavy-duty passive isolation mounts (Thorlabs, PWA075). Contrary to multiple optical trapping setups that are based on the modification of a commercial microscope [KPD06; Gri97; MP02; NB04; JZ08], the here presented setup was built from the ground up in order to ensure adaptability. An additional bread board (Thorlabs, MB6090/M) was attached vertically to the optical table (black box in fig. 2.1) and the optical components were mounted individually to this vertical breadboard.

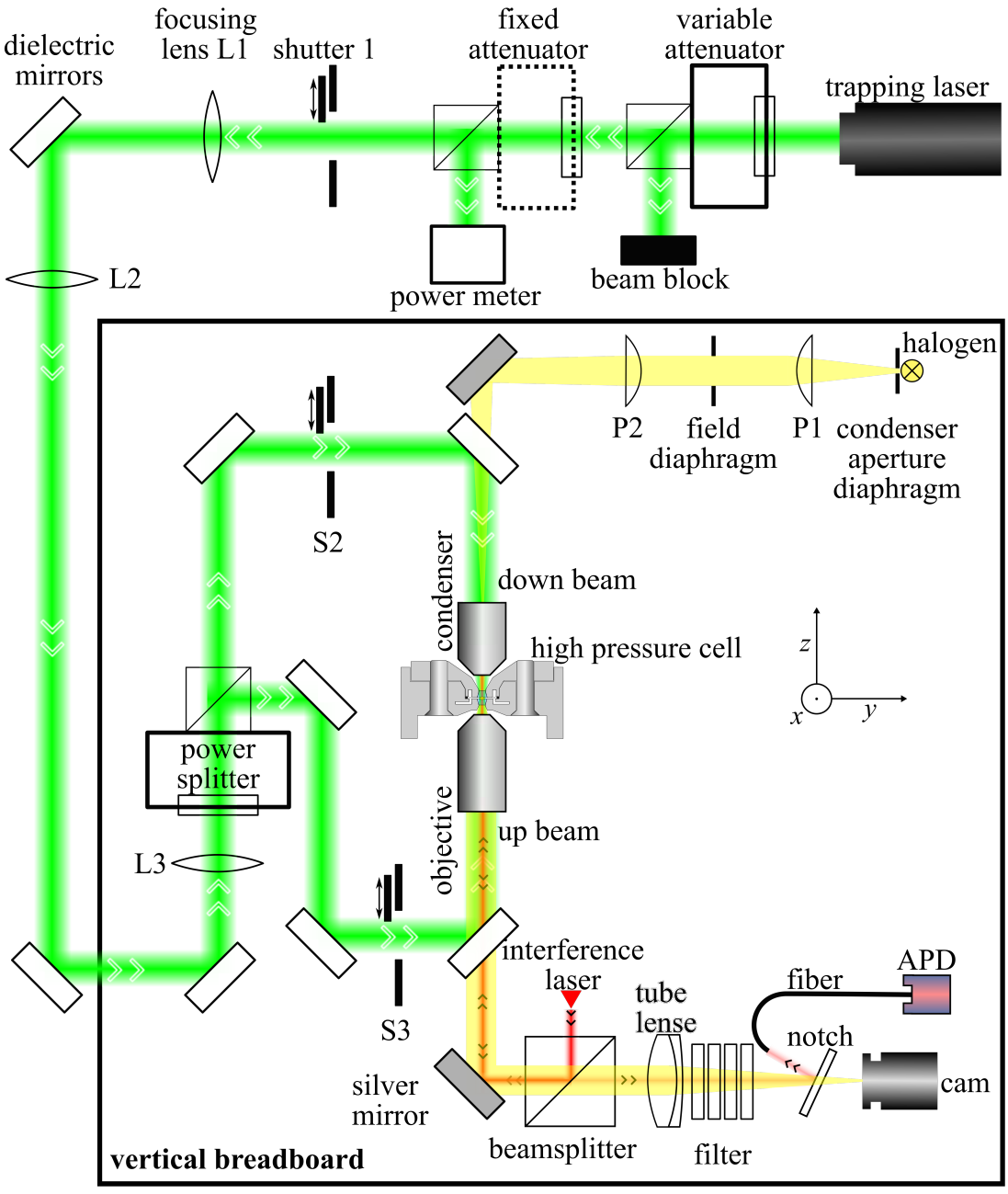

Figure 2.1: The optical setup. Green: Optical trap. Red: Interferometer. Yellow: Optical microscope. ©2016 American Physical Society [Pil+16]

2.1.1 Optical Trap

In order to effectively implement the principle of force-measurement presented in part 1.1, the optical trap needed to meet the following requirements:

1. Exert a stable and adjustable force on the bead in direction of beam propagation.
2. Trap the bead laterally to the direction of beam propagation.
3. Provide enough working-distance to fit a high-pressure cell.
4. Exert a force in both upwards and downwards direction.

Here I used a Gaussian long-working-distance optical trap, which immanently meets requirements 2 and 3. Such a trap as well exerts a force in direction of beam propagation. Requirement 1 translates into the requirement of a stable and adjustable laser power. The here presented optical trap is a two-beam optical trap (fig. 2.1, green beam). Due to the use of two counter-propagating beams requirement 4 was fulfilled. The use of a long-working-distance *objective* (Nikon, 50×, NA = 0.6, WD = 11 mm) and a long-working-distance *condenser* (Nikon, 50×, NA = 0.4, WD = 22 mm) allowed for generating two counter-propagating trapping-beams with focuses at distances > 1 cm to the optics. The distance in between the objective and the condenser was > 3 cm, which was large enough to fit the optical high-pressure cell.

The laser used to generate the trapping-beams (trapping laser) was a diode-pumped solid-state laser that provided linearly polarized light with a Gaussian beam profile (Laser Quantum, Finesse pure, wavelength $\lambda = 532\,\text{nm}$). In order to ensure high beam quality and stability, the trapping laser was always operated at a power of 3 W. The root-mean-squared (RMS) noise of the trapping beam was below 0.2 %.

The force exerted on the bead is proportional to the power of the trapping-beam. In order to vary the force on the bead, the beam power had to be made adjustable without causing changes to other beam-parameters. This was realized by using a combination of a $\lambda/2$-plate and a polarization sensitive beam-splitter cube. The linearly polarized laser beam was split into two perpendicularly polarized beams. The power ratio of the exiting beams depended on the direction of polarization of the initial beam. Thus, rotating the direction of polarization of the initial beam using a $\lambda/2$-plate allowed for adjusting the power-ratio of the exiting beams. This principle was used for the *variable attenuator*,

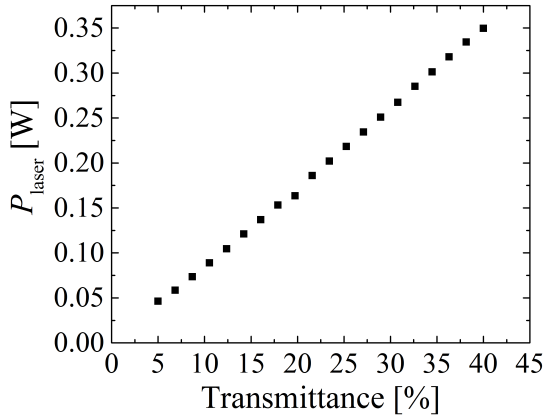

Figure 2.2: Power of the transmitted beam P_{laser} versus transmittance of the variable attenuator. At about 20 % the power meter was most likely not yet equilibrated when the power was logged, causing the outlier.

the *fixed attenuator* and the *power splitter*. The variable attenuator and the power splitter were commercially available modules that allowed for the automated rotation of the $\lambda/2$-plate (Workshop of Photonics, Motorized Standard Watt Pilot, high-power version). The variable attenuator was used for attenuation of the overall laser-beam. The reflected part was directed on a beam block. For the fixed attenuator, the $\lambda/2$-plate was adjusted to split the power in a 1 : 2-ratio. The power of the transmitted beam P_{laser} was thus limited to approximately 1 W, in order to prevent damage to the optical components or the sample. The reflected beam was directed onto a power meter (Thorlabs, PM100D with S302C thermal power sensor), allowing to monitor P_{laser} as half the measured power. P_{laser} was found proportional to the adjusted transmittance of the fixed attenuator (fig. 2.2), allowing for computer controlled adjustment of the power and thus the force on the bead. For the experiments presented in this thesis, a transmittance of 40 % was not exceeded. This means that after exiting the fixed attenuator the power of the laser beam was below 0.4 W at all times.

A shutter (fig. 2.1, shutter 1), positioned subsequent to the fixed attenuator, allowed for computer-controlled blocking of the entire trapping beam. The shutter was the only optical component that was not mounted to the optical table in order to avoid the excitations of vibrations due to the abrupt movement of the shutting-lever. Instead, the shutter was mounted to a pole that stood on the floor of the laboratory. Due to the large aperture of the shutter, the relative movement of pole and optical table had no influence on the trapping beam. For directing the trapping beam, high-power dielectric mirrors (CVI Melles Griot, Y2-1025-45P) were used. These mirrors reflected light with wavelength $\lambda = 532\,\text{nm}$ while allowing for the partial transmission of light at other wavelengths.

The beam was shaped by three convex lenses (fig. 2.1, L1 to L3). The power splitter split the beam into the (reflected) *up beam* and (transmitted) *down beam*, with an adjustable power ratio between the beams. Shutters allowed for blocking up- and down beam separately (fig. 2.1, S2 and S3). The position of the power splitter ensured equal lengths for the beam paths for up and down beam. The equal path lengths ensured that both beams were of the same shape and could thus be brought to overlap.

In the here presented experimental configuration (fig. 1.3) the up beam was used to push the bead against the wall. The radiation pressure force F_{rp} depends on the power of the trapping beam at the bead P. In order to estimate the ratio of P and the monitored power of the trapping beam after passing the fixed attenuator P_{laser}, the power of the up beam after the objective was measured (fig. 2.1). The high-pressure cell was removed and the power splitter was set to zero transmission, thus giving full power to the up beam. The power of the trapping beam was found to drop to approximately 74 % of P_{laser}. Furthermore, the power of the trapping beam was found to reduce by 15 % of P_{laser} when passing a single dry window of the high-pressure cell. Assuming the power loss due to the glass-capillary to be negligible results in the approximation

$$P \approx 74\,\% \cdot 85\,\% \cdot P_{\mathrm{laser}} \approx \frac{2}{3} P_{\mathrm{laser}} \,. \tag{2.1}$$

Beam Shape

The shape of the trapping beam has an influence on the radiation pressure force F_{rp} exerted on the bead. The radius of a circular Gaussian beam w is defined by the distance from the beam axis to where the intensity drops to $1/e^2$ of its value at the beam axis [Sel83]. The propagation of w in direction of beam propagation, i.e. z-direction, for a beam with given wavelength λ is fully characterized by the radius of the beam waist w_0, i.e. the smallest radius of the beam (fig. 2.3).

The laser can possibly heat up or damage the sample or the optics. It is thus important to choose a configuration of the optical trap that allows the operation at as low laser powers as possible. Thus, the force efficiency, i.e. the ratio of F_{rp} to P should be maximized. An instructive argumentation about the optimum beam radius w_0 relative to the bead radius R was given by Kraikivski *et al.* [KPD06]: Lets consider a Gaussian trapping beam with fixed power P illuminating a bead. In case the beam waist radius

is approximately equal to the radius of the bead, i.e. $w_0 \approx R$, a certain force F_{rp} is exerted on the bead. In case the beam is wider than the bead, i.e. $w_0 > R$, a part of the beam is not refracted by the bead and thus does not contribute to the overall F_{rp}, which results in a force on the bead that is smaller than the F_{rp} for the $w_0 \approx R$ case. In the opposite case where the bead is larger than the beam, i.e. $w_0 < R$, more of the beam intensity passes through the center of the bead than in the $w_0 \approx R$ case. Since refraction is strongest at the sides of the bead, the force on the bead for the $w_0 < R$ case is smaller than for the $w_0 \approx R$ case. It is thus evident, that the force efficiency is largest in the $w_0 \approx R$ case.

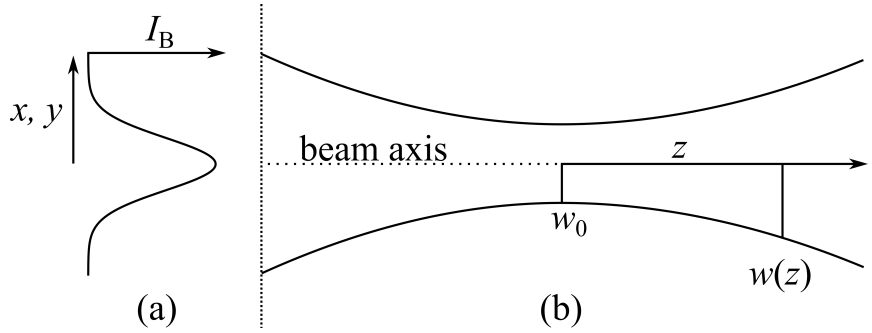

Figure 2.3: (b) Propagation of a beam with Gaussian intensity profile (a). Z is direction of beam propagation.

In my optical setup I have chosen lenses with focal lengths $f_{L1} = 200\,\text{mm}$, $f_{L2} = 150\,\text{mm}$ and $f_{L3} = 750\,\text{mm}$ for shaping the trapping beam(fig. 2.1). The lenses all were in confocal configuration with the their neighboring lenses (i.e. the distance between L1 and L2 was $f_{L1} + f_{L2}$, etc.). Lens L3 was in confocal configuration with both the objective and the condenser, since the power splitter was adjusted so that the beam path lengths of up beam and down beam were equal. The focal lengths of the objective and the condenser both were $f = 4\,\text{mm}$, corresponding to the a magnification of 50× stated by the manufacturer [GHD]. The beam waist radius of the trapping laser was approximately 1 mm. For this optical configuration the beam waist radius of both the up beam and the down beam were expected to be of the order of micrometers [Sel83]. Furthermore, the beam waist of the up beam and the down beam were expected to be located in the focal plane of the objective and the condenser, respectively.

For the measurement of the beam profile, the microscope camera was exchanged by a CCD laser beam profiler. The beam profile of the up beam was measured by blocking

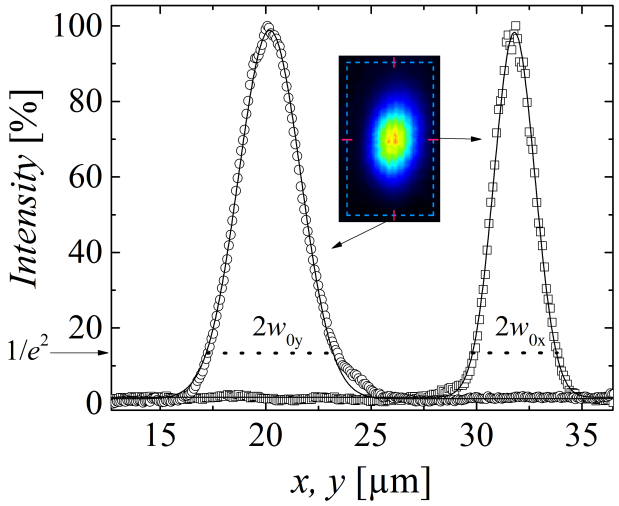

Figure 2.4: Inset: Beam profile of the up beam measured with a CCD laser beam profiler (Newport LBP-2-USB). Squares: horizontal cross section of the profile. Circles: vertical cross section. Lines are fits with a Gaussian functions. The fits revealed $w_{0x} = 1.9\,\mu m$ and $w_{0y} = 2.9\,\mu m$. The fit parameter errors were below 1 %.

the down beam and measuring the reflection of the up beam from the lower window of the high-pressure cell (fig. 2.4). The position of the cell was adjusted in z-direction until the width of the reflected beam was minimal. Three times the cell was adjusted and the profile was measured. The beam profile was approximately elliptical with half-widths of the semi-axes

$$w_{0x} = (2.0 \pm 0.1)\,\mu m \qquad w_{0y} = (2.9 \pm 0.1)\,\mu m\,, \tag{2.2}$$

which can be approximated by a mean beam waist radius of

$$w_0 = (2.4 \pm 0.4)\,\mu m\,. \tag{2.3}$$

In this work, the radii of the beads were $R \approx 4\,\mu m$, thus $w_0 \approx R$ was approximately satisfied. From w_0 we can now calculate the *Rayleigh length*, i.e. the distance z_R from the beam waist at which $w(z_R) = \sqrt{2}w_0$. For our result (2.3) we obtain

$$z_R = \frac{\pi w_0^2}{\lambda} = (35.2 \pm 11.5)\,\mu m\,. \tag{2.4}$$

This means, that the width of the beam stays constant over a range of several micrometers in direction of beam propagation.

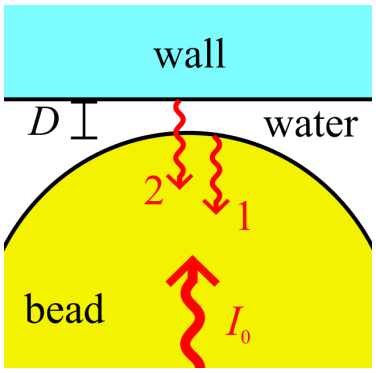

Figure 2.5: Reflection interference. The incident beam (I_0) is reflected at the bead-water interface (1) and the water-wall interface (2). The reflected rays interfere.

2.1.2 Interferometer

The distance between bead and wall was measured using interferometry (fig. 2.5). The incident *interference beam* (I_0) was reflected at the bead-water interface (1) and at the water-wall interface (2). The interference of rays 1 and 2 depends on the bead-wall distance D.

In order to realize a coherent and stable interference beam, an ultralow-noise laser-diode module (Coherent, ULN, 5 mW, λ = 635 nm) was used (fig. 2.1, interference laser). The interference beam was transmitted by the dielectric mirrors, allowing for alignment of the interference beam on to of the up beam (fig. 2.1, red beam path). Since both, trapping and interference beam were focused by the objective, their alignment relative to each other was independent of the relative alignment of the objective and the condenser. This resulted in a stable alignment of interference beam and up beam.

The reflection interference signal was collected by the objective and directed into an avalanche photo-diode (Thorlabs, APD130A/M) by a non-polarizing beam-splitter cube, a tilted Notch filter (Thorlabs, wavelength of center = 633 nm, FWHM = 25 nm) and an optical fiber (Thorlabs, M69L01, diameter = 300 µm, NA = 0.39). The beam-splitter cube allowed for separation of the beam-paths of incident interference beam and reflection interference signal. The notch filter made the separation of the reflection interference signal from the trapping beam and the microscope light possible. The notch filter was slightly tilted, which increased the center wavelength of the reflected band, thus allowing a small part of the interference signal to enter the microscope camera. Monitoring the reflection interference signal with the microscope camera enabled the alignment of the interference beam. The optical fiber was used to collect only the signal of the on-axis interference, i.e. the part of the reflection interference that corresponds to perpendicular

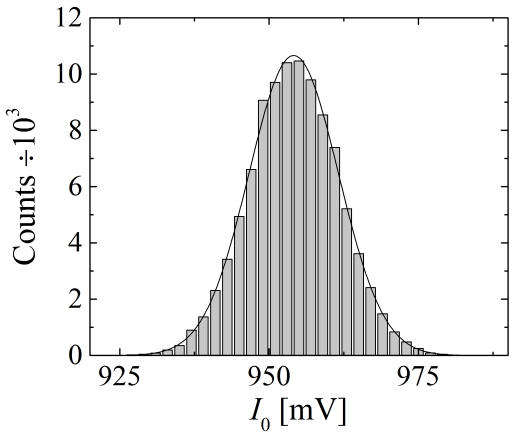

Figure 2.6: Histogram of intensities of the interference laser reflected from the lower inner wall of the capillary without a bead in the beam path. The histogram was determined by performing frequency counting on a 2 s interval of the I_0 signal with bin-size = 2 mV. The measured distribution was fitted with a Gaussian function yielding a mean intensity of $\overline{I_0}$ = 954.1 mV and a standard deviation of σ_{ln} = 7.5 mV.

reflections at the bead-apex (fig. 2.5). The intensity recorded by the avalanche photodiode is referred to as I_{RI}. A similar optical setup for the same interferometry technique was published recently by Suraniti et al. [Sur+13].

Laser Noise

In order to determine the noise in the reflection interference signal that is not due to actual movement of the bead, the intensity of I_0 reflected from the wall was measured in absence of the bead (fig. 2.6). From the measured intensity distribution it can be seen that the intensity of the interference beam can be characterized by a Gaussian distribution with a standard deviation of

$$\sigma_{\mathrm{ln}} = 0.8\,\% \cdot \overline{I_0}. \tag{2.5}$$

Here $\overline{I_0}$ is the mean intensity of the interference beam. When the interference laser was blocked, the RMS-noise dropped below 0.5 mV, which corresponds to $0.05\,\% \cdot \overline{I_0}$. The RMS-noise of the interference laser for frequencies between 10 Hz and 10 MHz was specified by the manufacturer to be less than 0.1 %. Thus, the major contributions to the measured noise originated from other sources, e.g. thermal motion or other vibrations of the optical components, which can cause or enhance beam pointing fluctuations. The optical fiber collects only a part of the reflection interference, causing spatial fluctuations to translate to fluctuations in the measured intensity.

There are very few reports of the laser noise for other experimental setups. However, the here determined laser noise falls below the laser noise reported in a recent study

where the distance between a colloidal bead and a wall was determined by total internal reflection microscopy [NAB13]. The authors reported a laser noise between 1.5 % to 5 %.

2.1.3 Optical Microscope

The illumination, the condenser, the objective, the tube lens and the camera compose an inverse optical microscope (fig. 2.1, yellow beam path). The focal length of the tube lens was 400 mm, yielding a magnification of the microscope of 400 mm/4 mm = 100×. Between tube lens and notch filter four long-pass colored glass filters (Thorlabs, FGL530, FGL550, FGL570, FGL590) were installed that suppressed light with a wavelength smaller than approximately 0.6 µm, in order to filter out the residual intensity of the trapping beam that was transmitted by the dielectric mirror closest to the silver mirror. At high powers of the trapping laser this residual light could damage the camera. The transmission at a wavelength of 532 nm varied for the different colored glass filters. Thus, by inserting appropriate combinations of the glass filters into the beam path, the residual light of the down beam could be attenuated in order to be monitored with the microscope camera or completely blocked.

The illumination of the microscope was in a Köhler-like configuration [Köh93], i.e. the image of the halogen light source (Thorlabs, OSL1) was projected onto the back-focal plane of the condenser by two plano-convex lenses (fig. 2.1). The light source was in the focus of the first plano convex lens (P1). The back-focal plane of the condenser was in the focus of the second plano-convex lens (P2). Between the plano-convex lenses the image of the light source was at infinity. Contrary to the typical Köhler configuration, the condenser aperture diaphragm was not placed in the back-focal plane of the condenser, i.e. in the plane of the image of the light source, but directly in front of the light source. This way the aperture of the light source could be adjusted without an influence on the down beam. The field diaphragm was positioned between the plano-convex lenses. The condenser aperture diaphragm was closed as much as possible, causing the light coming from the condenser to be nearly unidirectional, i.e. reducing the condenser aperture to zero. This way the depth of field was increased while trading off for lateral resolution of the microscope image [SD]. A large depth of field facilitated the selection of only a single bead, since additional beads or satellites (i.e. smaller particles) could be detected effectively without having to adjust the position of the focus. The lateral resolution d of

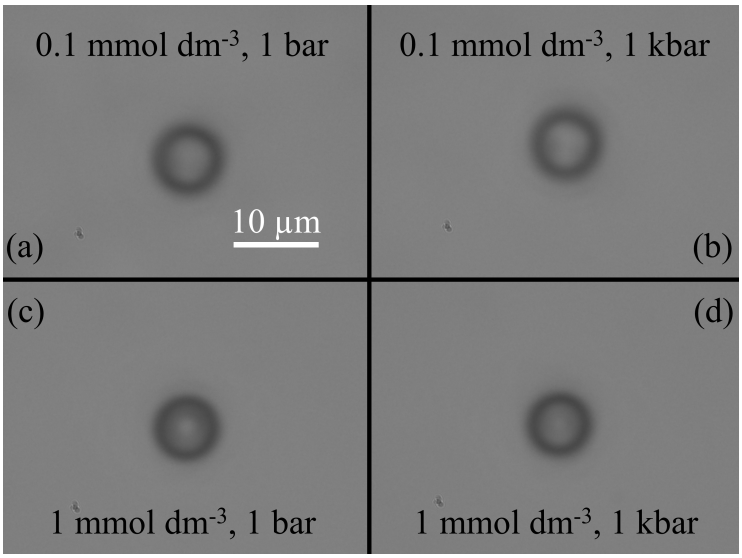

Figure 2.7: Microscope images of the two beads used for recording force curves at a salt concentration of $0.1\,\mathrm{mmol\,dm^{-3}}$ at a pressure of $p = 1\,\mathrm{bar}$ (a) and $p = 1\,\mathrm{kbar}$ (b) and at a salt concentration of $1\,\mathrm{mmol\,dm^{-3}}$ at a pressure of $p = 1\,\mathrm{bar}$ (c) and $p = 1\,\mathrm{kbar}$ (d). At a given salt concentration, the same bead was used at different pressures.

the optical microscope with a condenser numerical aperture of zero may be estimated using the Abbe formula for central illumination

$$d = \frac{\lambda_\mathrm{m}}{\mathrm{NA}_\mathrm{Objective}} \,. \tag{2.6}$$

For λ_m we can use the smallest wavelength collected by the camera. Due to the colored glass filters, $\lambda_\mathrm{m} \approx 0.6\,\mu\mathrm{m}$. For the numerical aperture of the objective $\mathrm{NA}_\mathrm{Objective} = 0.6$ (part 2.1.1) equation (2.6) yields $d \approx 1\,\mu\mathrm{m}$. The only quantity determined by optical microscopy was the radius R of the bead under investigation (fig. 2.7). The inaccuracy in determining the bead-diameter is equal to the resolution of the microscope. Thus, the inaccuracy in determining the bead radius was

$$\Delta R = \frac{d}{2} \approx 0.5\,\mu\mathrm{m} \,. \tag{2.7}$$

The application of pressure did not seem to have an influence on the microscope image (fig. 2.7).

2.2 High Pressure

2.2.1 High Pressure Cell

In order to realize optical trapping experiments at high hydrostatic pressure a compact optical high-pressure cell was needed that fit into the optical trapping setup. A cell invented by Hartmann, Pfeifer, Dornheim and Sommer (HPDS-cell) met the requirement of compactness while withstanding pressures up to 3 kbar [Har+03; HKS04]. The HPDS-cell was originally used for the investigation of biological cells by light microscopy at high hydrostatic pressure [HKS04; Fre+06]. For the work presented in this thesis a HPDS-cell was manufactured by RECORD Maschinenbau GmbH, Königsee, Germany. The cell consisted of a cylindrical main body and a lid, both made of tool steel, that were fixed by six screws (M6×20) (fig. 2.8). Two channels that exit at opposite sides of the the main body allow to fill the cell with water. For pressurization, one channel was closed by a plug and the other channel was connected to a high-pressure tube coming from the high-pressure equipment used for compression of the water.

The reason for the compact design of the HPDS-cell was a progressive metal sealing [Dor03]. At pressures below approximately 0.5 kbar, the o-ring between main body and lid sealed the cell. At higher pressures, the part of the lid that was in contact with the o-ring was pressed against the main body of the cell due to the pressure inside the cell, constituting a metal-to-metal sealing.

Two sapphire windows allowed for light to be transmitted through the center of the cell. The distance between the windows was approximately 0.4 mm. Inside this gap the sample could be placed. The entire cell was positioned in the optical setup between the objective and the condenser (fig. 2.1). The objective could be brought to a distance from the sample-volume below 7 mm due to the recess at the lower part of the main body. Thus, the use of an objective with a working distance of 11 mm allowed for the exploration of the entire sample volume without risking collisions of the objective with the high-pressure cell.

The sample liquid was encapsulated inside a rectangular glass capillary (VitroCom, VitroTubes 5010-050, borosilicate rectangular glass capillary, nominal inner dimensions $h \times w \times d = 100\,\mu m \times 1\,mm \times 8\,mm$). The ends of the capillary were sealed with high-

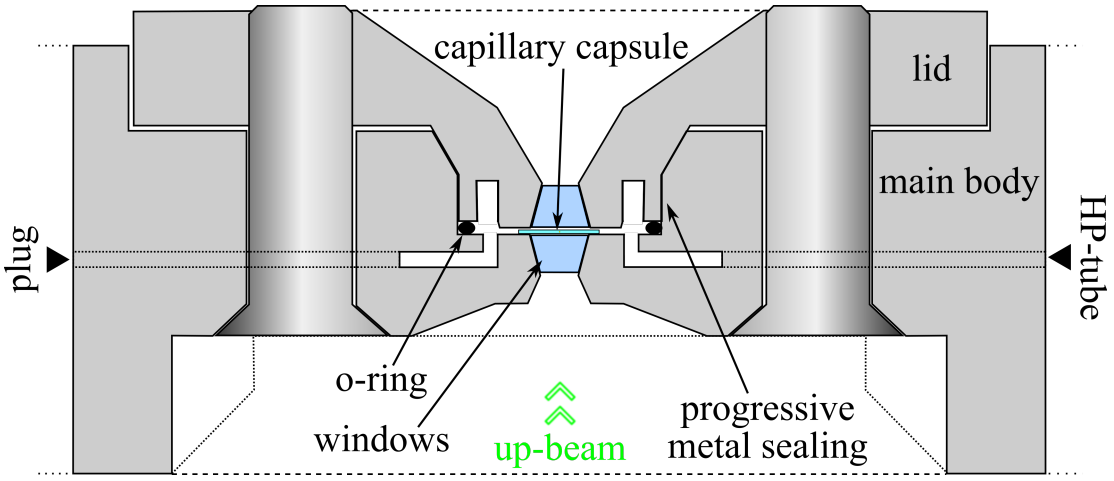

Figure 2.8: Scheme of the high-pressure optical cell. The drawing is based on the high-pressure cell described by Hartmann *et al.* [Har+03] and a technical drawing from Andreas Zumbach (RECORD Maschinenbau GmbH, Königsee, Germany). Not to scale. The main body of the cell was cylindrical with a height of 25 mm and a diameter of 85 mm. With mounted lid, the overall height of the high-pressure cell was below 3 cm. Two conical sapphire windows (thickness 2.2 mm) were fitted into the lid and the main body. The direction of the up beam is indicated for orientation.

viscosity Baysilone paste (Bayer), thus separating the sample liquid from the pressure transmitting liquid while allowing for hydrostatic pressure to be transmitted.

2.2.2 Periphery

For pressurization, the high-pressure cell was connected to the high-pressure equipment with a flexible high-pressure tube (fig. 2.9). The plug was removed. An electrical hose pump (neoLab) was used for rinsing the entire equipment with with ultrapure water from the reservoir (Sartorius Arium 611 VF purification system, MilliQ, specific resistivity of 18.2 MΩ cm) until no more air-bubbles exited the high-pressure cell. The piston screw pump (HiP High Pressure Equipment Company) was filled with water. Then, while the pump was still running, the plug was inserted into the cell, sealing the pressurized volume. The valve was then closed and the pump was turned off. The water could be pressurized up to $p = 1$ kbar using the piston screw pump . An analogue manometer (HiP High Pressure Equipment Company, accuracy 5 %) was used for monitoring the pressure inside the high-pressure equipment. For safety reasons, a burst disc was used

that caused an instantaneous pressure relaxation in case the pressure exceeded 1 kbar.

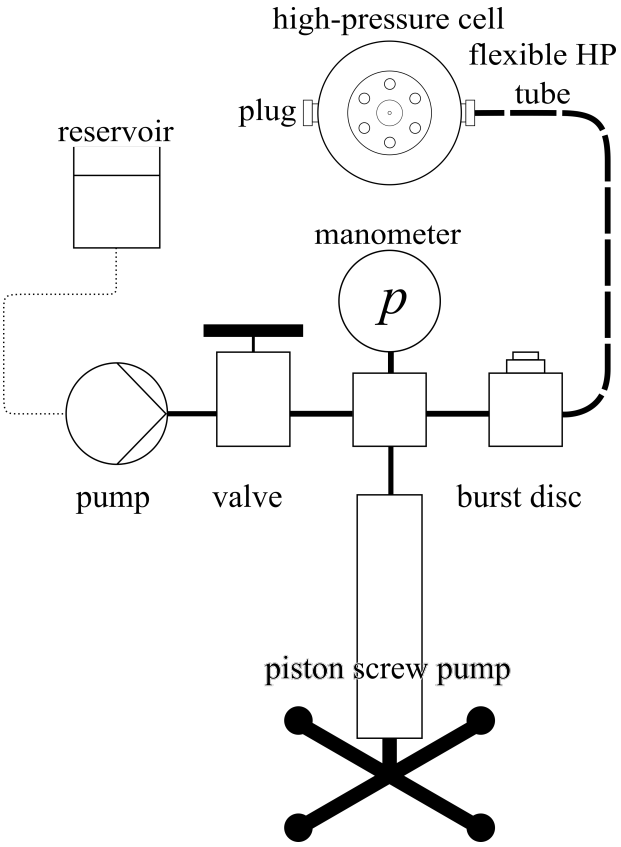

Figure 2.9: High pressure equipment.

At a pressure of 0.5 kbar the pressure reading of the manometer was approximately constant. At a pressure of 1 kbar the pressure decreased by approximately 10 bar min^{-1}.

2.3 Samples

2.3.1 Beads

The colloidal beads used for surface force measurement by optical trapping at high hydrostatic pressure had to meet the following requirements:

1. A surface charge of the same sign as the surface charge of the glass wall. Otherwise

the beads would adhere to the wall and could not be detached by means of optical trapping.

2. A refractive index n_{bead} larger than the refractive index of the liquid, i.e. water ($n_{\text{water}} \approx 1.33$). Otherwise the beads would be pushed out of the trapping beam by the gradient force instead of being centered on the beam axis.

3. No change in size in a pressure range from 1 bar to 1 kbar.

4. A weight in water not larger than a few piconewton, i.e. smaller than typical optical forces [JZ08].

5. A low surface-roughness.

Glass beads meet requirements 1 and 2. The bulk modulus K of glass is of the order of 50 GPa, which is e.g. about one order of magnitude larger than the bulk modulus of polystyrene [KL]. The isotropic change in the volume of a substance ΔV is related to the change in hydrostatic pressure Δp by

$$\frac{\Delta V}{V} K = -\Delta p \, . \tag{2.8}$$

For a sphere with radius R we use $V = 4/3 \cdot \pi R^3$ and $\Delta V = 4\pi R^2 \Delta R$, which yields

$$3\frac{\Delta R}{R} K = -\Delta p \, . \tag{2.9}$$

Thus, for a change of pressure by $\Delta p = 1\,\text{kbar} = 100\,\text{MPa}$, a relative decrease of the radius of a glass bead by

$$\frac{\Delta R}{R} = -\frac{2 \times 10^{-3}}{3} \approx -0.07\,\% \tag{2.10}$$

is expected. This means that for $R = 4\,\mu\text{m}$ a decrease of the radius by less than 3 nm is expected, which is negligible, thus satisfying requirement 3.

The roughness of several commercially available beads was studied by van Zwol *et al.* [Zwo+08]. They found that the root-mean-squared (RMS) roughness of different types of beads ranged from 0.7 nm to 40 nm, whereas some beads could not be quantified by an RMS-roughness due to their deformed shape. The lowest roughness, i.e. 0.7 nm, was reported for DUKE borosilicate microspheres type 9020. These beads had a radius of

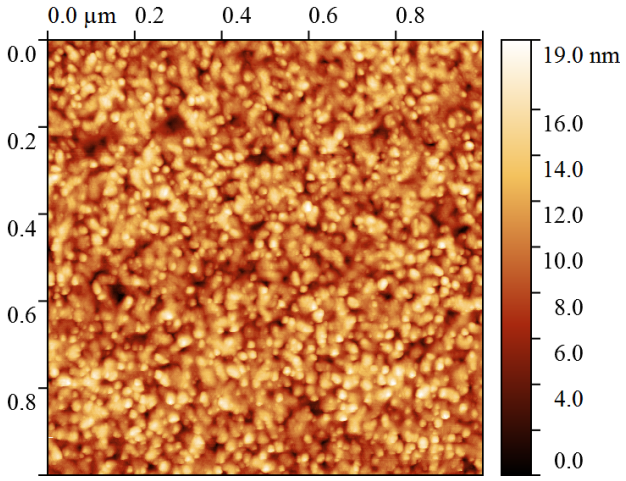

Figure 2.10: Scanning probe microscopy image of the DUKE STANDARDS borosilicate glass microspheres 9008. The height sensor topography was recorded in intermediate contact mode with a Dimension Icon FS device using an Olympus non-contact mode cantilever (OMCL-AC 240TS-W2, resonant frequency $f_0 = 70\,\mathrm{kHz}$). In order to account for the curvature of the bead, 2nd order flattening was applied to the image-data. The RMS-roughness for this measurement after flattening was $\sigma = 2.6\,\mathrm{nm}$.

$R = (10.0 \pm 0.7)\,\mu\mathrm{m}$.

In order to satisfy both requirements 4 and 5, DUKE microspheres from the 9000 series with a mean radius of $R = 4\,\mu\mathrm{m}$ were chosen (DUKE STANDARDS borosilicate glass microspheres 9008). A density of $\rho_{\mathrm{bead}} = 2.55\,\mathrm{g\,cm^{-3}}$ and a refractive index of $n_{\mathrm{bead}} = 1.56$ (at a wavelength of 589 nm) were stated by the manufacturer.

Scanning probe microscopy (SPM) measurements of four different beads of the here used type revealed a mean RMS-roughness of

$$\sigma = 3.3\,\mathrm{nm}\,. \tag{2.11}$$

Fig. 2.10 shows an exemplary SPM image for one of the beads. The measured roughness is larger than the reported value of 0.7 nm [Zwo+08]. However, the roughness of the here used beads is smaller than most roughness values reported by Van Zwol *et al.*. A comparable roughness of 5.5 nm was reported for DUKE sodalime glass 9030 beads.

Van Zwol *et al.* also reported scanning electron microscope (SEM) images of the investigated bead-types. The DUKE borosilicate glass 9020 beads appeared smooth while the DUKE sodalime glass 9030 beads had µm-sized features. SEM images of the here used DUKE borosilicate glass 9008 beads revealed similar features (fig. 2.11). Overall, the here used beads were less smooth than the ones of the same type investigated by van Zwol *et al.* (type 9020), which is most likely is due to a batch-dependence of the bead quality.

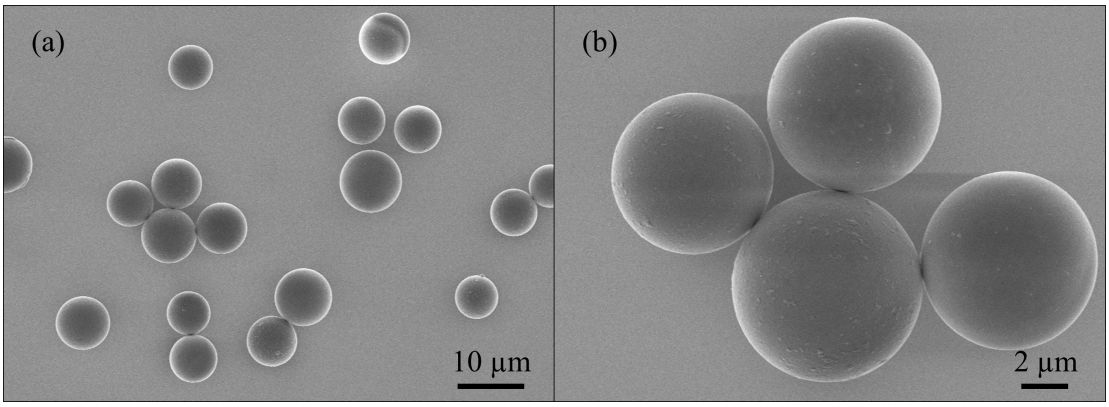

Figure 2.11: Scanning electron microscope images of the glass beads used in this work. The beads were supplied in form of a dry powder. A small amount of the bead-powder was poured onto a Si wafer that was coated with 20 nm of Pt. The overall sample was coated with an additional thin layer (3 nm) of Pt by means of sputtering. Picture (b) is a zoom-in of (a). ©2016 American Physical Society [Pil+16]

The choice of DUKE borosilicate glass 9008 beads meets all requirements mentioned above. If not mentioned otherwise, these beads were used in all experiments reported in this thesis.

2.3.2 Capillary

Rectangular capillaies (VitroCom, VitroTubes 5010-050, borosilicate rectangular glass capillary) were used for encapsulation of the dispersion of aqueous NaCl solution and beads. Force measurements were performed with a bead pushed against the upper inner wall of the capillary. Thus, the inner wall of the capillaries needed to be characterized.

SPM images at three different positions on a shiver of a VitroTubes 5010-050 borosilicate rectangular glass capillary revealed a mean RMS-roughness of the inner capillary wall of

$$\sigma = 0.3\,\text{nm}\ . \tag{2.12}$$

Fig. 2.12 shows an exemplary SPM image of the upper inner wall of the capillary. The roughness of the capillary was one order of magnitude smaller than the roughness of the beads. Furthermore, the surface of the capillary displayed occasional spikes (white

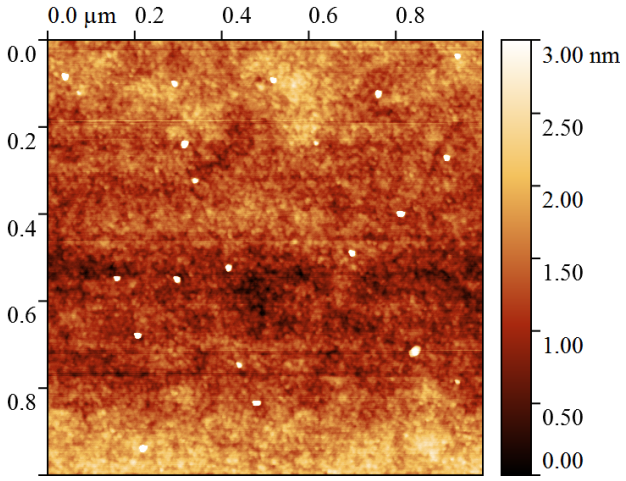

Figure 2.12: Scanning probe microscopy image of the inside of a VitroTubes 5010-050 borosilicate rectangular glass capillary. The height sensor topography was recorded in intermediate contact mode with a Dimension Icon FS device using an Olympus non-contact mode cantilever (OMCL-AC 240TS-W2, resonant frequency $f_0 = 70\,\mathrm{kHz}$). 1st order flattening was applied to the image-data. The RMS-roughness for this measurement after flattening was $\sigma = 0.3\,\mathrm{nm}$.

dots in fig. 2.12). However, he height of the spikes was smaller than 4 nm, which is comparable to the RMS-roughness of the beads. It was thus not expected that the spikes had a significant effect on the the electrostatic double-layer force between bead and wall. A more detailed discussion on the effect of roughness on the measured electrostatic double-layer force will be given in part 6.0.2.

2.4 Experimental Procedure and Data Acquisition

2.4.1 Preperations

Two aqueous NaCl solutions with salt concentrations of $c_0 = (0.10 \pm 0.01)\,\mathrm{mmol\,dm^{-3}}$ and $(1.0 \pm 0.1)\,\mathrm{mmol\,dm^{-3}}$ were prepared using ultra-pure water (Sartorius Arium 611 VF purification system, resistivity of $18.2\,\mathrm{M\Omega\,cm}$). A small amount of the dry glass beads was dispersed in ultra-pure water and sonicated for at least 15 min. 1 ml of NaCl solution was mixed with 50 µl of the bead dispersion, thus diluting the sample solutions to salt concentrations of approximately

$$c_0 = (95 \pm 10)\,\mu\mathrm{mol\,dm^{-3}} \quad \text{and} \quad (0.95 \pm 0.10)\,\mathrm{mmol\,dm^{-3}}\,. \tag{2.13}$$

The pH value of the sample was approximately $p\mathrm{H} = 4 - 4.5$ (measured with MERCK pH-indicator strips Acilit®).

The sample solutions were encapsulated in a glass capillary. I have experienced that

sealing the capillary worked best, when the outer surface of the capillary remained dry before contact with the sealing paste (Bayer, high-viscosity Baysilone paste). Thus, the following loading procedure was employed: The rectangular glass capillaries were supplied having a length of 50 mm. One capillary was prepared for breaking off a small capillary piece by scratching it with a diamond cutter approximately 8 mm away from one end. The other end of the capillary was then dipped into the sample solution and the sample solution filled the capillary by capillary rise. The scratched end was dipped into the sealing paste. The capillary was then broken. The other end of the 8 mm long capillary piece was dipped into the sealing paste. It was important to not dip the ends of the capillary too deep into the sealing paste so that the central part of the capillary stayed clean.

The sealed capillary piece was then placed in the middle of the high-pressure cell. Due to the sealing paste, the capillary piece stuck to the cell-body. The high-pressure cell was then pre-filled with water, closed and tilted by 90° for a couple of minutes in order to let the beads sediment to one side of the capillary. The cell was then connected to the high-pressure periphery and clamped on a platform that was connected to a motorized stage (Vision Lasertechnik) and placed between the objective and the condenser.

The glass beads were at one side of the capillary. A single bead was selected for all experiments at a given salt concentration and moved away from the wall to the center of the capillary by trapping it with the down beam and moving the high-pressure cell laterally. Far from the other beads, the selected bead was pushed upwards by the up beam. The cell was lowered continuously in order to keep the bead in the focus of the objective until the bead reached the upper inner wall of the capillary.

2.4.2 Recording a Force Curve

At the upper inner capillary wall the force curves were recorded. The interference laser was turned on and aligned so that the reflection interference pattern was centered on the bead and symmetrical. The intensity of the reflection interference signal I_{RI} measured by the avalanche photo-diode was recorded at a sampling rate of 50 kHz using a data acquisition card (National Instruments™ PCIe-6321, X Series Multifunction DAQ). Using this sampling rate, the Nyquist criterion was fulfilled, since the fastest recorded

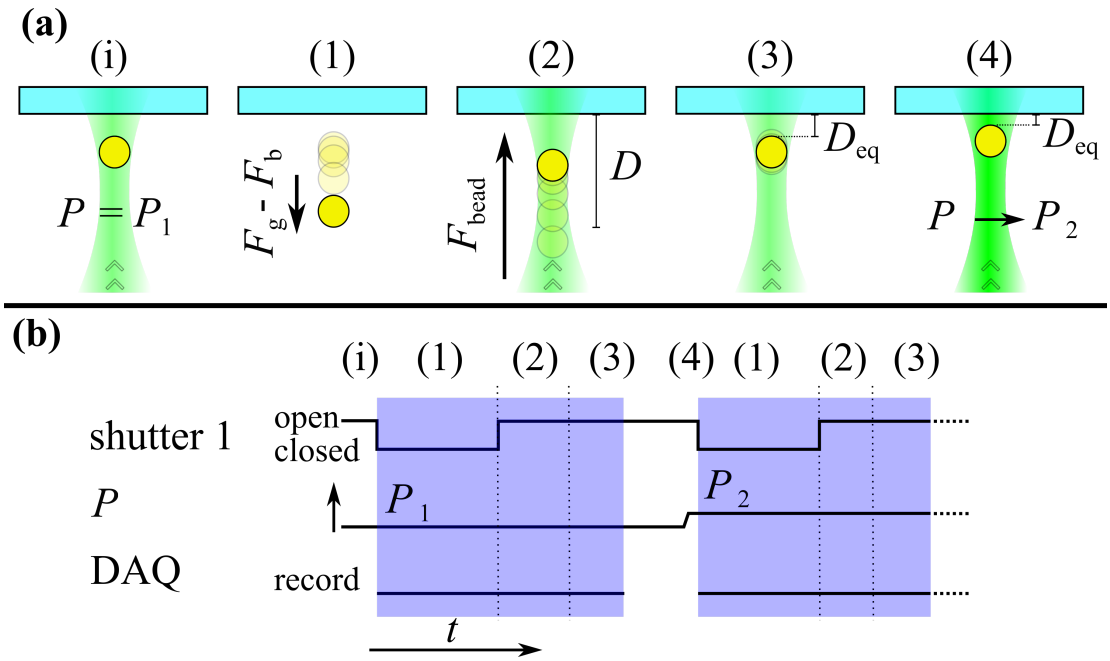

Figure 2.13: Scheme of the automated measurement. The different stages of the experiment (a) and the corresponding settings of the computer controlled shutter, attenuator (P) and data acquisition electronics (DAQ) (b).

frequency was of the order of 5 kHz. The data acquisition, shutter 1, i.e. the shutter that blocks the trapping beam and the variable attenuator were controlled using LabVIEW (National Instruments™) (fig. 2.13 (b)).

A force curve was automatically recorded in the following way: Initially, the power of the trapping beam was set to a value P_1 (fig. 2.13 (i)). Then shutter 1 was closed, blocking the trapping beam, and the data acquisition of I_{RI} was initiated (fig. 2.13 (1)). Since the density of the bead was larger than the density of water, the bead then sedimented a few micrometers away from the wall. Subsequently, shutter 1 was opened and the bead was pushed against the wall by the trapping beam (fig. 2.13 (2)). The force pushing the bead against the wall is given by

$$F_{\text{bead}} = -F_{\text{rp}} + F_{\text{g}} - F_{\text{b}} \, . \tag{2.14}$$

The bead moved against the wall until F_{bead} was counteracted by the double-layer force

F_{DL}. Around the equilibrium distance D_{eq} where

$$F_{\mathrm{bead}} = -F_{\mathrm{DL}}\left(D_{\mathrm{eq}}\right), \tag{2.15}$$

the bead performed thermal motion (fig. 2.13 (3)). The data acquisition was stopped and the power of the trapping beam P was increased to $P = P_2$ (fig. 2.13 (4)), thus increasing F_{bead} and reducing the equilibrium distance D_{eq}. Steps (1) to (4) were then repeated several times.

A measurement at a given power of the trapping beam $P = P_i$ is referred to as a *single measurement* (fig. 2.13 (b), highlighted blue). Every single measurement gave a single force-distance data point $\left(D_{\mathrm{eq}}, F_{\mathrm{DL}}\right)$. A series of data points derived from single measurements at different P_i composed a force curve.

2.4.3 Single Measurement

A single measurement gives the recorded intensity of the reflection interference signal I_{RI} versus time (fig. 2.14, black line). I_{RI} is related to the bead-wall distance D by [LS09]

$$2I_{\mathrm{RI}} = I_{\mathrm{max}} + I_{\mathrm{min}} - (I_{\mathrm{max}} - I_{\mathrm{min}}) \cos\left(\frac{4\pi n_{\mathrm{medium}}}{\lambda} D + \phi\right). \tag{2.16}$$

Here, I_{max} and I_{min} are the intensities of a maximum and a minimum of I_{RI}, n_{medium} is the refractive index of the medium between bead and wall, λ is the wavelength of the interference laser and ϕ is the phase of the cosine function at contact of bead and wall. The refractive index of water at a hydrostatic pressure of up to 1 kbar was determined by Schiebener *et al.* [Sch+90].

When the bead moved towards the wall, the recorded I_{RI} signal exhibited multiple extrema (fig. 2.14 (2)). For consecutive extrema in the measured interference signal the corresponding difference in distance D is

$$\Delta D = \frac{\lambda}{4 n_{\mathrm{medium}}}\,. \tag{2.17}$$

For water at $p = 1\,\mathrm{bar}$ up to 1 kbar and the wavelength of the here used interference laser ($\lambda = 635\,\mathrm{nm}$) the distance difference was $\Delta D \approx 119\,\mathrm{nm}$. By determining the

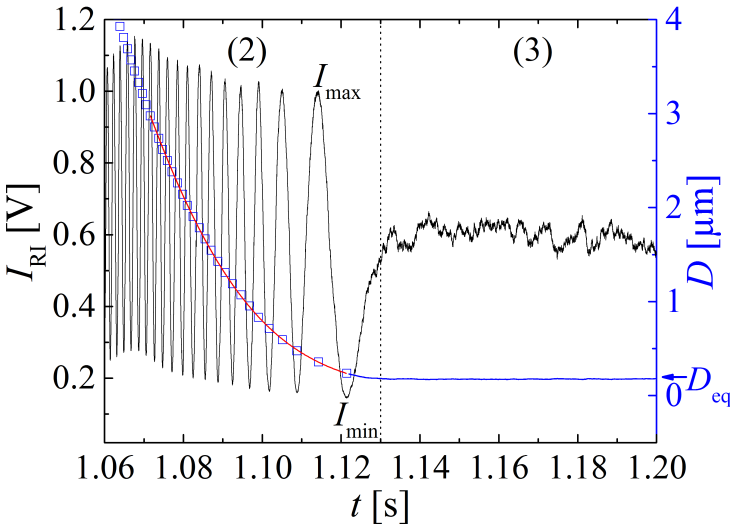

Figure 2.14: Example of a single measurement at $P = 83\,\mathrm{mW}$. Black line: Intensity of the reflection interference signal I_{RI}. Blue line: Derived bead-wall distance D. The parts before and after approximately 1.13 s correspond to steps (2) and (3) in fig. 2.13, respectively. ©2016 American Physical Society [Pil+16]

temporal position of the extrema, the trajectory of the bead moving against the wall was determined (fig. 2.14, blue squares). After the last minimum at around 1.12 s, equation (2.16) was strictly monotonic and could thus be inverted

$$D = \arccos\left(\pm\frac{2I_{RI} - (I_{max} + I_{min})}{I_{max} - I_{min}}\right) \cdot \frac{\lambda}{4n_{medium}\pi} - D_0\,, \tag{2.18}$$

yielding the blue line in fig. 2.14. Here, the sign inside the inverse cosine function depends on the side of the cosine where the recorded I_{RI} was located. The distance D_0 corresponds to the phase ϕ. Since by interferometry with a single laser only relative distances can be measured, the constant D_0 was at first not determined.

The I_{RI}-signal exhibited an envelope that is not accounted for by equation (2.16). This envelope was due to the lensing effect of the bead. It caused a distance dependence of the I_{max} and I_{min} values, i.e. the peak values of the different extrema differed from one another. This lead to an inaccuracy of the distances D determined by equation (2.18). Using extrapolation, the inaccuracy in D due to the lensing effect of the bead was determined to be of the order of 1 nm. The error was determined for all measured distances D_{eq} and taken into account for fitting.

It will be shown that the evaluation of step (2) (fig. 2.14) yields the force acting on the bead and also the constant D_0 needed for determination of the absolute distance D (see chapter 3). Furthermore, the evaluation of the thermal motion in equilibrium (step (3))

yields the precise value of the D_{eq} (see chapter 5).

3 Analysis of the Trajectory of the Bead Moving Towards the Wall

Force curves were recorded by performing single measurements at stepwise increasing powers of the trapping beam P (see part 2.4.3). At each single measurement, the bead was pushed against the wall by the sum of the radiation pressure force, gravity and buoyancy

$$F_{\text{bead}} = -F_{\text{rp}} + F_{\text{g}} - F_{\text{b}} \ . \tag{3.1}$$

The value of F_{bead} needed to be determined for every given P. For distances much larger than the Debye-length, i.e. $D > 7\lambda_{\text{D}}$, the electrostatic double-layer force between bead and wall is negligible. The force counteracting F_{bead} is the hydrodynamic drag F_{hd} (fig. 3.1), with

$$F_{\text{bead}} = -F_{\text{hd}} \ . \tag{3.2}$$

Gravity and buoyancy are independent of D. The radiation pressure force F_{rp} depends on the radius w of the beam at the position of the bead [Ash70]. The beam-radius is

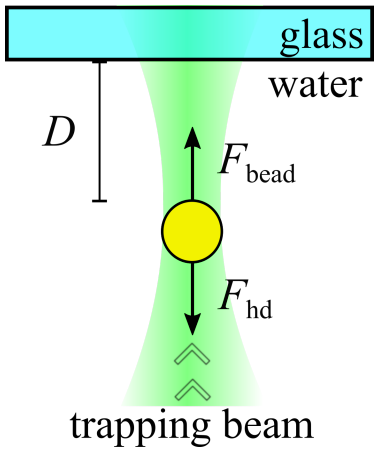

Figure 3.1: Bead pushed against the wall by the trapping beam. The force pushing the bead against the wall is counteracted by the hydrodynamic drag.

distance dependent [JZ08]

$$w(z) = w_0 \sqrt{1 + \left(\frac{z}{z_R}\right)^2} \,. \tag{3.3}$$

Here $z = 0$ is the position of the beam-waist along the direction of beam propagation (z-direction). For a beam waist radius of $w_0 = 2.4\,\mu\text{m}$ (see equation (2.3)) and a corresponding Rayleigh length of $z_R = 35.2\,\mu\text{m}$ the radius of the beam increases by less than 0.4 % for $z = 3\,\mu\text{m}$, which is negligible and thus should not affect F_{rp}. Thus, when evaluating the beads trajectory at bead-wall distances $D \leq 3\,\mu\text{m}$, F_{bead} may be assumed constant.

The constancy of F_{bead} has the important consequence that the electrostatic double-layer force for a bead-wall distance D_{eq} is equal to the hydrodynamic drag experienced by the bead for $D > 7\lambda_D$

$$F_{DL}\left(D_{eq}\right) = F_{hd} \,. \tag{3.4}$$

In this chapter, in order to determine F_{hd}, the trajectory of the bead moving towards the wall is evaluated. The equation of motion of a bead moving towards a wall through a liquid depends on the distance D. Analytic solutions of the equation of motion are determined and compared to the exact numerical solution. The distance dependence of the equation of motion is exploited in order to determine the absolute separation between bead and wall.

3.1 Equation of Motion

The equation of motion for a "slow" bead in a viscous fluid is given by the Stokes equation

$$F_{hd} = -6\pi R v \eta \,. \tag{3.5}$$

Here η is dynamic viscosity of the fluid and v is the velocity of the bead.

The quantity that determines whether this equation is applicable to the given system is the Reynolds number [HB83]

$$Re = \frac{2\rho v R}{\eta} \,. \tag{3.6}$$

Here ρ is the density and of the fluid. Using the radius of the here used beads $R \approx 4\,\mu\mathrm{m}$ yields for water $Re = 8v\ \mathrm{s\,m^{-1}}$. Since in this work $v < 1\,\mathrm{mm\,s^{-1}}$ for all experiments, $Re < 10^{-2}$, which is sufficiently small [HB83], confirming the applicability of equation (3.5).

However, for a bead moving against a wall, the effect of drainage of liquid from the gap between bead and wall must be accounted for. In this case, the equation of motion is given by the modified Stokes equation

$$F_{\mathrm{hd}} = -6\pi R v \eta \lambda_{\mathrm{B}}(D)\ . \tag{3.7}$$

For a given bead radius R, the factor $\lambda_{\mathrm{B}}(D)$ is the dimensionless wall-correction of the Stokes equation [Bre61]. It is a strictly monotonic function of D with

$$\lim_{D\to\infty} \lambda_{\mathrm{B}}(D) = 1 \tag{3.8}$$

and [CH85]

$$\lim_{D\to 0} \lambda_{\mathrm{B}}(D) = \frac{R}{D}\ . \tag{3.9}$$

Equation (3.8) depicts the case of a bead moving through a fluid in the absence of a wall where equation (3.7) reproduces the ordinary Stokes equation. An exact solution of $\lambda_{\mathrm{B}}(D)$ was derived by Brenner [Bre61]

$$\lambda_{\mathrm{B}}(D) = \frac{4}{3}\sinh(\alpha)\cdot\sum_{n=1}^{\infty}\frac{n(n+1)}{(2n-1)(2n+3)}\left[\frac{2\sinh(2n+1)\alpha + (2n+1)\sinh(2\alpha)}{4\sinh^2\left(n+\frac{1}{2}\right)\alpha - (2n+1)^2\sinh^2(\alpha)} - 1\right] \tag{3.10}$$

with

$$\alpha = \arccos\left(\frac{D}{R} + 1\right). \tag{3.11}$$

It is now evident, that $\lambda_{\mathrm{B}}(D) \equiv \lambda_{\mathrm{B}}(D/R)$, i.e. the wall correction depends on the ratio of bead-wall distance to bead radius. Numerical evaluation of the first 200 terms of equation (3.10) yielded a plot of λ_{B} (fig. 3.2 (a), black line).

The exact solution of equation (3.10) is only numerically possible. Thus, using the exact

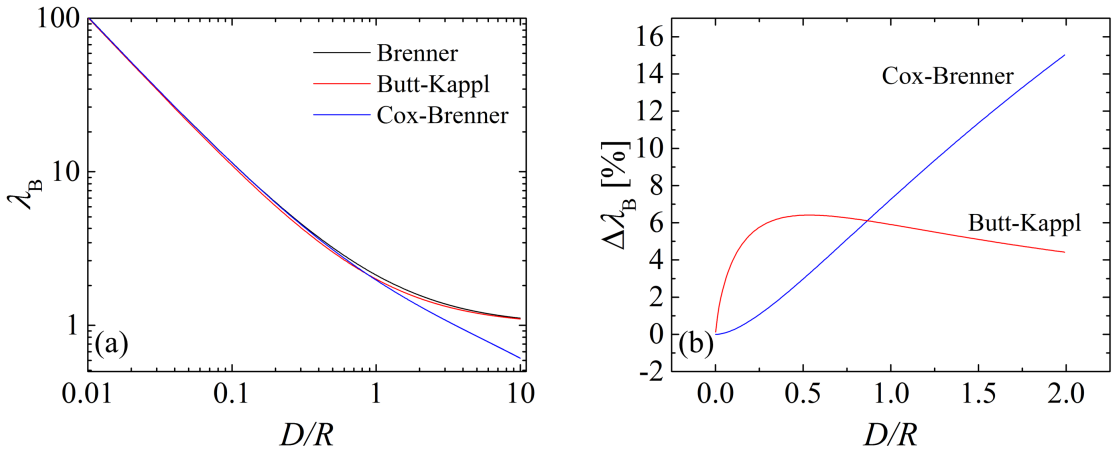

Figure 3.2: (a) Log-log plot of correction factor λ_B calculated independent of R with the exact equation (3.10) (black line), the Butt-Kappl approximation (3.12) (red line) and the Cox-Brenner approximation (3.14) (blue line). (b) Relative difference between exact calculation of λ_B and approximation by Butt-Kappl (red line) and Cox-Brenner (blue line) calculated with (3.13). Calculations were performed with MathWorks® Matlab® Version 7.14.0.739.

solution given by equation (3.10) for solving of equation (3.7) and evaluating the measured trajectories would be cumbersome and lengthy, especially since approximately 500 trajectories were evaluated in this thesis. An analytical approximation of (3.10) was motivated by Butt and Kappl [BK10]

$$\lambda_B^{BK}(D) = 1 + \frac{R}{D} \,. \tag{3.12}$$

They used the pragmatic approach of adding the asymptotic solutions (3.8) and (3.9), making $\lambda_B^{BK}(D)$ exact in the case of $D << R$ and $D >> R$ (fig. 3.2 (a), red line). Here, the case of $D \approx R$ was evaluated by calculation of

$$\Delta\lambda_B(D) = \frac{\lambda_B(D) - \lambda_B^{approx}(D)}{\lambda_B(D)} \,. \tag{3.13}$$

The error made by using $\lambda_B^{BK}(D)$ was found smaller than 6.5 % for all D (fig. 3.2 (b), red line).

Another approximation, valid for small values of D was given by Cox and Brenner

[CB67]

$$\lambda_B^{CB}(D) = \frac{R}{D} + \frac{1}{5}\ln\left(\frac{R}{D}\right) + 0.971264\ . \tag{3.14}$$

This approximation satisfies (3.9) but deviates from the exact solution for large D (fig. 3.2 (a), blue line). For a range of $10^{-3} < D/R < 3/4$, $\lambda_B^{CB}(D)$ was found to be closer to the exact $\lambda_B(D)$ than $\lambda_B^{BK}(D)$ (fig. 3.2 (b), blue line).

For evaluation of the measured beads trajectory, a model function $D(t)$ is needed. The wanted function is the solution of equation (3.7), or more explicitly

$$-1 = R \cdot a \frac{\mathrm{d}D}{\mathrm{d}t} \lambda_B(D)\ , \tag{3.15}$$

with

$$a := \frac{6\pi\eta}{F_{hd}}\ . \tag{3.16}$$

For $F_{hd} = const$ this differential equation can be solved by

$$-(t - t_i)\frac{1}{aR} = \int_{D_i}^{D} \lambda_B(z)\,\mathrm{d}z\ . \tag{3.17}$$

For the exact λ_B given by equation (3.10), equation (3.17) was solved by numerical integration using the adaptive Simpsons's method (fig. 3.3, black line).

For the Butt-Kappl (λ_B^{BK}) and Cox-Brenner (λ_B^{CB}) approximations solving equation (3.17) results in the implicit solutions for the trajectory of the bead

$$-(t - t_i)\frac{1}{aR} = \Lambda_B(D) - \Lambda_B(D_i)\ , \tag{3.18}$$

with

$$\Lambda_B^{BK}(D) := D + R\ln(D) \tag{3.19}$$

for the Butt-Kappl approximation and

$$\Lambda_B^{CB}(D) := \ln(D)\left(R - \frac{1}{5}D\right) + D\left(\frac{1}{5}R + 1.1712\right) \tag{3.20}$$

for the Cox-Brenner approximation.

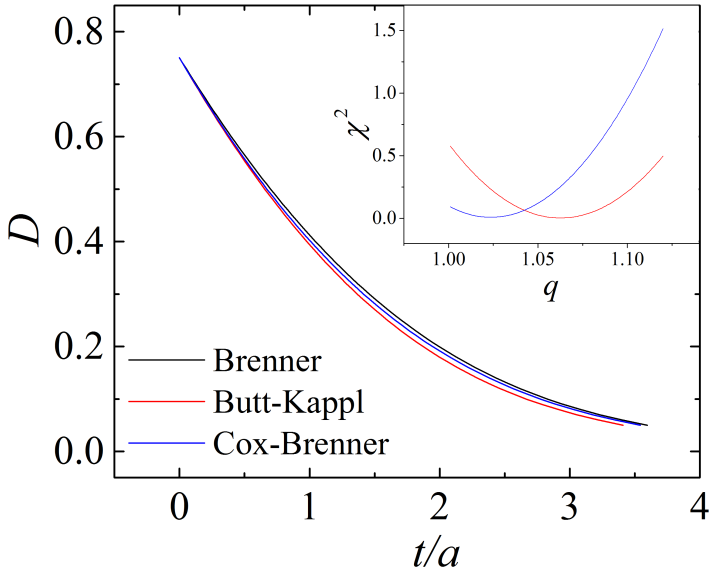

Figure 3.3: Calculated trajectory of a bead moving towards a wall for $F_{\mathrm{hd}} = const$ and $R = 1$ using the exact correction factor λ_{B} (black line) and the approximations by Butt-Kappl (red line) and Cox-Brenner (blue line). Inset shows sum of squared errors between the trajectories calculated with the exact and approximated correction factors. Calculations were performed with MathWorks® Matlab® Version 7.14.0.739.

The trajectories given by (3.18) were calculated on a range of $D_i = 3/4 \geq D \geq D_f = 1/20$ setting $R = 1$ and $t_i = 0$ (fig. 3.3, red line and blue line). The chosen range corresponds to $3\,\mu\mathrm{m} \geq D \geq 0.2\,\mu\mathrm{m}$ for a bead with $R = 4\,\mu\mathrm{m}$, which is the range of the measured trajectories that was evaluated. The exact and approximate calculated trajectories all display the same behavior. For a fixed range, the trajectories may be brought to overlap by scaling the antiderivatives $\Lambda_{\mathrm{B}}^{\mathrm{BK}}(D)$ and $\Lambda_{\mathrm{B}}^{\mathrm{CB}}(D)$ with a factor q. To find the value of q that provides the best overlap of exact and approximate solution, the sum of squared errors was calculated

$$\chi^2 = \sum_{n=0}^{N} \left[\int_{D_i}^{D_n} \lambda_{\mathrm{B}}(z)\,\mathrm{d}z - q\left(\Lambda_{\mathrm{B}}(D_n) - \Lambda_{\mathrm{B}}(D_i)\right) \right]^2, \tag{3.21}$$

where the range from D_i to D_f was divided into an equidistant grid $D_n = D_i - n/100$ with $N = \left(D_i - D_f\right) \cdot 100$. χ^2 had a minimum at $q_{\mathrm{min}}^{\mathrm{BK}} = 1.06$ and $q_{\mathrm{min}}^{\mathrm{CB}} = 1.02$ for the Butt-Kappl and the Cox-Brenner approximation, respectively (fig. 3.3 , inset).

The values of $q_{\min}$ are a measure of the error made by data evaluation with the analytic approximations of λ_B. When equation (3.18) is used for curve fitting, F_{hd} is a fit value. Instead of the hydrodynamic drag F_{hd}, a reduced drag force $\tilde{F}_{hd} = F_{hd}/q$ is determined by curve fitting. This means that using the Butt-Kappl approximation and the Cox-Brenner approximation the hydrodynamic drag is underestimated by approximately 6 % and 2 %, respectively. However, since this is only a minor error of the accuracy of determining F_{hd}, equation (3.18) together with (3.19) or (3.20) may be used as the function of the bead trajectory for data evaluation.

3.2 Data Evaluation

Evaluation of the reflection interference signal resulted in the trajectory of the bead (see part 2.4.3). The evaluation of the recorded reflection interference signal itself does not give the absolute bead-wall distance D, but a relative distance

$$\tilde{D} = D + D_0 \,, \tag{3.22}$$

with an offset D_0, which was not jet determined. For data evaluation, $\tilde{D} = 0$ was chosen to be the position of the bead corresponding to the last extremum of the reflection interference signal before the bead reaches D_{eq} (see fig. 2.14 of an exemplary single measurement at approximately $t = 1.12\,\mathrm{s}$). Using equation (3.18) yields the implicit function for the bead trajectory

$$t = -aR\Lambda_B\left(\tilde{D} - D_0\right) + \tilde{t} \,. \tag{3.23}$$

Here a, D_0 and $\tilde{t}$ are the fit-values, with the integration constant $\tilde{t} = t_i/(aR) + \Lambda_B(D_i)$, and $\Lambda_B(D)$ given by equations (3.19) or (3.20). F_{hd} was determined from the fit value a using tabulated values for the viscosity of water for a given temperature and pressure from the National Institute of Standards and Technology Chemistry Webbook [LMF].

The measured trajectories could be fitted with equation (3.23) with a coefficient of determination > 0.999 with both the Butt-Kappl and the Cox-Brenner approximation. The fit-curves of both approximations overlapped and were not distinguishable, thus only

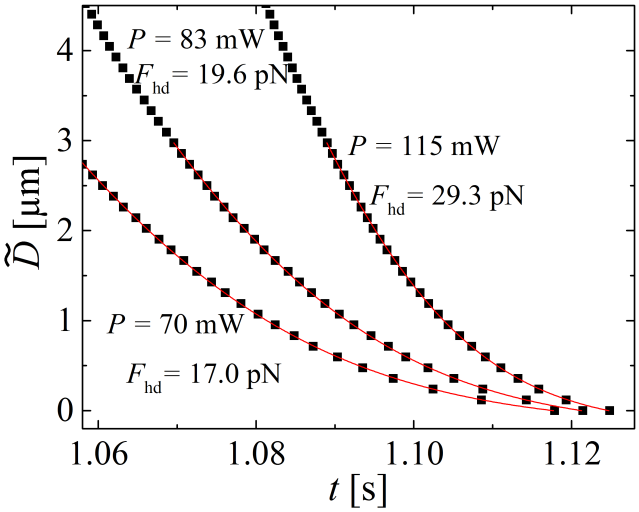

Figure 3.4: Trajectories of the bead moving against the wall for different powers of the trapping beam P (black squares). Approximately the last 3 µm before the wall were fitted using equation (3.23) (red lines). If not stated otherwise, in this work curve fitting was performed with OriginLab® OriginPro 9.1 OG (32-bit) using orthogonal regression. Here $R = (4.0 \pm 0.5)\,\mu\text{m}$, $c_0 = 0.1\,\text{mmol}\,\text{dm}^{-3}$, $p = 1\,\text{bar}$ and $T = (21 \pm 1)\,°\text{C}$.

the fit-curve of the Butt-Kappl approximation was plotted (fig. 3.4, red lines). From the steepness of the trajectories it is evident that for larger powers of the trapping beam P the bead moved faster against the wall and the determined F_{hd} was larger. The dependence of F_{hd} and thus F_{bead} on P is discussed in chapter 4.

In order to determine whether both approximations lead to equivalent results, a series of trajectories recorded for different powers of the trapping beam P was evaluated with equation (3.23) using equations (3.19) and (3.20) (fig. 3.5). The force determined using the Butt-Kappl approximation $F_{\text{hd}}^{\text{BK}}$ is correlated to the force determined using the Cox-Brenner approximation $F_{\text{hd}}^{\text{CB}}$ with a Pearson product-moment correlation coefficient of $r_{\text{Pearson}} = 1$. This means that there is no qualitative difference between the two approximations. Fitting with a proportional function (fig. 3.5, red line) revealed

$$\frac{F_{\text{hd}}^{\text{CB}}}{F_{\text{hd}}^{\text{BK}}} = 1.04\,. \tag{3.24}$$

This is in good agreement with the above determined correction factors

$$\frac{q_{\text{min}}^{\text{BK}}}{q_{\text{min}}^{\text{BK}}} = \frac{1.06}{1.02} = 1.04\,. \tag{3.25}$$

The values of the distance offset D_0 were as well strongly correlated with $r_{\text{Pearson}} > 0.999$. On average the Butt-Kappl and Cox-Brenner approximations yielded $\overline{D_0}^{\text{BK}} =$

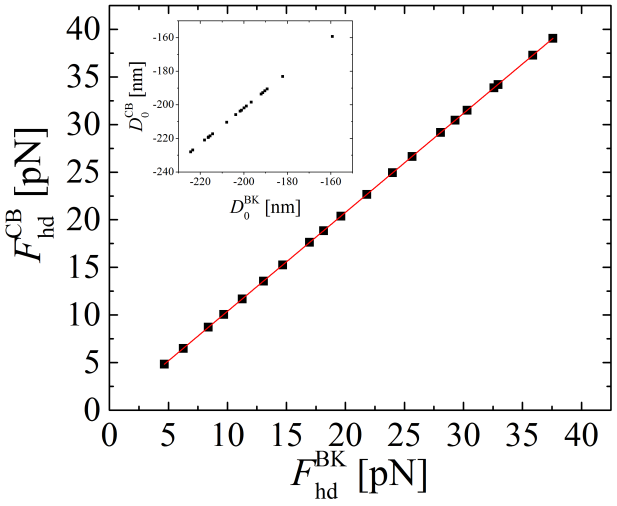

Figure 3.5: Comparison of fit values F_{hd} and D_0 (inset) determined with the Butt-Kappl and the Cox-Brenner approximation. 20 trajectories with $R = (4.0 \pm 0.5)\,\mu m$, $c_0 = 0.1\,mmol\,dm^{-3}$, $p = 1\,bar$, $T = (21 \pm 1)\,°C$ and P increasing from 28 mW to 142 mW in equidistant steps of 5.7 mW were evaluated.

$(-202.1 \pm 15.9)\,nm$ and $\overline{D_0}^{CB} = (-204.3 \pm 16.8)\,nm$, i.e. a difference of approximatel 1 %. It is thus evident that both functions lead to equivalent results. Due to its simplicity the Butt-Kappl approximation, namely

$$t = -aR\left(\tilde{D} - D_0 + R\ln\left(\tilde{D} - D_0\right)\right) + \tilde{t} \tag{3.26}$$

was used in this work for evaluation of the trajectory of the bead moving towards the wall.

3.2.1 Errors of the Fit

Before fitting the measured trajectories, two parameters must be chosen, i.e.

1. the radius R of the bead and
2. the end of the fit-range D_f.

The uncertainty of the radius ΔR has a direct influence on equation (3.26). The choise of D_f influences the fit due to the D-dependence of the error of the approximation $\Delta\lambda_B$ (fig. 3.2 (b)). Thus, both parameters influence the determined F_{hd} and D_0. In order to determine the influence of ΔR on F_{hd} and D_0, the same data-set as in fig. 3.5 was evaluated by fitting it with a radius subsequently set to $R + \Delta R$ and $R - \Delta R$ and determining the largest absolute deviation of the fit values from those obtained by fitting with R. Setting $R = 4.0\,\mu m$ and $\Delta R = 0.5\,\mu m$ yielded

- $\Delta F_{\mathrm{hd}}/F_{\mathrm{hd}} \approx 22\,\%$ ($\Delta F_{\mathrm{hd}}/F_{\mathrm{hd}} \approx 25\,\%$ with $R = 3.6\,\mu\mathrm{m}$) and
- $\Delta D_0 \approx 13.7\,\mathrm{nm}$

systematically at all powers P. It is important to note that ΔR only influences the accuracy of determining F_{hd}. Thus, although the corresponding error ΔF_{hd} is significantly large, it is insignificant when comparing force curves recorded with the same bead. Hence, in this work, for experiments at a given salt concentration and different hydrostatic pressures, the same bead was used to record all force curves.

Only the last $3\,\mu\mathrm{m}$ of the bead's trajectory were fitted, i.e. $D_{\mathrm{f}} = 3\,\mu\mathrm{m}$. The error due to the choice of the fitting-range was evaluated by subsequently setting $D_{\mathrm{f}} = 2\,\mu\mathrm{m}$ and $D_{\mathrm{f}} = 4\,\mu\mathrm{m}$, and determining the largest absolute deviation of the fit values from those obtained by fitting with $D_{\mathrm{f}} = 3\,\mu\mathrm{m}$. The determined errors were on average

- $\overline{\Delta F_{\mathrm{hd}}/F_{\mathrm{hd}}} \approx 1\,\%$ and
- $\overline{\Delta D_0} \approx 4.3\,\mathrm{nm}$.

The error of F_{hd} was calculated for every force-distance data point and accounted for by the curve-fitting algorithm.

3.3 Determination of the Absolute Distance

The reflection interference signal by itself does not allow the determination of the absolute bead-wall distance D (see equation (2.16)). Determining D from analysis of the bead's trajectory is possible but error-prone (see part 3.2). However, it will be shown that using the information gained from the evaluation of the bead's trajectory, the phase at contact ϕ of the reflection interference signal may be determined to be exactly π, allowing an accurate determination of the absolute bead-wall distance.

The here used reflection interference technique is very similar to reflection interference contrast microscopy (RICM) [Nad+01; RS92; LS09]. For RICM, it was argued by Radler and Sackmann that the phase is determined $\phi = \pi$, because the liquid has a lower refractive index than the bead and the wall [RS92]. The refractive index of borosilicate glass is lower than that of water, hence Radler and Sackmann's argument holds for the presently discussed experimental configuration. The reason for the fixed value of

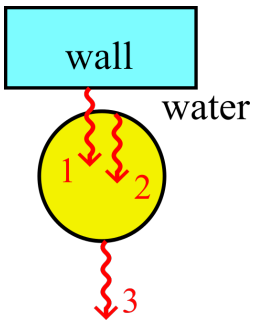

Figure 3.6: Rays reflected from the water-wall interface (1), and the bead-water interfaces facing the wall (2) and averted from the wall (3).

ϕ is that the reflection at the water-wall interface undergoes a phase shift by π (fig. 3.6, ray 1) while the the reflection at the bead-water interface doesn't (fig. 3.6, ray 2). However, this argumentation neglects the influence of further reflections, in particular a third reflection at the bead-water interface averted from the wall (fig. 3.6, ray 3). For the usual RICM configuration this third reflection most likely can be neglected, since in RICM setups an incoherent light-source is used for interference measurement [RS92; LS09]. However, in this work a laser-diode was used, where the coherence length is of the order of millimeters, i.e. much larger than the diameter of the bead. Thus, $\phi = \pi$ cannot be assumed *a priori*.

Assuming an influence of a third ray, the phase at contact would depend on the radius of the bead, i.e. $\phi(R)$. Evaluation of the trajectory of a bead moving against the wall using equation (3.26) for different beads with radii R from 2.6 µm to 5.2 µm allowed the investigation of the R dependence of ϕ (fig. 3.7), since a given phase ϕ corresponds to a distance offset D_0. Using equation (2.16), the determined D_0 were converted into values of ϕ in units of π.

The effect of a third reflection due to e.g. an additional membrane was studied in RICM experiments [LS09]. The change in ϕ was found to depend on the ratio of the membrane thickness and the wavelength of the reflected light. For a membrane of 4 nm thickness illuminated with light with a wavelength in the visible range, a change in ϕ of approximately 0.4π was stated [LS09]. Thus, for the range of here investigated radii, ϕ should assume seemingly random values from 0 to 2π. This however was not observed. The measured values all were in a range between 0.7π and 1.1π, demonstrating that ϕ is not a function of R. The variations of ϕ rather originate from inaccuracies related to the evaluation of the bead's trajectory. It can thus be concluded, that the third reflection

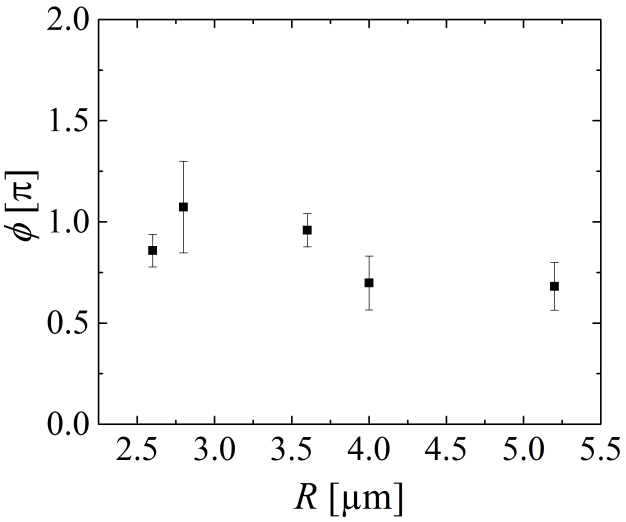

Figure 3.7: Phase of the reflection interference signal ϕ versus radius R of the bead. In case of $R = 2.6\,\mu m$ and $R = 2.8\,\mu m$ silica microspheres type SS06N from Bangs Laboratories, Inc. were used. The beads with $R = 3.6\,\mu m$ and $R = 4\,\mu m$ were described in part 2.3. In case of $R = 5.2\,\mu m$ a borosilicate glass microsphere type 9010 from DUKE Scientific Corp. was used.

does not influence ϕ, yielding analogously to the RICM case that

$$\phi = \pi \, . \tag{3.27}$$

Hence, for the experiment in part 3.2 we get

$$D_0 = -\frac{\lambda}{2n} \tag{3.28}$$

and with this the absolute distance calibration

$$D = \tilde{D} + \frac{\lambda}{2n} \approx \tilde{D} + 238\,\mathrm{nm} \, . \tag{3.29}$$

3.4 Summary

In this chapter the trajectory of the bead moving towards the wall was exploited in order to determine the hydrodynamic drag on the bead and the absolute bead-wall distance. It was discussed that the determination of the hydrodynamic drag allows the force calibration of the measured electrostatic double-layer force.

Approximations of the distance dependent wall-effect correction factor λ_B were discussed. It was found that a simple approximation proposed by Butt and Kappl allows accurate determination of λ_B for all distances D. Based on this approximation, an

equation was derived that allowed the determination of both absolute distance and hydrodynamic drag. The combination of the results from evaluation of the beads trajectory with properties of the reflection interference signal allowed for an accurate determination of the absolute bead-wall distance.

4 The Force Pushing the Bead Against the Wall

The force pushing the bead against the wall was assumed to be given by

$$F_{\text{bead}} = -F_{\text{rp}} + F_{\text{g}} - F_{\text{b}} \ . \tag{4.1}$$

with the difference of gravity and bouyancy

$$F_{\text{g}} - F_{\text{b}} = \frac{4}{3}\pi R^3 g \left(\rho_{\text{bead}} - \rho_{\text{water}}\right) \tag{4.2}$$

and the radiation pressure force F_{rp}. Here $g = 9.81\,\text{m}\,\text{s}^{-2}$ is the gravitational acceleration in central Germany. In this chapter the validity of equation (4.1) will be proven. The measured radiation pressure force will be compared to calculations based on the generalized Lorentz-Mie theory. Furthermore, possible force fluctuations due to the dependence of F_{rp} on the position of the bead lateral to the beam-axis will be estimated.

4.1 Dependence on Beam Power

The radiation pressure force is proportional to the number of photons that are refracted by the bead, and thus proportional to the power of the trapping beam P [Ash70; NB04; MP02]. We can thus define the force efficiency

$$f_{\text{rp}} := \frac{F_{\text{rp}}}{P} \ , \tag{4.3}$$

which is independent of the beam power P. In chapter 3 it was established that $F_{\text{bead}} = -F_{\text{hd}}$ (equation (3.2)). Thus, by evaluating the hydrodynamic drag for multiple P we expect to find a linear function

$$F_{\mathrm{hd}} = f_{\mathrm{rp}} \cdot P + F_{\mathrm{b}} - F_{\mathrm{g}} \,. \tag{4.4}$$

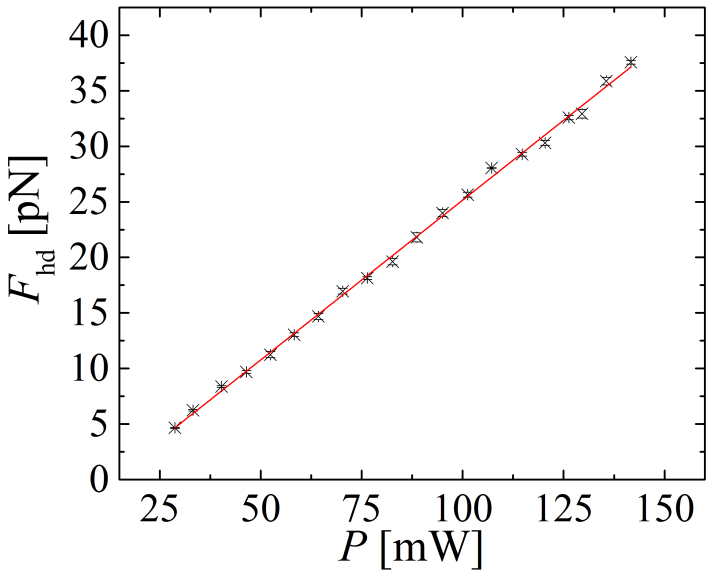

Figure 4.1: The hydrodynamic drag versus laser power for a bead with $R = (4.0 \pm 0.5)\,\mu\mathrm{m}$ (crosses) fitted with equation (4.4) (red line). Fit values were $f_{\mathrm{rp}} = (0.29 \pm 0.06)\,\mathrm{pN\,mW^{-1}}$ and $F_{\mathrm{b}} - F_{\mathrm{g}} = (-3.6 \pm 0.2)\,\mathrm{pN}$. Other experimental parameters: $c_0 = 0.1\,\mathrm{mmol\,dm^{-3}}$, $p = 1\,\mathrm{bar}$ and $T = (21 \pm 1)\,^{\circ}\mathrm{C}$.

The measured force could be fitted with equation (4.4) with a calculated coefficient of determination of 1. This proves that the power dependent part of the force pushing the bead against the wall is non-thermal. If e.g. the trapping beam heated up the bead, additional effects like convection would lead to a deviation of the measured curve from a line.

Calculating the difference of buoyancy and gravity with equation (4.2) yields

$$F_{\mathrm{b}} - F_{\mathrm{g}} = (-4.1 \pm 1.5)\,\mathrm{pN} \,. \tag{4.5}$$

Here $R = (4.0 \pm 0.5)\,\mu\mathrm{m}$, $\rho_{\mathrm{water}} \approx 1\,\mathrm{g\,cm^{-3}}$ and $\rho_{\mathrm{bead}} = 2.55\,\mathrm{g\,cm^{-3}}$ (value provided by manufacturer) was used. This result is in quantitative agreement with the intercept of the fitted function at $(-3.6 \pm 0.2)\,\mathrm{pN}$ in fig. 4.1. We can thus conclude that the force on the bead is well represented by equation (4.1).

The evaluation of the hydrodynamic drag yields the force efficiency for the here presented experimental configuration

$$f_{\mathrm{rp}} = (0.29 \pm 0.06)\,\mathrm{pN\,mW^{-1}}\ . \tag{4.6}$$

The force efficiency f_{rp} can alternatively be determined using the generalized Lorentz-Mie therorie (GLMT) [RGG94]. Using the program ABSphere [Ren14] for the given experimental configuration ($R = (4.0 \pm 0.5)\,\mu\mathrm{m}$, $w_0 = (2.4 \pm 0.4)\,\mu\mathrm{m}$, $\lambda/n_{\mathrm{water}} = 397\,\mathrm{nm}$ $n_{\mathrm{bead}}/n_{\mathrm{water}} = 1.164$) yields

$$f_{\mathrm{rp}}^{\mathrm{GLMT}} = (0.11 \pm 0.06)\,\mathrm{pN\,mW^{-1}}\ . \tag{4.7}$$

This theoretically determined force efficiency is lower than the measured f_{rp} (equation 4.6). The discrepancy could be explained with the imprecision of n_{bead}. The value stated by the manufacturer ($n_{\mathrm{bead}} = 1.56$ @ $589\,\mathrm{nm}$) is explicitly not intended for calibration and could thus vary. Also, due to dispersion n_{bead} would be slightly larger for a wavelength of 532 nm than for 589 nm. An increased value of n_{bead} by 5 % would resolve the discrepancy.

4.2 Effect of Non-Conservatism of the Radiation Pressure Force

Ashkin pointed out that the radiation pressure force excreted by a Gaussian beam on a bead is not conservative [Ash92]. Roichman *et al.* have found that due to this non-conservatism a bead trapped by optical tweezers does not assume a static equilibrium position but traces out a tordial vortex [Roi+08]. These additional fluctuations could influence the equilibrium position of the trapped bead. De Messieres *et al.* porposed a simple model of the optical force $\vec{F}_{\mathrm{op}}$ experienced by a trapped bead that reproduced the findings by Riochman *et al.* [MDLP11]

$$\vec{F}_{\mathrm{op}}\left(\vec{r}\right) = \vec{F}_{\mathrm{gr}}\left(\vec{r}\right) + F_{\mathrm{rp}}^{eff}(l)\hat{z}\ , \tag{4.8}$$

with harmonic restoring force due to the gradient in laser-intentsity

$$\vec{F}_{\mathrm{gr}}\left(\vec{r}\right) = -k_{\mathrm{x}} x\hat{x} - k_{\mathrm{y}} y\hat{y} - k_{\mathrm{z}} z\hat{z} \; . \tag{4.9}$$

Here $\vec{r} = x\hat{x} + y\hat{y} + z\hat{z}$ is the displacement of the bead relative to the focus of the beam, with $\left\|\vec{r}\right\|$ assumed small, and k_i is the trap-stiffness in i-th direction. z is the direction of the beam propagation. The radiation pressure force was modeled as

$$F_{\mathrm{rp}}^{eff}(l) = F_{\mathrm{rp}} + Sl^2 \; . \tag{4.10}$$

Here $l = \sqrt{x^2 + y^2}$ is the lateral displacement of the bead from the beam-axis. For a bead centered on the beam axis $F_{\mathrm{rp}}^{eff}(l = 0) = F_{\mathrm{rp}}$, as was used in this work. Within this model, the radiation pressure force is not conservative, since

$$\nabla \times \left(F_{\mathrm{rp}}^{eff}(l)\hat{z}\right) = 2S \begin{bmatrix} y \\ -x \\ 0 \end{bmatrix} \; , \tag{4.11}$$

which generically is not zero. Whereas $\nabla \times \vec{F}_{\mathrm{gr}}\left(\vec{r}\right) = \vec{0}$, proving the conservative character of the gradient force.

For beads that are larger than the radius of the beam ($R > w_0$), S is positive. The observations by Roichman *et al.* can now be understood in the following way [MDLP11]: In the absence of thermal motion the bead would be trapped at a position z_{eq} along the beam-axis, where $k_{\mathrm{z}} z_{\mathrm{eq}} = F_{\mathrm{rp}}$. However, thermal motion causes lateral displacement of the bead. When the bead moves off-axis, the radiation pressure force is increased, causing an additional displacement in z-direction. Eventually, the on-axis position of the bead will be restored, causing the radiation pressure to assume its initial strength. The bead's on-axis position will then return to z_{eq}, restoring initial conditions.

In this work the optical trap was of long-working-distance type, which differs from optical tweezers by lack of a restoring force in z-direction. For example in the case of a bead illuminated by the trapping beam in bulk water, $k_{\mathrm{z}} \approx 0$. However, when the bead was at a small distance D_{eq} from the glass wall, it was trapped in z-direction due to the electrostatic double-layer force. Thus, $k_{\mathrm{z}} = \frac{\mathrm{d}F_{\mathrm{DL}}}{\mathrm{d}z}\left(D_{\mathrm{eq}}\right)$. The profile of the optical forces for our experimental configuration was calculated using GLMT (fig. 4.2). For small

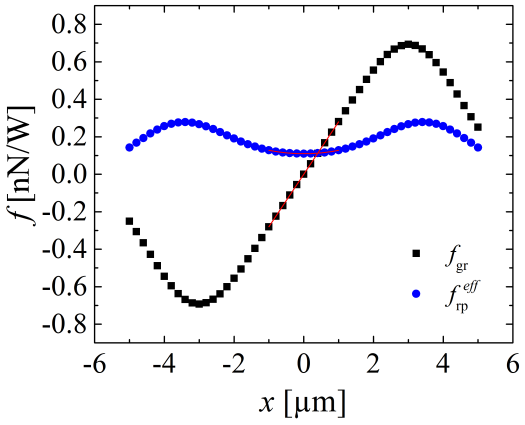

Figure 4.2: Radiation pressure force efficiency f_{rp}^{eff} and gradient force efficiency f_{gr} for lateral displacements from the beam axis with $y = 0$ and $-5\,\mu\mathrm{m} \leq x \leq 5\,\mu\mathrm{m}$ calculated with ABSphere [Ren14]. Red lines: Fits with equations (4.12) and (4.13) on the range $-1\,\mu\mathrm{m} < x < 1\,\mu\mathrm{m}$ yield $f_{\mathrm{rp}} = 0.11\,\mathrm{pN\,mW^{-1}}$, $S/P = 0.02\,\mathrm{pN\,mW^{-1}\,\mu m^{-2}}$ and $k_{\mathrm{x}}/P = 0.28\,\mathrm{pN\,mW^{-1}\,\mu m^{-1}}$. Errors of the fit-values were below 1 %. Parameter of the calculation: $R = 4.0\,\mu\mathrm{m}$, $w_0 = 2.4\,\mu\mathrm{m}$, $\lambda/n_{\mathrm{water}} = 397\,\mathrm{nm}$, $n_{\mathrm{bead}}/n_{\mathrm{water}} = 1.164$.

displacements $|x| \leq 1\,\mu\mathrm{m}$ the radiation pressure force efficiency f_{rp} could be fitted with

$$f_{\mathrm{rp}}^{eff}(l) = f_{\mathrm{rp}} + \frac{S}{P} l^2 \,, \tag{4.12}$$

which was deduced by dividing (4.10) by P. In the same range the gradient force was found harmonic with

$$f_{\mathrm{gr}} = \frac{F_{\mathrm{gr}}}{P} = \frac{k_{\mathrm{x}}}{P} x \,. \tag{4.13}$$

Thus, equation (4.8) is applicable to our experimental configuration and can be used for estimating the effect of the non-conservatism of the radiation pressure force.

Pilat *et al.* have argued that the additional displacement caused by the fluctuations can be estimated by determining the mean radiation pressure force [Pil+16]. The mean square displacement of the bead from the beam-axis is given by

$$\left\langle l^2 \right\rangle = 2 \frac{k_{\mathrm{B}} T}{k_{\mathrm{x}}} \,, \tag{4.14}$$

assuming $k_{\mathrm{x}} = k_{\mathrm{y}}$. For the mean effective radiation pressure force we thus get

$$\overline{F}_{\mathrm{rp}}^{eff} \approx F_{\mathrm{rp}} \left(1 + \frac{2 S k_{\mathrm{B}} T}{F_{\mathrm{rp}} k_{\mathrm{x}}} \right) . \tag{4.15}$$

For our experimental configuration $k_{\mathrm{x}} > 10^{-5}\,\mathrm{N\,m^{-1}}$ and $S/F_{\mathrm{rp}} \approx 0.2\,\mu\mathrm{m^{-2}}$ (fig. 4.2), yielding

$$\frac{2 S k_{\mathrm{B}} T}{F_{\mathrm{rp}} k_{\mathrm{x}}} < 1.6 \times 10^{-4} \,. \tag{4.16}$$

Thus, lateral fluctuations of the bead could cause an increase of the radiation pressure force on the femtonewton range. In order to estimate the effect on the equilibrium position D_{eq} we approximate $F_{\mathrm{bead}} \approx -\overline{F}_{\mathrm{rp}}^{eff}$, thus neglecting gravity an buoyancy. The corrected position $\tilde{D}_{\mathrm{eq}}$ can be calculated using $\overline{F}_{\mathrm{rp}}^{eff} = F_{\mathrm{DL}}\left(\tilde{D}_{\mathrm{eq}}\right)$ and $F_{\mathrm{rp}} = F_{\mathrm{DL}}\left(D_{\mathrm{eq}}\right)$. Using equation (1.4) for F_{DL} we get

$$\tilde{D}_{\mathrm{eq}} = D_{\mathrm{eq}} - \lambda_{\mathrm{D}} \ln\left(1 + \frac{2Sk_{\mathrm{B}}T}{F_{\mathrm{rp}}k_{\mathrm{x}}}\right). \tag{4.17}$$

For $\lambda_{\mathrm{D}} < 30\,\mathrm{nm}$ the corrective term in (4.17) is of the order of picometer, which is below the resolution of the technique.

4.3 Summary

It could be shown that the force pushing the bead against the wall was given by the sum of the radiation pressure force and the effective gravitational force. Thermal effects due to excessive absorption of the laser light were not observed. It was further estimated that the non-conservative character of the radiation pressure force has no influence on the experiments performed in this work.

5 Analysis of the Thermal Motion of the Bead Close to the Wall

For a given power of the trapping beam P, the glass bead was pushed against the glass wall by a force F_{bead} (see chapters 3 and 4). In the absence of thermal motion the bead would have moved against the wall until it reached a distance D_{eq} where

$$F_{\text{bead}} = -F_{\text{DL}}\left(D_{\text{eq}}\right). \tag{5.1}$$

The method of determining force curves used in this work relies on the determination of D_{eq}. However, due to thermal motion the distance D fluctuates randomly (fig. 5.1), resulting in a statistical distribution of the distances D.

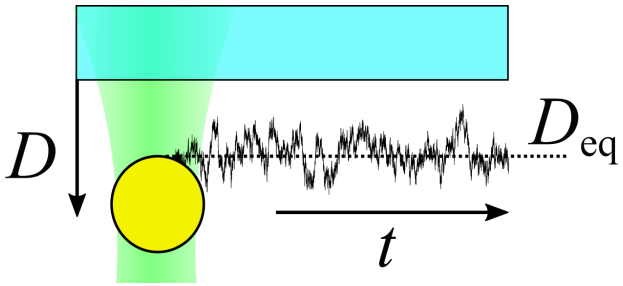

Figure 5.1: Thermal motion of the bead at the wall.

For a colloidal bead in a potential $V(D)$ the probability density of distances $p(D)$ is given by the Boltzmann distribution [AP87]

$$p(D) = A \exp\left(-\frac{V(D)}{k_{\text{B}}T}\right). \tag{5.2}$$

Here A is a factor ascertaining the normalization $\int_{-\infty}^{+\infty} p(D)\,\mathrm{d}D = 1$. It is noteworthy that,

although the hydrodynamic drag on the bead is distance dependent (equation (3.7)), the probability density $p(D)$ is not influenced by the hydrodynamic wall effect and only depends on the potential $V(D)$ [AP87]. For our experimental configuration the potential $V(D)$ is implicitly given by

$$-V'(D) \equiv -\frac{\mathrm{d}V}{\mathrm{d}D}(D) = F_{\text{total}} \,, \tag{5.3}$$

where F_{total} is the total force acting on the bead

$$F_{\text{total}}(D) = F_{\text{DL}}(D) + F_{\text{bead}} \,, \tag{5.4}$$

which in D_{eq} by definition (equation (5.1)) is zero

$$F_{\text{total}}\Big(D_{\text{eq}}\Big) = 0 \,. \tag{5.5}$$

In order to evaluate $p(D)$ and thus determine D_{eq} we will at first approximate equation (5.2).

5.1 Approximation of the Probability Distribution

We will first argue that D_{eq} is the position of a minimum of $V(D)$ and thus the most probable distance. From equations (5.3) and (5.5) we know that $V(D)$ is at an extremum at D_{eq}. For our experimental configuration F_{DL} is given by an exponentially decaying function

$$F_{\text{DL}}(D) = F_0 \exp\left(-\frac{D}{\lambda_{\text{D}}}\right), \tag{5.6}$$

where the decay-constant is the Debye-length λ_{D} and F_0 is the force-amplitude. A more detailed discussion of $F_{\text{DL}}(D)$ will be given in chapter 6. Using equation (5.6), the differentiation of equation (5.3) results in

$$V''(D) = -F'_{\text{total}}(D) = \frac{1}{\lambda_{\text{D}}} F_{\text{DL}}(D) \,, \tag{5.7}$$

yielding that $V(D)$ is a convex function, since $V''(D) > 0$ for all D. Thus D_{eq} is the position of the minimum of $V(D)$ and the maximum of $p(D)$. Assuming only small deviations

$$\Delta D = D - D_{\text{eq}} \tag{5.8}$$

of the bead's position from the equilibrium and most probable position D_{eq}, the potential can be expanded

$$V(D) = V\left(D_{\mathrm{eq}}\right) + \underbrace{V'\left(D_{\mathrm{eq}}\right)\Delta D}_{=:T_1} + \underbrace{\frac{1}{2}V''\left(D_{\mathrm{eq}}\right)\Delta D^2}_{=:T_2} + \underbrace{\frac{1}{6}V'''\left(D_{\mathrm{eq}}\right)\Delta D^3}_{=:T_3} + \mathcal{O}\left(\Delta D^4\right) . \tag{5.9}$$

By definition of D_{eq}, $V'\left(D_{\mathrm{eq}}\right) = 0$ and thus $T_1 = 0$. In order to estimate the influence of T_3 on $V(D)$ relative to T_2, equation (5.7) is differentiated

$$V'''(D) = -\frac{1}{\lambda_{\mathrm{D}}^2} F_{\mathrm{DL}}(D) . \tag{5.10}$$

We thus get

$$T_2 = \frac{1}{2}\frac{1}{\lambda_{\mathrm{D}}} F_{\mathrm{DL}}\left(D_{\mathrm{eq}}\right)\Delta D^2 = \frac{1}{2}\lambda_{\mathrm{D}} F_{\mathrm{DL}}\left(D_{\mathrm{eq}}\right)\left(\frac{\Delta D}{\lambda_{\mathrm{D}}}\right)^2 \tag{5.11}$$

and

$$T_3 = -\frac{1}{6}\frac{1}{\lambda_{\mathrm{D}}^2} F_{\mathrm{DL}}(D)\Delta D^3 = -\frac{1}{6}\lambda_{\mathrm{D}} F_{\mathrm{DL}}(D)\left(\frac{\Delta D}{\lambda_{\mathrm{D}}}\right)^3 . \tag{5.12}$$

Dividing (5.12) by (5.11) gives

$$\frac{T_3}{T_2} = -\frac{1}{3}\frac{\Delta D}{\lambda_{\mathrm{D}}} . \tag{5.13}$$

We can thus conclude that for

$$\Delta D << 3\lambda_{\mathrm{D}} , \tag{5.14}$$

T_3 and higher orders of ΔD in equation (5.9) can be neglected, yielding the harmonic approximation of the potential

$$V(D) \approx V\left(D_{\mathrm{eq}}\right) + \frac{1}{2}V''\left(D_{\mathrm{eq}}\right)\Delta D^2 . \tag{5.15}$$

The corresponding probability density is given by

$$p(D) = \tilde{A}\exp\left(-\frac{1}{2}\frac{V''\left(D_{\mathrm{eq}}\right)}{k_{\mathrm{B}}T}\left(D - D_{\mathrm{eq}}\right)^2\right) . \tag{5.16}$$

Here $\tilde{A} := A\exp\left(-\frac{V\left(D_{\mathrm{eq}}\right)}{k_{\mathrm{B}}T}\right)$. This approximate equation was stated before by [Nad+01; CD01]. However, by explicit conducting the approximation, the condition (5.14) for the validity of equation (5.16) was derived.

The probability density $p(D)$ is thus a Gaussian function

$$p(D) = \tilde{A} \exp\left(-\frac{1}{2}\left(\frac{D - D_{\mathrm{eq}}}{\sigma_{\mathrm{tm}}}\right)^2\right), \tag{5.17}$$

with standard deviation σ_{tm}, which is related to the curvature of the potential by

$$V''\left(D_{\mathrm{eq}}\right) = \frac{k_{\mathrm{B}}T}{\sigma_{\mathrm{tm}}^2}\,. \tag{5.18}$$

Most often (approximately 68 % of the time), $\Delta D < \sigma_{\mathrm{tm}}$. Using equation (5.14) yields a usable measure of the validity of approximation (5.17)

$$\sigma_{\mathrm{tm}} << 3\lambda_{\mathrm{D}}. \tag{5.19}$$

5.2 Data Analysis

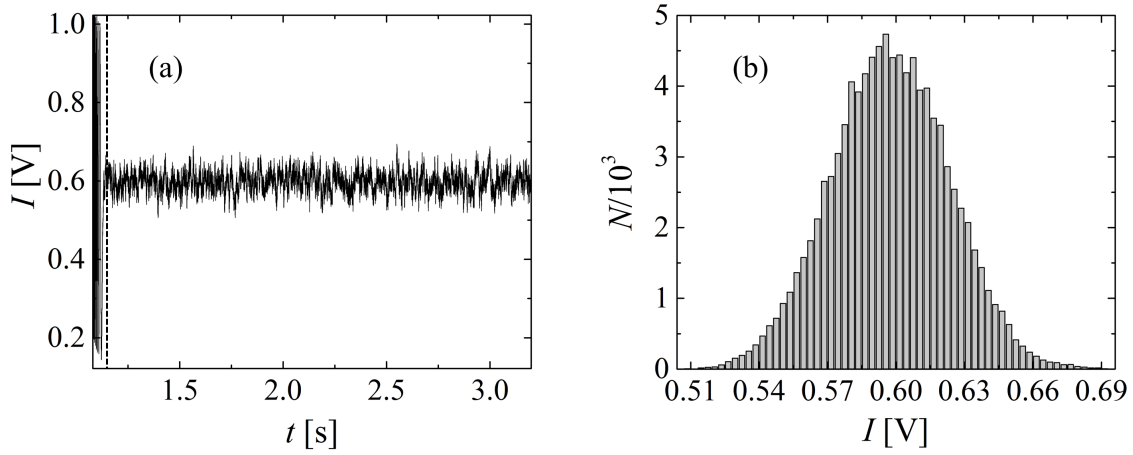

Figure 5.2: (a) Example of the reflection interference signal I of a bead's thermal motion close to the wall at a beam power of $P = 83\,\mathrm{mW}$ and a corresponding force on the bead $F_{\mathrm{bead}} = 19.6\,\mathrm{pN}$. Signal was recorded with a sampling rate of 50 kHz. Left of the dotted vertical line the last fringes due to the bead moving against the wall are included in the plot. Plot corresponds to the same single measurement as fig. 2.14. (b) Corresponding histogram of intensities of the reflection interference signal $N(I)$ determined for a sampling interval of $\tau = 2\,\mathrm{s}$ with a bin-size of $\Delta I = 3\,\mathrm{mV}$. Further experimental parameters: $R = (4.0 \pm 0.5)\,\mu\mathrm{m}$, $c_0 = 0.1\,\mathrm{mmol\,dm^{-3}}$, $p = 1\,\mathrm{bar}$ and $T = (21 \pm 1)\,^{\circ}\mathrm{C}$.

In this chapter, for better readability, the intensity of the reflection interference signal is simply stated as I without the subscript RI, i.e.

$$I \equiv I_{\mathrm{RI}} \,. \tag{5.20}$$

By analyzing the reflection interference signal of the bead's thermal motion around D_{eq} (fig. 5.2 (a), right of the dotted vertical line) at first the probability density of intensities $p(I)$ is determined, whereas $p(I)\,\mathrm{d}I$ is the probability to find the measured intensity of the interference signal in the interval $[I - \mathrm{d}I/2, I + \mathrm{d}I/2]$. Frequency counting is applied for a 2 s long interval of the interference signal $I(t)$ with a bin-size of $\Delta I = 3\,\mathrm{mV}$, determining the histogram $N(I)$, i.e. the number of samples of $I(t)$ that fall into the interval $[I - \Delta I/2, I + \Delta I/2]$ for different values of I (fig. 5.2 (b)). The corresponding probability is given by

$$\frac{N(I)}{N} = p(I)\Delta I \,. \tag{5.21}$$

Here N is the total number of samples, in particular $N = 10^5$ for 2 s interval sampled at a rate of 50 kHz. A sampling time of $\tau = 2\,\mathrm{s}$ was chosen in order to avoid the influence of long-term instability of the reflection interference signal due to possible drift of the sample or fluctuations of the intensity of the interference laser. Since the reference intensities I_{min} and I_{max} used for calculating the distance D were determined for every single measurement right before the thermal motion in equilibrium was analyzed (see fig. 2.14) the reflection interference signal only had to be stable for the sampling time of 2 s.

In the next step it will be shown how the probability density of distances $p(D)$ is determined, whereas $p(D)\,\mathrm{d}D$ is the probability to find the bead at a distance to the wall between $D - \mathrm{d}D/2$ and $D + \mathrm{d}D/2$. The probability of finding the bead in the distance interval $[D - \mathrm{d}D/2, D + \mathrm{d}D/2]$ is equal to the probability of finding the corresponding reflection interference signal in the interval $[I - \mathrm{d}I/2, I + \mathrm{d}I/2]$ [PLL87], i.e.

$$p(D)\,\mathrm{d}D = p(I)\,\mathrm{d}I \,. \tag{5.22}$$

Changing over from infinitesimal to finite intervals, we get the approximation

$$p(D)\Delta D(I) \approx p(I)\Delta I \,. \tag{5.23}$$

This approximation is valid for the case $p\left(\tilde{I}\right) \approx const$ for all $\tilde{I} \ni [I - \Delta I/2, I + \Delta I/2]$ and $p\left(\tilde{D}\right) \approx const$ for all $\tilde{D} \ni [D - \Delta D/2, D + \Delta I/2]$. Combining equations (5.21) and (5.23) yields

$$p(D) \approx \frac{N(I)}{N \cdot \Delta D(I)} \,. \tag{5.24}$$

As mentioned above, the data evaluation was performed with a constant bin-size ΔI. However, the corresponding $\Delta D(I)$ is a function of I, given by

$$\Delta D(I) = \left| D(I + \Delta I) - D(I - \Delta I) \right| \,, \tag{5.25}$$

whereas the relationship between distance and intensity $D(I)$ is given by equation (2.18).

Applying equation (5.24) to the measured histogram of intensities $N(I)$ (fig. 5.2) resulted in the probability density of distances $p(D)$ (fig. 5.3 (a)). For sufficiently long sampling times τ the probability density converges against a Boltzmann distribution. As expected from the approximation (5.16), the determined $p(D)$ was Gaussian and could be fitted with equation (5.17), yielding the equilibrium distance D_{eq} and the standard deviation σ_{tm}. For measurements at salt concentration $c_0 = 0.1\,\mathrm{mmol\,dm^{-3}}$ for F_{bead} from 4.6 pN to 37.6 pN the determined standard deviations σ_{tm} were in a range from 4.3 nm to 1.9 nm, which is well below the corresponding Debye length of $\lambda_{\mathrm{D}} \approx 23\,\mathrm{nm}$, thus satisfying condition (5.19).

Using equation (5.2) the potential $V(D)$ can be determined by

$$\frac{V(D)}{k_{\mathrm{B}}T} = -\ln\left(p(D)\right) - \ln(A) \,. \tag{5.26}$$

The potential $V(D)$ determined from the measured $p(D)$ was parabolic (fig. 5.3 (b)), furthermore demonstrating the validity of the harmonic approximation of $V(D)$ (equation (5.15)).

It is worth noting that the measured histogram $N(I)$ (fig. 5.2) corresponding to $p(D)$ in fig. 5.3 (a) as well is a Gaussian. Since $p(I)$ and $p(D)$ are related by

$$p(I) = \frac{p(D)}{\frac{\mathrm{d}I}{\mathrm{d}D}(D)} \,, \tag{5.27}$$

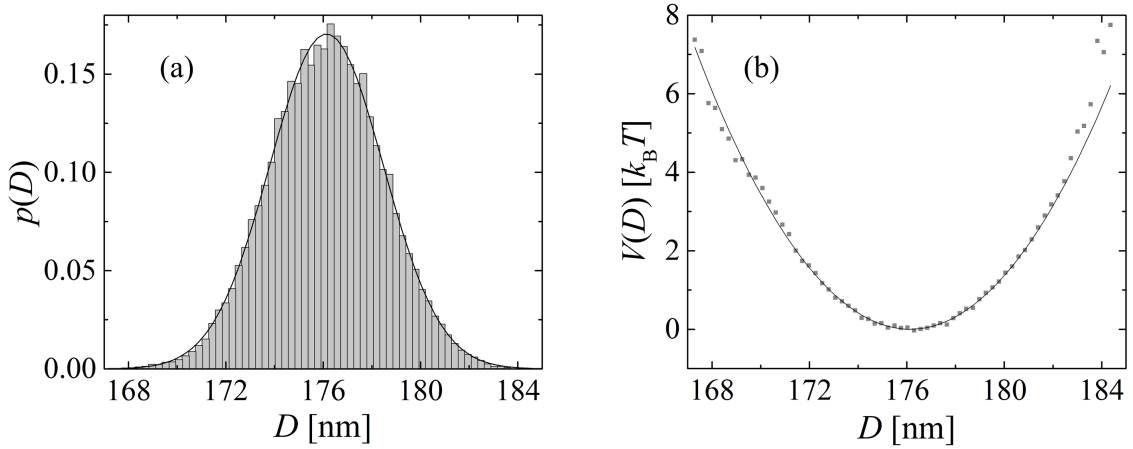

Figure 5.3: (a) Probability density $p(D)$ determined from histogram $N(I)$ in fig. 5.2. The probability density was fitted with equation (5.17) (black line), yielding $D_{\mathrm{eq}} = 176.4\,\mathrm{nm}$, $\sigma_{\mathrm{tm}} = 2.3\,\mathrm{nm}$ and $\tilde{A} = 0.999\,\mathrm{nm}/\sqrt{2\pi\sigma_{\mathrm{tm}}}$. The errors of the fit values were smaller than 1 % and in particular smaller than 0.1 % for D_{eq}. (b) Corresponding potential $V(D)$ calculated with equation (5.26) (gray squares). The black line is the fit from (a) inserted in (5.26).

the shape of $p(I)$ and thus $N(I)$ will be the same as the shape of $p(D)$ in case the slope $\mathrm{d}I/\,\mathrm{d}D$ of $I(D)$ is approximately constant in the range of distances assumed by the bead. This is the case if the measured reflection interference signal I is far from its extrema (see equation (2.16)). For example in fig 5.2 the interference signal $I(D)$ corresponding to the bead's thermal motion is approximately in the middle between I_{min} and I_{max} and thus on the side of the cosine function. In general, when recording the force curves the range of trapping beam powers P was set so, that the bead's thermal motion was performed on the same side of the cosine for all powers P. For most P the intensity I was far from the extrema.

5.2.1 Effect of Instrument Noise

Up until now it was assumed that the reflection interference signal I was free of any noise that was not due to the thermal motion of the bead. However, any real experiment is influenced by instrument noise, i.e. noise that is caused by the means to investigate the system. One type of instrument noise is what we will call *laser noise*, i.e. the noise of the intensity recorded with the avalanche photo-diode that remains when the bead

is removed from the beam path. Thus, this noise could be measured directly (see part 2.1.2 Laser Noise). Laser noise includes all noise that causes fluctuations in the intensity of the interference beam, i.e. fluctuations of the intensity of the interference laser and vibrations of the optics in the beam path of the interference beam. Since every single measurement is evaluated independently, any fluctuations on timescales longer than the sampling time $\tau = 2\,\mathrm{s}$ do not influence the data evaluation.

Here, the effect of laser noise on the measured probability density $p(D)$ will be investigated. We will later argue that the findings for the effect of laser noise could be applied to other instrument noise as well.

From investigating the recorded signal of the interference beam reflected from the wall without a bead in the beam path (fig. 2.6) it can be concluded that the intensity of the interference beam $I_0(t)$ can be represented by the sum of a constant mean intensity $\overline{I_0}$ and a time dependent noise contribution $I_{\mathrm{ln}}(t)$

$$I_0(t) = \overline{I_0} + I_{\mathrm{ln}}(t) \; . \tag{5.28}$$

The measured probability density of the interference beam $p_0(I_0)$ was well represented by a Gaussian function with mean value $\overline{I_0}$ and standard deviation $\sigma_{\mathrm{ln}}^{\mathrm{I}} = 0.8\,\% \cdot \overline{I_0}$ (see part 2.1.2). In other words, the probability density of the noise contribution $p_{\mathrm{ln}}(I_{\mathrm{ln}}) = p_0\Big(I_0 - \overline{I_0}\Big)$ is a Gaussian function with a mean value of zero and standard deviation $\sigma_{\mathrm{ln}}^{\mathrm{I}} = 0.8\,\% \cdot \overline{I_0}$.

The reflection interference signal I is a function of the distance D and the intensity of the interference beam, i.e. $I(D, I_0(t)) = I\Big(D, \overline{I_0} + I_{\mathrm{ln}}(t)\Big)$. From $\sigma_{\mathrm{ln}}^{\mathrm{I}}/\overline{I_0} = 0.8\,\%$ we know that $I_{\mathrm{ln}}(t) << \overline{I_0}$. Expansion yields

$$I(D, I_0(t)) \approx I\Big(D, \overline{I_0}\Big) + \frac{\mathrm{d}I}{\mathrm{d}I_0}\Big(D, \overline{I_0}\Big) \cdot I_{\mathrm{ln}}(t) \; . \tag{5.29}$$

Since the reflection interference signal is proportional to the intensity of the interference beam [LS09], i.e. $I(D, I_0(t)) \propto I_0(t)$ we get

$$I\Big(D, \overline{I_0}\Big) = \frac{\mathrm{d}I}{\mathrm{d}I_0}\Big(D, \overline{I_0}\Big) \cdot \overline{I_0} \; . \tag{5.30}$$

Combining equations (5.29) and (5.30) yields

$$I(D, I_0(t)) \approx I\left(D, \overline{I_0}\right) + I\left(D, \overline{I_0}\right) \cdot \frac{I_{\ln}(t)}{\overline{I_0}} \,. \tag{5.31}$$

For the product on the right side of equation (5.31) the fluctuation of the factor $I\left(D, \overline{I_0}\right)$ due to thermal noise of the bead arround D_{eq} is negligible compared to the fluctuation of the factor $I_{\ln}(t)/\overline{I_0}$, establishing the approximation

$$I(D, I_0(t)) \approx I\left(D, \overline{I_0}\right) + I\left(D_{\text{eq}}, \overline{I_0}\right) \cdot \frac{I_{\ln}(t)}{\overline{I_0}} \,. \tag{5.32}$$

Recollecting that $I\left(D, \overline{I_0}\right) \equiv I(D)$ is the instrument noise-free reflection interference signal, equation (5.32) signifies that laser noise introduces additive noise to the measured reflection interference signal.

The measured distance D_{m} is a function of the reflection interference intensity I (equation (2.18)). The latter is a function of the *actual* distance D and the intensity of the interference beam $I_0(t)$, i.e.

$$D_{\text{m}} = D\Big(I(D, I_0(t))\Big) \,. \tag{5.33}$$

Since $I_{\ln}(t)/\overline{I_0} << 1$, expansion yields

$$D_{\text{m}} \approx \underbrace{D\Big(I\left(D, \overline{I_0}\right)\Big)}_{\equiv D} + \underbrace{\frac{\mathrm{d}D}{\mathrm{d}I}(I) \cdot I\left(D_{\text{eq}}, \overline{I_0}\right) \cdot \frac{I_{\ln}(t)}{\overline{I_0}}}_{=:D_{\ln}} \,. \tag{5.34}$$

It was thus shown that the measured distance D_{m} is the sum of the actual bead-wall distance D and a noise contribution $D_{\ln}$. The final step is to determine the effect of additive distance-noise on the measured probability density $p_{\text{m}}(D_{\text{m}})$. Let $p_{\ln}(D_{\ln})$ be the probability density due to laser noise and $p_{\text{tm}}(D)$ be the probability density due to thermal motion (note: usually the probability density due to the thermal motion of the bead was simply stated as $p(D)$. Here the subscript "tm" was used for unambiguity). Odiachi and Prieve have found that the measured probability density of a signal subject to additive noise is equal to the convolution of the probability densities of the noise-free signal and the noise contribution [OP04]. Application to the here presented case yields

$$p_{\mathrm{m}}(D_{\mathrm{m}}) = \int_{-\infty}^{\infty} p_{\mathrm{tm}}(D_{\mathrm{m}} - D_{\mathrm{ln}}) p_{\mathrm{ln}}(D_{\mathrm{ln}})\, \mathrm{d}D_{\mathrm{ln}} \,. \tag{5.35}$$

It was shown that $p_{\mathrm{tm}}(D)$ was a Gaussian function (see equation (5.16) and fig. 5.3 (a)). The probability density of intensities $p_{\mathrm{ln}}(I_{\mathrm{ln}})$ of the laser noise contribution is related to the probability density of distances $p_{\mathrm{ln}}(D_{\mathrm{ln}})$ by equation (5.27). Since $p_{\mathrm{ln}}(I_{\mathrm{ln}})$ is a Gaussian function, $p_{\mathrm{ln}}(D_{\mathrm{ln}})$ is also expected to be Gaussian, because the slope of the reflection interference signal $I(D)$ is approximately constant over the range of I_{ln} values contributing to $p_{\mathrm{ln}}(D_{\mathrm{ln}})$. The definition of D_{ln} in equation (5.34) yields the standard deviation $\sigma_{\mathrm{ln}}^{\mathrm{D}}$ of $p_{\mathrm{ln}}(D_{\mathrm{ln}})$

$$\sigma_{\mathrm{ln}}^{\mathrm{D}} = \left| \frac{\partial D}{\partial I}\left(\overline{I_0}\right) \right| \cdot I\left(D_{\mathrm{eq}}, \overline{I_0}\right) \cdot \frac{\sigma_{\mathrm{ln}}^{\mathrm{I}}}{\overline{I_0}} \,. \tag{5.36}$$

Here $\sigma_{\mathrm{ln}}^{\mathrm{I}}$ is the standard deviation of $p_{\mathrm{ln}}(I_{\mathrm{ln}})$. For simplicity the notation $\sigma_{\mathrm{ln}} \equiv \sigma_{\mathrm{ln}}^{\mathrm{D}}$ will be used for the standard deviation of distances.

By using properties of a convolution of two Gaussian functions, three key properties of the measured probability density $p_{\mathrm{m}}(D_{\mathrm{m}})$ can be derived from equation (5.35):

- The convolution $p_{\mathrm{m}}(D_{\mathrm{m}})$ is as well a Gaussian function with mean value $\overline{D_{\mathrm{m}}}$ and standard deviation σ_{m}.
- The mean of the convolution is the sum of means of the convoluted functions:

$$\overline{D_{\mathrm{m}}} = \overline{D} + \overline{D_{\mathrm{ln}}} = D_{\mathrm{eq}} + 0 \,. \tag{5.37}$$

- The variance of the convolution is the sum of variances of the convoluted functions:

$$\sigma_{\mathrm{m}}^2 = \sigma_{\mathrm{tm}}^2 + \sigma_{\mathrm{ln}}^2 \,. \tag{5.38}$$

We thus conclude that the determined equilibrium position D_{eq} is independent of laser noise. The effect of laser noise is to increase the width of the measured probability density. This finding (i.e. equation (5.38)) is equivalent to an assumption by Oetama and Walz for any instrument noise that increases "the dynamic fluctuations in the scattering signal [of total internal reflection microscopy measurements, D.W.P.]" [OW05]. They were able to successfully apply their assumption in order to correct for instrument

noise when determining the diffusion coefficient of a colloidal bead in water. It is thus a reasonable proposition that equation (5.38) is applicable not only to laser noise but as well to other instrument noise that causes additional dynamic fluctuations to the measured reflection interference signal

$$\sigma_{\mathrm{m}}^2 = \sigma_{\mathrm{tm}}^2 + \sigma_{\mathrm{in}}^2 \,. \tag{5.39}$$

Assuming that the other noise contributions are approximately Gaussian and independent of the laser noise, the total variance of the instrument noise σ_{in}^2 is given by

$$\sigma_{\mathrm{in}}^2 = \sigma_{\mathrm{ln}}^2 + \sigma_{\mathrm{on}}^2 \,. \tag{5.40}$$

Here σ_{on} accounts for other noise contributions that could not be measured directly, e.g. noise due to pointing instability of the trapping laser. Since only the central part of the reflection interference is collected by the optical fiber and thus recorded by the avalanche photo-diode, spatial fluctuations of the reflection interference translate to fluctuations in the measured intensity I (see part 2.1.2). Lateral changes in the bead position could, due to the lensing effect of the bead laterally divert the reflection.

5.2.2 Sufficiency of the Sampling Time

In order for the measured probability density $p(D)$ to converge against the Boltzmann distribution (equation (5.16)) the bead must be given enough time to explore the potential $V(D)$. The probability is highest for finding the bead at D_{eq}, i.e. the minimum of the potential $V(D)$. With increasing distance ΔD from D_{eq}, the probability of occupation by the bead decreases. This means, the larger the interval $\left[D_{\mathrm{eq}} - \Delta D, D_{\mathrm{eq}} + \Delta D\right]$ on which $V(D)$ is supposed to be determined accurately, the larger the needed sampling time τ.

Compared to typical total internal reflection microscopy experiments, where the thermal motion is sampled for several minutes up to hours [PLL87; PF90; Vol+10], the here chosen sampling time of $\tau = 2\,\mathrm{s}$ appears rather short. Determining a sufficient τ is not trivial. Sholl *et al.* performed Brownian Dynamic simulations in order to investigate the relationship between sampling time τ and accuracy of determining the potential $V(D)$, quantified by the largest accurately determined potential V_{max} [Sho+00]. By using equations (5.16) and (5.18), the range of accurately determined potentials can be related

to the range of accurately determined distances by

$$\frac{(\Delta D)^2}{\sigma^2} = \frac{V_{\max}}{k_B T} \,. \tag{5.41}$$

This means, for $V_{\max} = 1\ k_B T$ an interval $\left[D_{eq} - \sigma, D_{eq} + \sigma\right]$ is well resolved. Since for the here presented data analysis only the peak of $p(D)$ is evaluated, the determined $p(D)$ must only be accurate over a small range around D_{eq}. Hence, $V_{\max} = 1\ k_B T$ is certainly a sufficient threshold.

Sholl *et al.* evaluated the case where the wall was below the bead and the bead was pushed against the wall by the difference of gravity and buoyancy [Sho+00]. For a bead with radius $R = 5\,\mu\text{m}$ and density $\rho_{\text{bead}} = 2.2\,\text{g}\,\text{cm}^{-3}$ they found $\tau = 6\,\text{s}$ for an accuracy of $V_{\max} = 2\ k_B T$. The concentration c_0 of the 1:1 electrolyte was $0.5\,\text{mmol}\,\text{dm}^{-3}$, however Sholl *et al.* found that τ was insensitive to the use of different electrolyte concentrations in a range from $0.1\,\text{mmol}\,\text{dm}^{-3}$ to $2\,\text{mmol}\,\text{dm}^{-3}$. The radius used in the simulation is comparable to the radius of the bead's used in the work presented here ($R \approx 4\,\mu\text{m}$). The force pushing the bead against the wall was $F_{\text{bead}} = \frac{4}{3}\pi R^3 \left(\rho_{\text{bead}} - \rho_{\text{water}}\right) g = 6.2\,\text{pN}$, where the gravitational acceleration $g = 9.81\,\text{m}\,\text{s}^{-2}$ and the density of water $\rho_{\text{water}} = 1\,\text{g}\,\text{cm}^{-3}$ were used. The required sampling time τ for $V_{\max} = 1\ k_B T$ can be calculated using the finding of Sholl *et al.*, that $V_{\max} \propto \ln(\tau)$, which yields

$$\tau = 2.2\,\text{s} \,. \tag{5.42}$$

Since in the here presented work F_{bead} was in a range from 4 pN to 90 pN and the needed τ was found to decrease with increasing ρ_{bead} [Sho+00] and thus with increasing F_{bead}, we can conclude that $\tau = 2\,\text{s}$ is a sufficiently large sampling time for data evaluation.

5.3 Summary

In this chapter the thermal motion of the bead around the equilibrium position D_{eq} in the potential $V(D)$ was investigated. A harmonic approximation of $V(D)$ was found valid for the given experimental configuration, yielding a Gaussian probability density of the bead's position. Since D_{eq} was defined as the position, where the total force on the bead is zero, it could be determined as the center of the Gaussian. It was further found that

instrument noise leaves the measured D_{eq} unaltered while increasing the width of the probability density. Finally, it was argued that recording the bead's thermal motion for a time of 2 s is sufficient to evaluate the potential $V(D)$ in proximity to D_{eq}.

6 Pressure Dependence of the Electrostatic Double-Layer Force

In water most surfaces are charged [BK10]. Glass surfaces are negatively charged in water at $p\mathrm{H} > 2$ due to the dissociation of silanol groups [BG01; Lam+08]. The electrostatic field generated by the surface charges causes counter-ions to accumulate close to the surface [BK10]. The system composed of the surface ions together with the dissolved ions that are close to the surface is called *electric double-layer*. The force between two charged surfaces in water is not simply the Coulomb-force, since the electrostatic field of the surface charges is screened by dissolved ions. The overlap of the double-layers of the surfaces causes a force between the surfaces which is called *electrostatic double-layer force*. This force is well understood at ambient pressure, but has never been directly measured at high hydrostatic pressure. In this chapter I will present the first measurement of the electrostatic double-layer force at hydrostatic pressures between 1 bar and 1 kbar.

For a sphere and a plane separated by a distance D "in all cases when the interaction [between the individual electric double-layers, D.W.P.] is not very strong"[VO48] and $D >> \lambda_\mathrm{D}$, the electrostatic double-layer force F_DL can be calculated by [Isr11; BK10; VO48]

$$F_\mathrm{DL}(D) = 64\pi R \frac{\epsilon_0\,\epsilon}{\lambda_\mathrm{D}} \frac{k_\mathrm{B}T}{e^2} \alpha^2 \exp\left(-\frac{D}{\lambda_\mathrm{D}}\right) = F_0 \exp\left(-\frac{D}{\lambda_\mathrm{D}}\right), \tag{6.1}$$

with

$$\alpha = \tanh\left(\frac{e\psi_0}{4k_\mathrm{B}T}\right). \tag{6.2}$$

Here R is the radius of the sphere, ψ_0 is the surface potential, which is assumed to be identical for both surfaces, ϵ_0 and ϵ are the vacuum permittivity and the dielectric constant of the liquid and e is the elementary charge. The Debye-length λ_D is given by

$$\frac{1}{\lambda_D} = \sqrt{\frac{e^2}{\epsilon_0 \epsilon k_B T} \sum c_i Z_i^2} \,. \tag{6.3}$$

Here, c_i and Z_i are the concentration and the valency of the i-th ion sort in the liquid. For room-temperature ($T = 20\,°C$) we get $k_B T/e \approx 25\,\mathrm{mV}$. For low surface potentials, i.e. $\psi_0 << 4k_B T/e \approx 100\,\mathrm{mV}$, we can approximate $\alpha \approx e\psi_0/4k_B T$ and thus simplify the expression for the electrostatic double-layer force

$$F_{DL}(D) = \frac{4\pi R \psi_0^2 \epsilon_0 \epsilon}{\lambda_D} \exp\left(-\frac{D}{\lambda_D}\right) = F_0 \exp\left(-\frac{D}{\lambda_D}\right), \tag{6.4}$$

which is equivalent to the result reported by Butt in case of large distances (approximately $D > 5\lambda_D$) [But91b; But91a]. The approximation of α has been used before for borosilicate glass in water [JB13]. Another important quantity that characterizes a charged surface is the surface charge density σ_s. σ_s is related to ψ_0 by the Grahame equation [BK10]

$$\sigma_s = \sqrt{8 c_0 \epsilon_0 \epsilon k_B T} \cdot \sinh\left(\frac{e\psi_0}{2k_B T}\right) \,. \tag{6.5}$$

For small arguments of sinh, i.e. $\psi_0 << 2k_B T/e$, we can approximate $\sinh(x) \approx x$ and get the linearized Grahame equation

$$\sigma_s = \frac{\epsilon_0 \epsilon \psi_0}{\lambda_D} \,. \tag{6.6}$$

The theoretical description presented above establishes a relationship between the electrostatic double-layer force and properties of the liquid and the surfaces. Based on this description we can predict effects on $F_{DL}(D)$ due to pressurization of the liquid.

6.0.1 Effects of Pressure

Based on the increase of ϵ with pressure [UF80; FN04] (fig. 6.1 (a)), a pressure effect on the electrostatic double-layer force is deducible. In a pressure range from 1 bar to 1 kbar at room-temperature ϵ increases by approximately 5 %. Using equation (6.3) it can be expected for λ_D at two different pressures p_1 and p_2 that

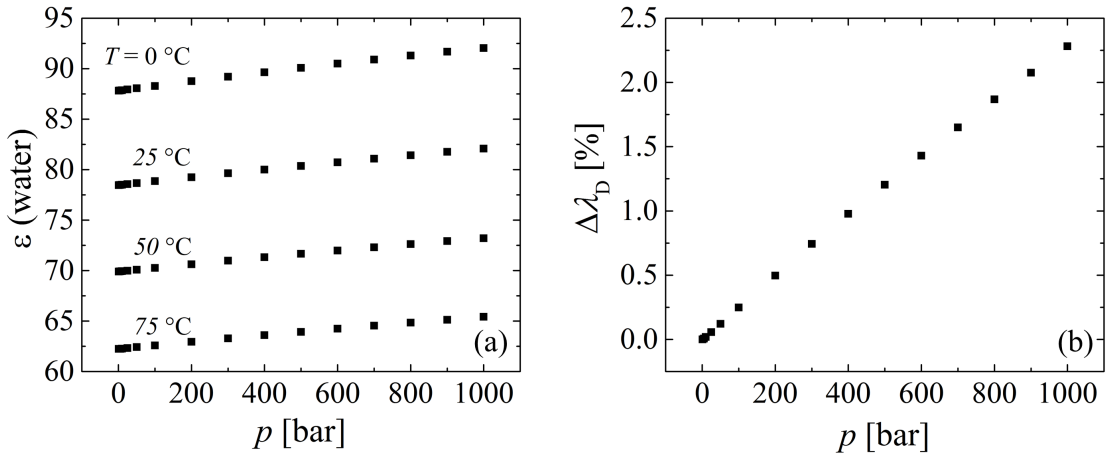

Figure 6.1: (a) Dielectric constant of water ϵ versus hydrostatic pressure p at different temperatures T. Plot based on data from [UF80]. At $T = 25\,°C$, ϵ increases from 78.46 at $p = 1\,\text{bar}$ to 82.08 at $p = 1\,\text{kbar}$. (b) Increase of λ_D with p at $T = 25\,°C$ relative to $\lambda_D\big(p = 1\,\text{bar}\big)$ calculated with (6.7). This increase was approximately the same for all temperatures from 0 °C to 75 °C.

$$\lambda_D\left(p_2\right) = \lambda_D\left(p_1\right)\sqrt{\frac{\epsilon\left(p_2\right)}{\epsilon\left(p_1\right)}}\,. \tag{6.7}$$

For an increase of the hydrostatic pressure from $p_1 = 1\,\text{bar}$ to $p_1 = 1\,\text{kbar}$ at a room-temperature λ_D is expected to increase by approximately 2.3 % (fig. 6.1 (b)).

In order to predict the pressure dependence of the force amplitude F_0, the pressure dependence of ψ_0 and σ_s must be investigated. ψ_0 and σ_s are related to each other by the Grahame equation (6.5). The linearized Grahame equation (6.6) together with $\lambda_D \propto \sqrt{\epsilon_0\epsilon}$ (6.3) results in:

$$\frac{\sigma_s}{\psi_0} = \frac{\epsilon_0\epsilon}{\lambda_D} \propto \sqrt{\epsilon_0\epsilon}\,. \tag{6.8}$$

Thus, in order to predict the pressure dependence of F_0, boundary conditions for ψ_0 and σ_s need to be specified. In analogy to the boundary conditions used for deriving the electrostatic double-layer force [BK10; PG72; VO48] the two extreme cases are

1. **CC:** Constant charge. The charge density σ_s remains constant during pressurization.

2. **CP:** Constant potential. The surface potential ψ_0 remains constant during pressurization.

CC: Assuming constant charge boundary condition, the expected pressure effect of ψ_0 can be estimated by using equation (6.8)

$$\psi_0\left(p_2\right) = \psi_0\left(p_1\right)\sqrt{\frac{\epsilon\left(p_1\right)}{\epsilon\left(p_2\right)}}\,. \tag{6.9}$$

Using the above equation together with (6.4) yields an estimation of the expected pressure effect on the amplitude of the double-layer force for the constant charge boundary condition

$$F_0^{CC}\left(p_2\right) = F_0\left(p_1\right)\frac{\epsilon\left(p_2\right)}{\epsilon\left(p_1\right)}\frac{\lambda_\mathrm{D}\left(p_1\right)}{\lambda_\mathrm{D}\left(p_2\right)}\left(\frac{\psi_0\left(p_2\right)}{\psi_0\left(p_1\right)}\right)^2 = F_0\left(p_1\right)\sqrt{\frac{\epsilon\left(p_1\right)}{\epsilon\left(p_2\right)}}\,. \tag{6.10}$$

CP: Using the constant potential boundary condition $\psi_0\left(p_1\right) = \psi_0\left(p_2\right)$ yields

$$F_0^{CP}\left(p_2\right) = F_0\left(p_1\right)\frac{\epsilon\left(p_2\right)}{\epsilon\left(p_1\right)}\frac{\lambda_\mathrm{D}\left(p_1\right)}{\lambda_\mathrm{D}\left(p_2\right)} = F_0\left(p_1\right)\sqrt{\frac{\epsilon\left(p_2\right)}{\epsilon\left(p_1\right)}}\,. \tag{6.11}$$

For an increase of the hydrostatic pressure from $p_1 = 1\,\mathrm{bar}$ to $p_1 = 1\,\mathrm{kbar}$ equation (6.10) predicts an increase of F_0 by 2.3 % while equation (6.11) predicts a decrease of F_0 by 2.2 %. Which boundary condition applies when changing the hydrostatic pressure is debated in literature [GT08; DM09; Gho09]. Detecting the subtle effect of pressure on F_0 could clarify the underlying boundary condition on σ_S and ψ_0.

Effect of hydrostatic pressure on the ζ-potential

The ζ-potential is a characteristic property of the electric double-layer used e.g. in the context of electrophoresis [HR97]. While ψ_0 is the potential at the solid-liquid interface, ζ is defined as the potential at the "plane of shear"[BVS09]. Although there does not seem to be any direct evidence of the existence of the plane of shear [GXX12], the plane is assumed to be located a few molecular layers away from the solid-liquid interface [HR97]. However, it is known that $\zeta < \psi_0$ [HR97]. In order to estimate the order of magnitude of the effect or pressure on the electrostatic double-layer force we will further

assume that the potential-drop between the solid-liquid interface and the plane of shear is less than $1/e$, i.e. $3\zeta > \psi_0$.

The effect of hydrostatic pressure up to 4 bar on the ζ-potential of quartz in aqueous electrolyte solutions at room temperature was investigated by means of electrophoresis [RA06]. The ζ-potential of quartz was found to increase from approximately -50 mV to -10 mV when increasing the pressure from 1 bar to 4 bar in an 10 mmol dm^{-3} aqueous NaCl solution at pH = 4. After excluding phase transformations of the quartz as the reason for this increase, the authors stated that "the increase in pressure can only change the suspension ordering at the solid-liquid interface in a monotonic variation"[RA06]. However, the meaning of "suspension ordering" is not further discussed by the authors, but it is clear that the authors explain their finding with a modification of the liquid by pressure. Thus, an effect of pressure on the ζ-potential should as well be observable for other solid materials in aqueous electrolyte.

In a more recent work the stability of fumed silica suspensions was inverstigated in a pressure range from 1 bar to 150 bar [AOS11]. It was found that the shear thickening behavior of fumed silica suspended in 50/50 mixtures of water and glycerol at an NaCl concentration of 0.1 mol dm^{-3} increased with hydrostatic pressure. This behavior was explained by a weakening of the electrostatic double-layer force due to a decrease in the magnitude of the ζ-potential with pressure, whereas the authors based their conclusion on the electrophoresis experiments by [RA06].

The Debye-length λ_D should not be affected by changes of the ζ-potential (see equation (6.3)). F_0 however depends on ψ_0. Using equations (6.1) and (6.2) and neglecting the pressure effect of ϵ results in

$$\frac{F_0\left(p_2\right)}{F_0\left(p_1\right)} \approx \left(\tanh\left(\frac{e\psi_0\left(p_2\right)}{4k_B T} \right) / \tanh\left(\frac{e\psi_0\left(p_1\right)}{4k_B T} \right) \right)^2 . \tag{6.12}$$

Using values of the ζ-potential reported in reference [RA06] results in

$$F_0\left(p = 4\,\text{bar}\right) / F_0\left(p = 1\,\text{bar}\right) \approx 0.05 \tag{6.13}$$

when assuming $\psi_0 = \zeta$, and

$$F_0\left(p = 4\,\mathrm{bar}\right)/F_0\left(p = 1\,\mathrm{bar}\right) \approx 0.1 \tag{6.14}$$

for $\psi_0 = 3\zeta$. Although such a steep decrease of the ζ-potential would not be likely to continue for pressures larger than 4 bar, for an increase of the hydrostatic pressure from 1 bar to 1 kbar the amplitude of the double-layer force F_0 is expected to decrease by at least one order of magnitude.

6.0.2 Influence of Roughness on the Electrostatic Double-Layer Force

The roughness of solid surfaces influences the surface forces between them [SW97; WSP99; Zwo+08; GXX12]. The effect of roughness on the electrostatic double-layer force was recently investigated by Parsons *et al.* [PWC14]. They found that roughness has no effect on the measured Debye length λ_D but increases the amplitude of the force by a factor of

$$F_\mathrm{DL} \propto \exp\left(\frac{\sigma_\mathrm{m}^2}{2\lambda_\mathrm{D}^2}\right), \tag{6.15}$$

where $\sigma_\mathrm{m} = \sqrt{\sigma_1^2 + \sigma_2^2}$, and $\sigma_{1/2}$ is the RMS-roughness of each surface. Using scanning probe microscopy the RMS-roughness σ_1 of the here used beads was determined to be on average 3.3 nm (equation (2.11)). The glass wall showed a mean roughness of $\sigma_2 = 0.3\,\mathrm{nm}$ (equation (2.12)). For $\lambda_\mathrm{D} = 23\,\mathrm{nm}$ and $\lambda_\mathrm{D} = 9\,\mathrm{nm}$ equation (6.15) predicts an increase of F_DL by 1 % and 7 %, respectively. Compared to the > 20 % inaccuracy of determining the absolute value of F_DL due to the inaccuracy of the radius of the bead R (see part 3.2.1) the increase of the measured F_DL due to roughness is minor. Furthermore, since the roughness of the bead has no influence on the precision of the force measurement, the error is insignificant when comparing force curves recorded with the same bead.

6.1 Ambient Pressure Experiment

The bead was pushed against the capillary wall by the trapping beam at different powers P. At each power, the analysis of the hydrodynamic drag F_hd on a bead approaching

the wall (see chapter 3) and the analysis of the thermal motion of the same bead close to the wall (see chapter 5) yielded a data point $\left(D_{\mathrm{eq}}, F_{\mathrm{DL}}\right)$. These data points composed a force curve. In case of the electrostatic double-layer force an exponential dependence is expected (equation (6.1)). The latter can be visualized by a semi-logarithmic plot of the force curve (fig. 6.2).

The force decayed more steeply for the salt concentration of $c_0 = 1\,\mathrm{mmol\,dm^{-3}}$ than for $c_0 = 0.1\,\mathrm{mmol\,dm^{-3}}$ due to the enhanced screening of the electrostatic field by the increased amount of ions in the electrolyte. For the same reason, the force curve for $1\,\mathrm{mmol\,dm^{-3}}$ was recorded at smaller absolute distances (60 nm to 80 nm) then the one for $0.1\,\mathrm{mmol\,dm^{-3}}$ (160 nm to 210 nm). The force curves could be effectively fitted with equation (6.1) using orthogonal regression, which accounts for x and y errors. The fitting revealed $\lambda_{\mathrm{D}} = (24.0 \pm 0.3)\,\mathrm{nm}$ and $\lambda_{\mathrm{D}} = (8.8 \pm 0.2)\,\mathrm{nm}$ for $0.1\,\mathrm{mmol\,dm^{-3}}$ and $1\,\mathrm{mmol\,dm^{-3}}$, respectively. Given the uncertainties of c_0 (see part 2.3), pH and T the Debye lengths were calculated by using equation (6.3). Here I obtained values for the Debye lengths of $\lambda_{\mathrm{D}} = 24.2 - 30.1$ nm and $\lambda_{\mathrm{D}} = 8.9 - 10.3$ nm, respectively, which are in quantitative agreement with the measured values.

In order to visualize the precision of the measurements, the force curves were plotted with two sets of error bars (fig. 6.2). The black error bars correspond to errors of the precision and are thus relevant for the comparison of data points corresponding to the same force curve. The gray error bars furthermore include errors of the accuracy of the measurement, e.g. the inaccuracy of the force values due to the error of the bead radius ΔR (see part 3.2.1).

In order to estimate the distance resolution of the technique, the force curve at $1\,\mathrm{mmol\,dm^{-3}}$ was evaluated. Force curves were recorded by increasing F_{bead} in equidistant steps ΔF_{bead}. The corresponding difference in D is given by

$$\Delta D = \Delta F_{\mathrm{bead}} \cdot \left(\frac{\mathrm{d}F_{\mathrm{DL}}}{\mathrm{d}D}\right)^{-1} \quad . \tag{6.16}$$

Since the slope of $F_{\mathrm{DL}}(D)$ increases with increasing force, the spatial resolution is demonstrated best for data points corresponding to the largest measured forces, i.e. $F_{\mathrm{DL}} > 53\,\mathrm{pN}$. Here, six distinguishable data points were recorded consecutively in a range from 59 nm to 63 nm (fig. 6.2 (b)), demonstrating sub-nanometer distance resolu-

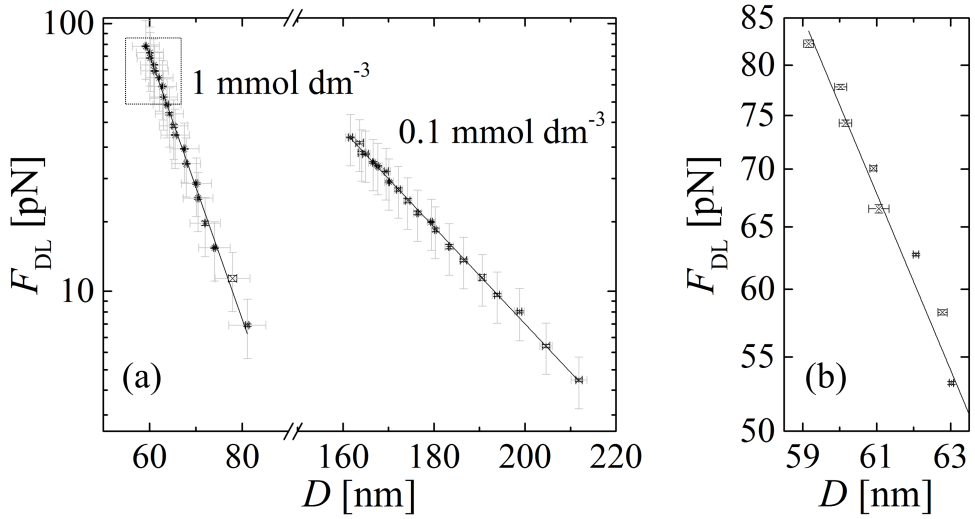

Figure 6.2: (a) Semi-logarithmic plot of force curves recorded at 1 bar for NaCl concentrations of 0.1 mmol dm^{-3} and 1 mmol dm^{-3} in water at *p*H = 4 - 4.5 and $T = (21 \pm 1)\,°C$. Force curves were recorded by increasing F_{bead} in equidistant steps of $\Delta F_{bead} \approx 1.6$ pN from 4.7 pN to 37.6 pN and $\Delta F_{bead} \approx 3.7$ pN from 7.5 pN to 82.2 pN for 0.1 mmol dm^{-3} and 1 mmol dm^{-3}, respectively. Black error bars correspond to errors of the precision. Gray error bars furthermore include errors of the accuracy. Solid lines are fits with equation (6.1) with fit values $\lambda_D = (24.0 \pm 0.3)$ nm, $F_0 = (31 \pm 3)$ nN and $\lambda_D = (8.8 \pm 0.2)$ nm, $F_0 = (69 \pm 9)$ nN for 0.1 mmol dm^{-3} and 1 mmol dm^{-3}, respectively. (b) Zoom-in of (a). Only errors of the precision were plotted. ©2016 American Physical Society [Pil+16]

tion of the reflection interference technique.

6.2 Experiments at Different Pressures

Several force curves were recorded in aqueous NaCl solutions with concentrations of 0.1 mmol dm^{-3} and 1 mmol dm^{-3} at different hydrostatic pressures *p* between 1 bar and 1 kbar (fig. 6.3). Since the radius, the roughness and the surface charge density of a bead influence the measured double-layer force (see equation (6.1) and part 6.0.2), the same bead was used to record all force curves at a given salt concentration. At least three consecutive force curves were recorded at a given pressure.

All effects due to hydrostatic pressure on the experimental system under investigations

were expected to be reversible. Any irreversible changes of the force curves would point towards leakage, contamination or other unwanted effects. In order to ascertain reversibility regarding pressure effects, measurements were performed alternately at ambient and high pressure, i.e. first at ambient pressure (1 bar Nr. 1), then at high pressure (0.5 kbar and 1 kbar Nr.1), again at ambient pressure (1 bar Nr. 2), again at high pressure (1 kbar Nr.2) and finally at ambient pressure (1 bar Nr.3).

All measured force curves display the exponentially decaying behavior as expected for the electrostatic double-layer force from equation (6.1). Table 6.1 summarizes the averaged fit values obtained from the fits with equation (6.1). In nearly all cases, λ_D varied by less than 1 nm for consecutive force curves, demonstrating a nanometer precision in determining λ_D. The only exception was the first 1 kbar measurement at a salt concentration of 0.1 mmol dm^{-3}, where λ_D varied by less than 1.5 nm. However, the expected change of λ_D due to the pressure induced increase of ϵ was on the sub-nanometer scale (see part 6.0.1). For an increase of p from 1 bar to 1 kbar an increase of λ_D by 0.5 nm and 0.2 nm was expected for the 0.1 mmol dm^{-3} and 1 mmol dm^{-3} sample, respectively. Corresponding to the experimental precision, the Debye lengths λ_D for different pressures p were found constant within approximately 1 nm (table 6.1).

c_0[mmol dm^{-3}]	p =	1 bar	0.5 kbar	1 kbar
0.1	λ_D[nm] =	23.3 ± 0.6	22.7 ± 0.3	22.5 ± 1.1
0.1	F_0[nN] =	43 ± 9	53 ± 9	64 ± 30
1	λ_D[nm] =	9.0 ± 0.6	9.0 ± 0.4	9.5 ± 0.9
1	F_0[nN] =	55 ± 26	43 ± 8	61 ± 40

Table 6.1: Average fit values for force curves in figure 6.3 fitted with equation (6.1).

In the experiment with $c_0 = 0.1$ mmol dm^{-3} the force on the bead increased with increasing pressure (fig. 6.3 (a)), except for the second measurement at 1 bar (black stars). Here the measured force on the bead seemed to be largest although these force curves were recorded at ambient pressure. Since these force curves were recorded at ambient pressure, the increased force could not be explained by an effect of pressure. Also, since the force curves of the first and last measurement at 1 bar overlap (black squares and triangles) the increase of the force for the second at 1 bar could not be due to an irreversible effect of pressure, like e.g. leakage of the sealed capillary. Similar outliers were recorded for the experiment with a salt concentration of 1 mmol dm^{-3} (fig. 6.3 (b)). Opposed to

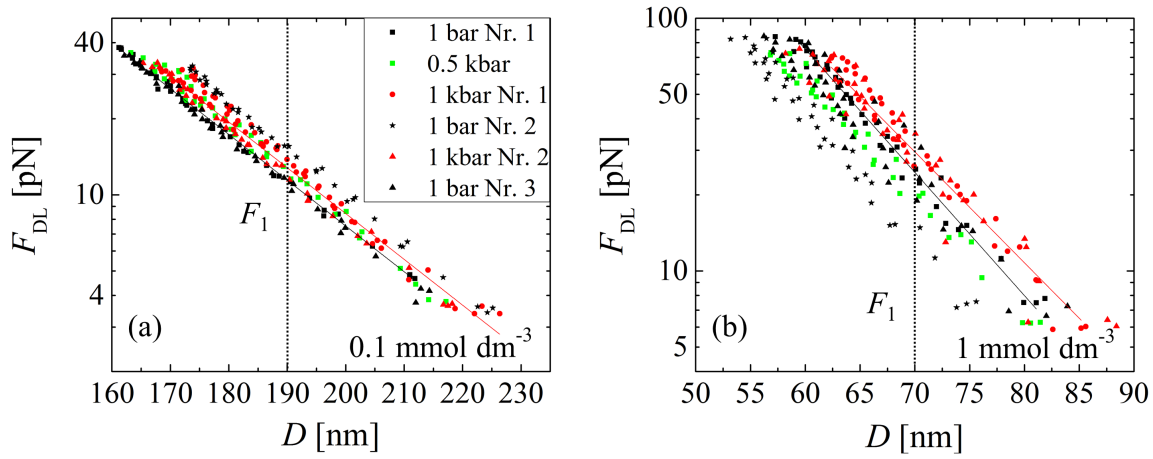

Figure 6.3: Semi-logarithmic plot of force curves recorded at hydrostatic pressures from 1 bar to 1 kbar at salt concentrations of 0.1 mmol dm^{-3} (a) and 1 mmol dm^{-3} (b). For all force curves at the same salt concentration the same bead was used. The radii of the two beads were (a) $R = (4.0 \pm 0.5)\,\mu$m and (b) $R = (3.6 \pm 0.5)\,\mu$m. $T = (21 \pm 1)\,^\circ$C. The experimental procedure was to first measure at a pressure of 1 bar (black squares), then 0.5 kbar (green squares), 1 kbar (red circles), again 1 bar (black stars), 1 kbar (red triangles) and finally 1 bar (black triangles). At each pressure step, at least three force curves were recorded. For example, the 40 black squares display one force curve composed of 20 data points and two force curves composed of 10 data points each. Error bars were not plotted for better visibility. However, errors of single data points were considered by the fitting algorithm. Solid lines are exemplary results of fits of the first force curve at 1 bar (black) and 1 kbar (red) with equation (6.1). Dotted lines mark the positions at which F_1 was determined (equation (6.17)).

the outlier for 0.1 mmol dm^{-3}, here the force seemed to decrease in the 0.5 kbar (green squares) and the second 1 bar measurement (black stars), furthermore suggesting that the large change of the force was not systematic but random.

A possible explanation for the outliers is a variation of bead orientation between measurements. Surface charge inhomogeneity was ascertained in the case of polystyrene beads [FV02] and hypothesized for silica beads [Che+09]. A variation of the surface charge density σ_s with the orientation of the bead would affect the measured F_0 (equations (6.1) and (6.5)) while not affecting the measured λ_D, since λ_D only depends on properties of the liquid (equation (6.3)). Furthermore, an inhomogeneity of the surface roughness would also affect the measured F_0 (see part 6.0.2). If the bead's orientation relative to the wall was fixed e.g. if the bead were glued to a cantilever, as in the case of

the colloidal probe technique [But91b; DSP91], the inhomogeneities would not affect the reproducibility of measured force curves. If the bead were free to rotate, as in the case e.g. in total internal reflection microscopy experiments [PLL87], the random rotation of the bead and thus constantly changing orientation would contribute to the measured noise. In the case of an optically trapped bead however, asymmetries in the bead's shape or optical density cause a preferred orientation of the bead relative to the trapping beam. It was for example observed that ellipsoidal particles, when trapped, locked their long axis in direction of beam propagation [MLP12; Mih+12]. Scanning electron microscopy images of the beads revealed asymmetries in the shape of the beads in the form of micrometer-sized features (see part 2.3). These asymmetries could cause the orientation of a bead to be locked during trapping, which would explain the overlap of consecutively measured force curves. However, when changing the pressure between measurements, the trapping laser was blocked for approximately 5 min and the bead sedimented to the lower wall of the capillary. Thus, the bead could rotate during that time, possibly causing a changed orientation when again being trapped by the trapping beam.

It was necessary to allow the bead to sediment to the lower capillary wall, since a change in the pressure caused the flexible high-pressure hose to expand (pressurization) or contract (pressure relaxation), which caused a lateral shift of the high-pressure cell. Trapping the bead at the upper capillary wall while changing the pressure could have led to the bead escaping the trapping beam due to the shift of the high-pressure cell, subsequently causing the bead to sediment out of focus and possibly get lost. Thus, in order to ensure that the same bead was used to record all force curves at a given salt concentration, it was not possible to keep the bead trapped and locked in its orientation while changing the pressure.

An alternative explanation to the random force changes could be dirt particles that entered the trapping beam. If located underneath the bead, dirt particles could influence the radiation pressure exerted on the bead by the trapping beam or the intensity of the interference signal. If located between bead and wall, dirt particles could furthermore have influenced the surface forces between bead and wall. However, the reflection interference signal is highly sensitive to dirt and would have noticeably been disturbed. This was not the case for any single measurement presented in this work. Dirt particles are thus excluded as a possible cause of the observed force changes.

6.2.1 Quantitative Comparison of the Force Magnitude at Different Pressures

In order to quantitatively compare the magnitude of the measured force between measurements, I compared the force at a fixed distance. For a given force curve fitted with equation (6.1) with fit value λ_D and F_0 the force F_1 at a fixed distance D_1 is determined by

$$F_1(D_1) = F_0 \exp(-\frac{D_1}{\lambda_D}) \,. \tag{6.17}$$

The distance ranges over which the force curves were recorded were approximately 160 nm to 230 nm and 55 nm to 90 nm for 0.1 mmol dm^{-3} and 1 mmol dm^{-3}, respectively (fig. 6.3). For a value of D_1 within the range of the experimental data, equation (6.17) is an interpolation. Since the fit curves were determined to fit the measured data best, an interpolated value of F_1 corresponds well to the recorded data. For a value of D_1 that exceeds the range, equation (6.17) is an extrapolation. For example $F_1(D_1 = 0) = F_0$, i.e. the fit value F_0 corresponds to an extrapolation to zero distance. Figuratively speaking, trying to determine F_0 by curve fitting data that was recorded far from the wall is like trying to press the power button on a distant computer using a long stick. For this reason the uncertainty of F_0 also depends on the error $\Delta\lambda_D$. The assumption that F_1 is exact at the left limit D_L of the range of a force curve together with the inversion of equation (6.17) allows the estimation of the relative error of the fit value F_0

$$\frac{\Delta F_0}{F_0} = \frac{1}{2}\left|\left(\exp(\frac{D_L}{\lambda_D - \Delta\lambda_D}) - \exp(\frac{D_L}{\lambda_D + \Delta\lambda_D})\right)\exp(-\frac{D_L}{\lambda_D})\right| \,. \tag{6.18}$$

For $D_L = 160\,\text{nm}$, $\lambda_D = (23 \pm 1)\,\text{nm}$ and $D_L = 55\,\text{nm}$, $\lambda_D = (9 \pm 1)\,\text{nm}$ we get $\Delta F_0/F_0 = 31\,\%$ and $\Delta F_0/F_0 = 80\,\%$, respectively. In order to avoid this imprecision of the fit values F_0, instead of directly comparing F_0 for different force curves, values of $F_1(D_1)$ were compared, where D_1 was within the range the measured force curve. The center of the range was chosen as the reference distance, i.e. $D_1 = 190\,\text{nm}$ and $D_1 = 70\,\text{nm}$ for all force curves for 0.1 mmol dm^{-3} and 1 mmol dm^{-3}, respectively (dotted lines in fig. 6.3). In figure 6.4 the displayed values of F_1 are averages for consecutively measured force curves and the error bars are the corresponding standard deviation, showing an average precision of the measured force magnitude of 3 % and 15 % for experiments at a salt con-

centration of 0.1 mmol dm^{-3} and 1 mmol dm^{-3}, respectively. The relative errors of F_1 are at least 5 times smaller than the estimated relative errors of the fit value F_0, confirming the expectation that F_1 is a more precise measure of the force at a given distance than F_0.

From the known pressure effect of the dielectric constant of water ϵ, the expected increase of F_0 and λ_D with increasing pressure was calculated (see part 6.0.1). The expected change between two values of F_1 for two different pressures p_1 and p_2 is given by

$$F_1(p_2) = F_1(p_1)\frac{F_0(p_2)}{F_0(p_1)}\exp\left(-\frac{D_1}{\lambda_D(p_2)} + \frac{D_1}{\lambda_D(p_1)}\right). \tag{6.19}$$

Using equations (6.7) for λ_D and (6.10) for F_0 with constant charge boundary condition results in

$$F_1^{CC}(p_2) = F_1(p_1)\sqrt{\frac{\epsilon(p_1)}{\epsilon(p_2)}}\exp\left(-\frac{D_1}{\lambda_D(p_2)}\left(1 - \sqrt{\frac{\epsilon(p_2)}{\epsilon(p_1)}}\right)\right). \tag{6.20}$$

The measured values $F_1(p)$ at different p can now be compared to each other by calculating what the expected value F_1^{CC} would be at a pressure of 1 bar

$$F_1^{CC} = F_1(p)\sqrt{\frac{\epsilon(p)}{\epsilon(1\,\text{bar})}}\exp\left(+\frac{D_1}{\lambda_D(p)}\left(1 - \sqrt{\frac{\epsilon(p)}{\epsilon(1\,\text{bar})}}\right)\right). \tag{6.21}$$

Values of F_1 (black crosses) and F_1^{CC} (blue circles) at $p = 1$ bar overlap (fig. 6.4), as is expected from equation (6.21). For both salt concentrations at $p = 0.5$ kbar and $p = 1$ kbar, $F_1^{CC}/F_1 \approx 0.92$ and $F_1^{CC}/F_1 \approx 0.85$, respectively. This large correction is mostly due to accounting for the pressure effect of λ_D which enters equation (6.21) exponentially. The correction of F_0 accounts for approximately 1 % to 2 % of the difference.

After correcting for the expected pressure effects, it can be seen that for the experiment with $c_0 = 0.1$ mmol dm^{-3} the values of F_1^{CC} recorded at the first and last 1 bar, the 0.5 kbar and the first 1 kbar measurement match within their error (fig. 6.4(a)). The value of F_1^{CC} for the second 1 kbar measurement is slightly lower by approximately 10 % compared to the former values. The F_1^{CC} value at the second 1 bar measurement deviates strongly by being at least 33 % higher than any of the other values of F_1^{CC}. As mentioned above, this

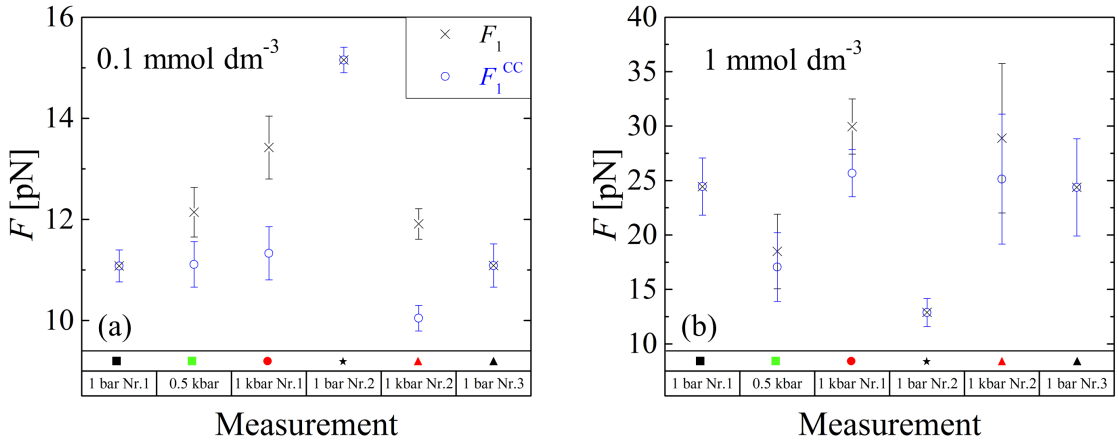

Figure 6.4: Magnitudes of the force F_1 determined from the force curves (fig. 6.3) at different hydrostatic pressures. Values of F_1 were determined for each force curve using equation (6.17) with $D_1 = 190\,\text{nm}$ and $D_1 = 70\,\text{nm}$ for $0.1\,\text{mmol}\,\text{dm}^{-3}$ and $1\,\text{mmol}\,\text{dm}^{-3}$, respectively. Mean values for consecutive force curves at same hydrostatic pressure are plotted (black crosses). F_1^{CC} are force magnitudes corrected for known pressure effects by equation (6.21) (blue circles). Errors are the determined standard deviations. For better orientation, the symbols of the corresponding force curves were displayed at the bottom.

difference can neither be explained by an effect of pressure, nor by a history effect, since the second as well as the third measurement at 1 bar were directly after a measurement at 1 kbar. It is much rather likely that the bead had the same orientation (orientation 1) in all cases except for the second 1 bar measurement (orientation 2). Maybe in the case of the second 1 kbar measurement the bead assumed a third orientation, although the difference to orientation 1 seems rather small. Since the bead assumed orientation 1 at least four times more often than orientation 2, orientation 1 seems to be the most probable orientation.

The experiment with $c_0 = 1\,\text{mmol}\,\text{dm}^{-3}$ shows qualitatively the same behavior as the one with $0.1\,\text{mmol}\,\text{dm}^{-3}$ (fig. 6.4 (b)). The values of F_1^{CC} match within their error for the first and last 1 bar and both 1 kbar measurements. The value of F_1^{CC} is by approximately 36 % lower for the 0.5 kbar force curves compared to the former values. For the second 1 bar measurement F_1^{CC} is approximately half of what was measured for the other two 1 bar measurements. These two deviants as well suggest a random error that could be explained by a varying orientation of the bead.

However, the majority of the performed measurements (at least 2 out of 3) agrees with the hypothesis that the effect of pressure on the electrostatic double-layer force originates solely from the effect of pressure on the dielectric constant ϵ. None of the measured F_1^{CC} values differ by one order of magnitude from each other. Since F_1^{CC} was corrected for pressure effects of λ_D, it can be concluded that the actual amplitude F_0 of the double-layer force as well did not decrease by one order of magnitude. Such a strong decrease was expected, based on the decrease of the ζ-potential with pressure that was reported by others (see [RA06; AOS11] and part 6.0.1). It is thus evident, that no such pressure effect of the ζ-potential occurred.

Nevertheless, in order to quantify to what extent the magnitude of the electrostatic double-layer force remained constant during the entire experiment, it was assumed that all values of F_1^{CC} were independent of p and their variation was purely statistical. By determining the overall mean μ and standard deviation σ of values F_1^{CC} we get $\sigma/\mu = 0.14$ and $\sigma/\mu = 0.28$ for the experiment with salt concentration 0.1 mmol dm^{-3} and 1 mmol dm^{-3}, respectively. Thus, after correction for known pressure effects, the force amplitude F_0 was constant within 14 % and 28 % for the experiment with 0.1 mmol dm^{-3} and 1 mmol dm^{-3} salt concentration, respectively. This affirms the finding, that the pressure effect of the ζ-potential is negligible.

It is important to note that the constant charge boundary condition was assumed for deriving F_1^{CC}. However, another possibility is that ψ_0 remained constant during pressurization and σ_s varied (see part 6.0.1). Assuming the constant potential boundary condition (equation (6.11)) the corrected values F_1^{CP} are determined by

$$F_1^{CP} = F_1(p)\sqrt{\frac{\epsilon(p = 1\,\mathrm{bar})}{\epsilon(p)}}\exp\left(+\frac{D_1}{\lambda_D(p)}\left(1 - \sqrt{\frac{\epsilon(p)}{\epsilon(p = 1\,\mathrm{bar})}}\right)\right). \tag{6.22}$$

The difference between the corrections due to the two different boundary conditions is $F_1^{CC}/F_1^{CP} = \epsilon(p)/\epsilon(p = 1\,\mathrm{bar})$, i.e. for $p = 1$ kbar, F_1^{CC} is 4.6 % larger than F_1^{CP}. This difference is of the order of the errors of single F_1 values. Thus, within the error of the experiment it was not possible to decide, which boundary condition is correct for the investigated system.

6.3 Summary

It was demonstrated that force curves were recorded with a sub-nanometer resolution in distance. The electrostatic double-layer force was successfully measured at hydrostatic pressures up to 1 kbar. The Debye length was found constant on the investigated pressure range within approximately 1 nm, which corresponds to the experimental precision of determining the Debye length. By careful evaluation of the force magnitude, the measured pressure effects could be explained by the pressure induced increase of the dielectric constant of water. Based on the here presented results, a decrease of the ζ-potential with increasing pressure as reported by [RA06] can be excluded. The results further prove that no significant artifact due to the pressurization occurred and the here presented method is a reliable tool for the measurement of surface forces at high hydrostatic pressure.

Changes in the measured forces that were not correlated with pressure could best be explained by inhomogeneity of the surface charge of the beads. To the best of my knowledge, this is the first report of an effect of inhomogeneities of the surface charge of colloidal beads on measured surface forces.

7 Thermal Motion at High Hydrostatic Pressure

7.1 Motivation

In the previous chapters of this thesis the electrostatic double-layer force on the bead in equilibrium was determined by a *hydrodynamic method*, i.e. by analysis of the hydrodynamic drag on the bead moving towards the wall. The resulting force curves are presented in chapter 6. For determining these force curves, the thermal motion of the bead close to the wall had to be accounted for (as discussed in chapter 5) in order to determine the equilibrium position D_{eq}, where the force pushing the bead against the wall was in equilibrium with the electrostatic double-layer force repelling the bead from the wall. The thermal motion of the bead was essentially treated as unwanted noise and its effect on the beads position was removed by averaging. However, the thermal motion holds a variety of information about the system under investigation and has the potential to extend the range of interactions accessible with the here presented instrument.

Techniques such as total internal reflection microscopy [PLL87] or reflection interference contrast microscopy [RS92] are available that allow to resolve the thermal motion of a colloidal particle with nanometer resolution at ambient pressure. It was reported, that with total internal reflection microscopy forces down to 0.01 pN could be investigated [Pri99]. The investigation of the thermal motion of a colloidal bead allowed the study of multiple interactions [Pri99], like the electrostatic double-layer force [AP87], hydrodynamic interactions [BS90], van der Waals interactions [BP99] or critical Casimir forces [Her+08].

However, the possibilities to investigate the thermal motion of colloidal particles at high hydrostatic pressure are extremely limited [MDT06]. The thermal motion of a colloidal sphere close to a wall at hydrostatic pressures up to 250 bar has been studied before by

Mukai *et al.* [MDT06]. Here the lateral diffusion coefficient was measured by tracking the position of the sphere using light microscopy with an optical resolution of 2 μm. Bowman *et al.* optically trapped a colloidal glass bead in bulk water inside a diamond anvil cell [Bow+13a; Bow+13b]. They tracked the bead's lateral thermal motion by high-speed (1 ms time resolution) video particle tracking and determined the bead's diffusion coefficient in order to derive the viscosity of water at up to 13 kbar hydrostatic pressure. Thus, so far the thermal motion of colloidal particles at high hydrostatic pressure could be tracked at best with micrometer resolution.

In chapter 6 it was shown that the investigation of surface forces at pressures up to 1 kbar with sub-nanometer resolution is possible. However, since any noise was averaged out in the previous evaluation, it remains unclear whether the measured noise is actually the thermal motion of the bead and how well the thermal motion is resolved.

In this chapter force curves will be determined by a *thermal method*, i.e. by analysis of the thermal motion of the bead. It will be shown that the measured noise signal is mainly due to the thermal motion of the bead with a minor instrument noise contribution. At first the noise signal will be evaluated for measurements at ambient pressure in order to independently derive force curves of the electrostatic double-layer force F_{DL} between bead and wall that will be compared to the force curves determined in chapter 6. Finally the thermal motion of the bead will be analyzed at 1 kbar hydrostatic pressure. It will be demonstrated that the thermal motion could be measured at high pressure just as well as at ambient pressure.

7.2 Determination of the Electrostatic Double-Layer Force by Analysis of the Thermal Motion

The probability density $p(D)$ of the bead's position depends on the potential $V(D)$ between bead and wall (equation (5.2))

$$p(D) = A \exp\left(-\frac{V(D)}{k_{\mathrm{B}}T}\right). \tag{7.1}$$

In order to deduce a force curve, it is possible to directly determine the potential $V(D)$ from analysis of $p(D)$ and deduce the total force on the bead F_{total} by derivation (equation (5.3))

$$-V'(D) \equiv -\frac{\mathrm{d}V}{\mathrm{d}D}(D) = F_{\text{total}}(D) \,. \tag{7.2}$$

However, since $F_{\text{total}} = F_{\text{DL}} + F_{\text{bead}}$, in order to determine the absolute values of F_{DL}, a calibration of the force driving the bead against the wall F_{bead} would be needed.

The aim was to obtain force values with the thermal method F_{tm} that are independent of force values determined with the hydrodynamic method F_{hd} (see equation (3.4)). This was achieved by in the following way. The harmonic approximation (equation (5.16))

$$p(D) = \tilde{A} \exp\left(-\frac{1}{2} \frac{V''\left(D_{\text{eq}}\right)}{k_{\text{B}}T} \left(D - D_{\text{eq}}\right)^2 \right) \tag{7.3}$$

was used. Hence, the probability density was a Gaussian distribution. The standard deviation σ_{tm} of the probability density $p(D)$ is related to the second derivative of the potential $V(D)$ at the position D_{eq} (equation (5.18))

$$V''\left(D_{\text{eq}}\right) = \frac{k_{\text{B}}T}{\sigma_{\text{tm}}^2} \,. \tag{7.4}$$

It was shown above that (equation (5.7))

$$V''(D) = F_{\text{DL}}(D)/\lambda_{\text{D}} \,, \tag{7.5}$$

which yields

$$F_{\text{DL}}\left(D_{\text{eq}}\right) = \lambda_{\text{D}} \frac{k_{\text{B}}T}{\sigma_{\text{tm}}^2} = F_{\text{tm}}\left(D_{\text{eq}}\right) \,. \tag{7.6}$$

Thus, the thermal method for determining the electrostatic double layer force is as follows:

1. The standard deviation of the probability density σ_{tm} is determined for different equilibrium positions D_{eq}.

2. From the determined standard deviations, the values of $V''\left(D_{\text{eq}}\right)$ are determined (equation (7.4)), overall yielding the curve $V''(D)$

3. $V''(D)$ is an exponential function with the same decay constant as $F_{\mathrm{DL}}(D)$ (equation (7.5)), allowing for the determination of λ_{D}.

4. Multiplication of $V''(D)$ by λ_{D} yields the force curve $F_{\mathrm{tm}}(D) = F_{\mathrm{DL}}(D)$.

7.2.1 Influence of Instrument Noise

The standard deviation σ_{tm} was assumed to depend solely on the thermal motion of the bead. However, it was discussed above that instrument noise increases the standard deviation σ_{m} of the measured probability density $p(D)$ (equation (5.39)), i.e.

$$\sigma_{\mathrm{m}}^2 = \sigma_{\mathrm{tm}}^2 + \sigma_{\mathrm{in}}^2 \,. \tag{7.7}$$

Here σ_{in} is the standard deviation of the D measurement corresponding to instrument noise. For the determined force values with the thermal method this means

$$F_{\mathrm{tm}}\Big(D_{\mathrm{eq}}\Big) = \lambda_{\mathrm{D}} \frac{k_{\mathrm{B}}T}{\sigma_{\mathrm{m}}^2} \tag{7.8}$$

$$= \lambda_{\mathrm{D}} \frac{k_{\mathrm{B}}T}{\sigma_{\mathrm{tm}}^2 + \sigma_{\mathrm{in}}^2} \,. \tag{7.9}$$

Hence, in the presence of instrument noise, the determined force is an underestimation of the electrostatic double-layer force

$$F_{\mathrm{tm}}\Big(D_{\mathrm{eq}}\Big) \leq F_{\mathrm{DL}}\Big(D_{\mathrm{eq}}\Big) \,. \tag{7.10}$$

Equation (7.6) is the special case of relation (7.10) for negligible instrument noise, i.e. $\sigma_{\mathrm{in}} << \sigma_{\mathrm{tm}}$. It is the only case where F_{tm} is equal to the actual magnitude of the double-layer force.

As the signal to noise ratio $\sigma_{\mathrm{tm}}/\sigma_{\mathrm{in}}$ decreases, so does the ratio $F_{\mathrm{tm}}\Big(D_{\mathrm{eq}}\Big)/F_{\mathrm{DL}}\Big(D_{\mathrm{eq}}\Big)$. Since $\sigma_{\mathrm{tm}}^2 \propto 1/F_{\mathrm{DL}}(D)$, generically the signal to noise ratio $\sigma_{\mathrm{tm}}/\sigma_{\mathrm{in}}$ decreases with decreasing distance D, resulting in a flattening of the measured force curve $F_{\mathrm{tm}}(D)$ due to instrument noise. Therefore, in the presence of instrument noise the decay constant $\lambda_{\mathrm{D}}^{\mathrm{tm}}$ of the force curve $F_{\mathrm{tm}}(D)$ is expected to be larger than the Debye length

$$\lambda_{\mathrm{D}}^{\mathrm{tm}} \geq \lambda_{\mathrm{D}} \,. \tag{7.11}$$

7.3 Measurement of the Electrostatic Double-Layer Force by Analysis of Thermal Motion

The thermal motion of the bead around its equilibrium position was analyzed for the same data that was presented in chapter 6, yielding multiple values for standard deviations σ_m corresponding to positions D_{eq} (see part 5.2 Data Analysis). Exemplary, the first experiment recorded at $p = 1\,\text{bar}$ was plotted (fig. 7.1 (a)). Due to the increasing slope of the double-layer force, the measured σ_m decreased with decreasing bead-wall distance. Application of equation (7.4) yielded the curvature of the potential $V''(D)$ (fig. 7.1 (b)). Fitting of $V''(D)$ with an exponential function yielded λ_D^{tm}.

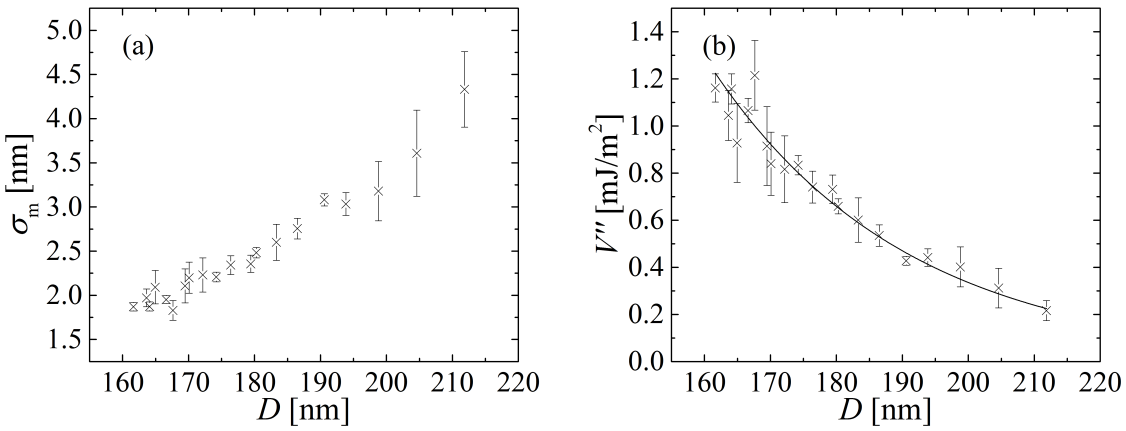

Figure 7.1: Evaluation of the bead's thermal motion at $p = 1\,\text{bar}$ and $c_0 = 0.1\,\text{mmol}\,\text{dm}^{-3}$ for powers P of the trapping beam between 29 mW and 142 mW. (a) Standard deviation σ_m of the measured probability density $p(D)$ at different equilibrium positions D_{eq}. (b) Corresponding curvature of the potential $V''\left(D_{eq}\right)$ calculated using equation (7.4) with $T = (294 \pm 1)\,\text{K}$. The underlying single measurements are the same as for fig. 6.2 at $c_0 = 0.1\,\text{mmol}\,\text{dm}^{-3}$. Thus, the errors of D_{eq} are the same as for fig. 6.2 at $c_0 = 0.1\,\text{mmol}\,\text{dm}^{-3}$ and were not plotted. The errors of σ_m and $V''\left(D_{eq}\right)$ are a measure of the variation of σ_m for varying sampling times τ form 0.5 s to 2 s. The curve $V''(D)$ was fitted with an exponential function (black line), yielding a decay constant of $\lambda_D^{tm} = (29.6 \pm 1.1)\,\text{nm}$.

Although the curve in fig. 7.1 (b) was determined from the same data as the force curve for $c_0 = 0.1\,\text{mmol}\,\text{dm}^{-3}$ in fig. 6.2, the determined decay constants differ from each other. The thermal method gave $\lambda_D^{tm} = (29.6 \pm 1.1)\,\text{nm}$, which is larger than the decay constant $\lambda_D^{hd} = (24.0 \pm 0.3)\,\text{nm}$ determined with the hydrodynamic method for the same data. On

average the decay constants determined with the thermal method were

$$\overline{\lambda_D^{tm}} = (26.5 \pm 2.9)\,\mathrm{nm} \tag{7.12}$$

and

$$\overline{\lambda_D^{tm}} = (10.3 \pm 1.1)\,\mathrm{nm}\,, \tag{7.13}$$

at salt concentrations of $c_0 = 0.1\,\mathrm{mmol\,dm^{-3}}$ and $1\,\mathrm{mmol\,dm^{-3}}$, respectively. Thus, on average λ_D^{tm} was approximately 15 % larger than λ_D^{hd} (see table 6.1). This difference between the thermal and the hydrodynamic method was expected due to the above discussed vulnerability of the thermal method to instrument noise (equation (7.11)).

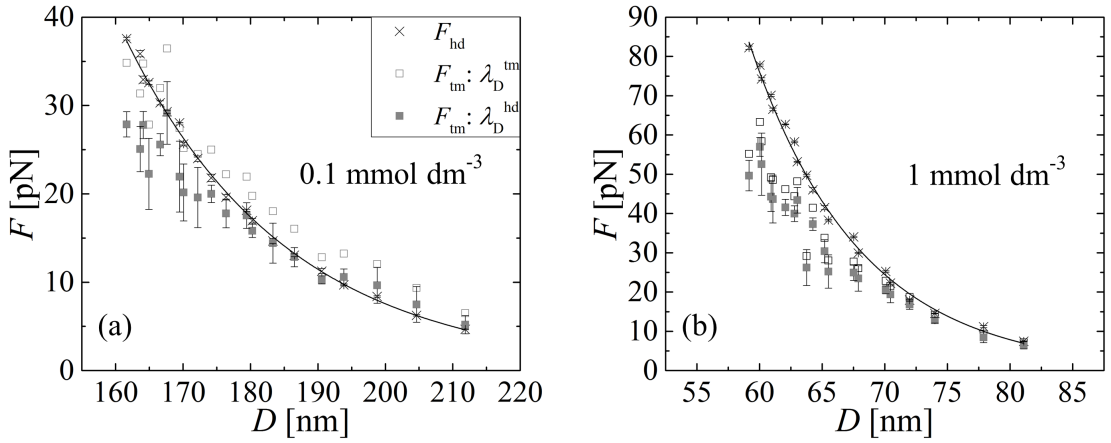

Figure 7.2: Comparison of thermal and hydrodynamic method. Data was recorded at $p = 1\,\mathrm{bar}$, $T = (21 \pm 1)\,°\mathrm{C}$ and $c_0 = 0.1\,\mathrm{mmol\,dm^{-3}}$ (a) and $c_0 = 1\,\mathrm{mmol\,dm^{-3}}$ (b). Force curves were determined by the thermal method using equation (7.8) with λ_D^{tm} (denoted as $F_{tm} : \lambda_D^{tm}$, open squares) and λ_D^{hd} (denoted as $F_{tm} : \lambda_D^{hd}$, gray squares). For comparison the force curves determined with the hydrodynamic method were plotted (crosses) with corresponding fit of equation (6.4). For (a): $\lambda_D^{tm} = (29.6 \pm 1.1)\,\mathrm{nm}$ and $\lambda_D^{hd} = (24.0 \pm 0.3)\,\mathrm{nm}$ and for (b): $\lambda_D^{tm} = (10.3 \pm 0.4)\,\mathrm{nm}$ and $\lambda_D^{hd} = (8.8 \pm 0.2)\,\mathrm{nm}$. The errors of the force values were approximately the same for $F_{tm} : \lambda_D^{tm}$ and $F_{tm} : \lambda_D^{hd}$. For better readability these errors were just plotted for $F_{tm} : \lambda_D^{hd}$. Since all force curves share the same D_{eq} values, the errors of D_{eq} were not plotted. The errors of D_{eq} are the same as in fig. 6.2.

The force curves $F_{tm}(D)$ were calculated in two ways: by multiplication of the measured $V''(D) = k_B T/\sigma_m^2$ by the decay constant λ_D^{tm} determined with the thermal method (fig.

7.2 empty squares) and by the decay constant λ_D^{hd} determined with the hydrodynamic method (filled squares). For comparison the force curves determined with the hydrodynamic method $F_{hd}(D)$ were plotted (crosses) with corresponding fit of equation (6.4) (solid line).

In order to compare the force curves determined with the two methods, the average relative difference of the force magnitude was calculated

$$\overline{\Delta F} = \frac{1}{N} \sum_{i=1}^{N} \left| \frac{F_{tm}(D_i) - F_{hd}(D_i)}{F_{hd}(D_i)} \right| . \tag{7.14}$$

Here N is the number of data points that compose a force curve. For a salt concentration of $c_0 = 0.1\,\mathrm{mmol\,dm^{-3}}$ and F_{tm} calculated with λ_D^{tm}:

$$\overline{\Delta F} = 18.5\,\% , \tag{7.15}$$

and for F_{tm} calculated with λ_D^{hd}:

$$\overline{\Delta F} = 13.8\,\% . \tag{7.16}$$

However, for $c_0 = 1\,\mathrm{mmol\,dm^{-3}}$ and F_{tm} calculated with λ_D^{tm}:

$$\overline{\Delta F} = 17.9\,\% , \tag{7.17}$$

and for F_{tm} calculated with λ_D^{hd}:

$$\overline{\Delta F} = 25.7\,\% . \tag{7.18}$$

In all cases, the agreement between force curves was comparable to the estimated inaccuracy of determining F_{hd}, i.e. 22 % and 25 % for $0.1\,\mathrm{mmol\,dm^{-3}}$ and $1\,\mathrm{mmol\,dm^{-3}}$, respectively (see part 3.2.1). In particular, force values F_{tm} calculated with λ_D^{tm} agree with the force values F_{hd}, demonstrating that the results obtained with the thermal method are in agreement with those obtained with the hydrodynamic method. However, since due to instrument noise λ_D^{hd} is argued to be less accurate than λ_D^{tm}, for further evaluation λ_D^{hd} was used for calculation of the force F_{tm}.

7.3.1 Accounting for Instrument Noise

By applying equation (7.7), instrument noise can be corrected for by subtraction of the corresponding variance σ^2_{in} from the measured variance σ^2_{m}

$$\sigma^2_{\mathrm{tm}} = \sigma^2_{\mathrm{m}} - \sigma^2_{\mathrm{in}} \,. \tag{7.19}$$

Insertion into equation (7.6) yields the corrected force values

$$F^{\mathrm{c}}_{\mathrm{tm}}\left(D_{\mathrm{eq}}\right) = \lambda_{\mathrm{D}} \frac{k_{\mathrm{B}}T}{\sigma^2_{\mathrm{m}} - \sigma^2_{\mathrm{in}}} \,. \tag{7.20}$$

As discussed above (equation (5.40)), the variance of the instrument noise is the sum of variances of the known laser noise σ^2_{ln} and other noise contributions σ^2_{on}

$$\sigma^2_{\mathrm{in}} = \sigma^2_{\mathrm{ln}} + \sigma^2_{\mathrm{on}} \,. \tag{7.21}$$

Using the finding $\sigma^{\mathrm{I}}_{\mathrm{ln}}/\overline{I_0} = 0.8\,\%$ (fig. 2.6) together with equation (5.36), which relates the standard deviation of the intensity $\sigma^{\mathrm{I}}_{\mathrm{ln}}$ to the standard deviation of the position σ_{ln}, the standard deviation of the laser noise σ_{ln} was calculated for every data point, yielding values between 0.2 nm and 0.5 nm. The standard deviation due to other noise sources σ_{on} was not known.

$\sigma^{\mathrm{I}}_{\mathrm{ln}}/\overline{I_0}$ [%]	σ_{on} [nm]	$\lambda^{\mathrm{tm}}_{\mathrm{D}}$ (0.1 mmol dm^{-3}) [nm]	$\lambda^{\mathrm{tm}}_{\mathrm{D}}$ (1 mmol dm^{-3}) [nm]
0	0	28.6 ± 2.7	10.0 ± 0.5
0.8	0	26.5 ± 2.5	9.6 ± 0.5
1.6	0	20.1 ± 2.0	8.1 ± 0.5
0.8	0.3	25.9 ± 2.5	8.9 ± 0.5
0.8	0.5	24.8 ± 2.5	7.4 ± 0.5
0.8	1.0	23.1 ± 2.4	4.3 ± 0.4

Table 7.1: Effect of instrument noise correction on $\lambda^{\mathrm{tm}}_{\mathrm{D}}$. Force curves were calculated using equations (7.20) and (5.40) for different standard deviations of the intensity noise of the interference beam $\sigma^{\mathrm{I}}_{\mathrm{ln}}/\overline{I_0}$ and other noise sources σ_{on}. The resulting force curves were fitted with equation (6.4) in order to determine $\lambda^{\mathrm{tm}}_{\mathrm{D}}$.

In order to examine the effect of instrument noise correction on the thermal method, the force values $F_{\mathrm{tm}} : \lambda^{\mathrm{hd}}_{\mathrm{D}}$ in fig. 7.2 were recalculated using equation (7.20) for different values of $\sigma^{\mathrm{I}}_{\mathrm{ln}}/\overline{I_0}$ and σ_{on}. The resulting force curves were fitted by the exponential function

(6.4) in order to determine the decay constants λ_D^{tm} (table 7.1). In general it was found that the larger the value of the subtracted variance, the smaller the corresponding decay constant. This is in agreement with the finding from total internal reflection microscopy experiments that instrument noise obscures the determination of the Debye length by increasing the measured decay constant [NAB13; Sho+00].

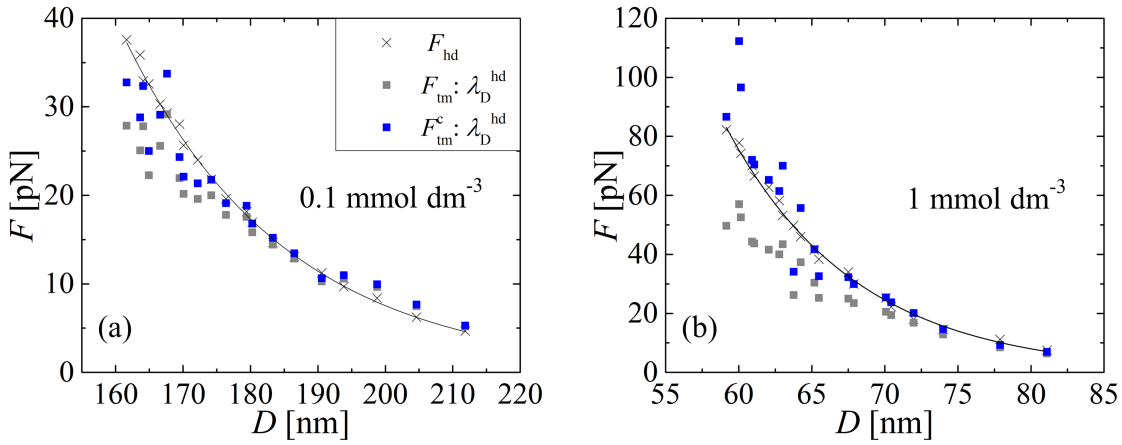

Figure 7.3: Instrument noise correction. Data was recorded at $p = 1\,\text{bar}$, $T = (21 \pm 1)\,°\text{C}$ and $c_0 = 0.1\,\text{mmol}\,\text{dm}^{-3}$ (a) and $c_0 = 1\,\text{mmol}\,\text{dm}^{-3}$ (b). Force curves $F_{tm} : \lambda_D^{hd}$ were determined with the thermal method using equation (7.8) with λ_D^{hd} (gray squares). Instrument noise corrected force curves $F_{tm}^c : \lambda_D^{hd}$ were calculated with equation (7.20) using $\sigma_{ln}^I/\overline{I_0} = 0.8\,\%$ and $\sigma_{on} = 0.5\,\text{nm}$ (blue squares). For comparison the force curves determined with the hydrodynamic method were plotted (crosses) with corresponding fit of equation (6.4) (black line). Error bars were not plotted for better visibility.

As mentioned above, it was determined that $\sigma_{ln}^I/\overline{I_0} = 0.8\,\%$ for the experiments presented in this thesis. Comparing the decay constants λ_D^{tm} in table 7.1 to the decay constants determined with the hydrodynamic method λ_D^{hd} (see fig. 7.2), σ_{on} is expected to be in a range from 0.3 nm to 0.5 nm. Values of σ_{on} that were outside this range led to significant discrepancies of λ_D^{hd} and λ_D^{tm}. This evaluation yields, that noise that could not be accounted for as laser noise was on the sub-nanometer scale. Thus, the overall RMS instrument noise was approximately

$$\sigma_{in} = \sqrt{\sigma_{ln}^2 + \sigma_{on}^2} \approx 1\,\text{nm}\,. \tag{7.22}$$

As an example, $F_{tm}^c(D)$ was calculated for $\sigma_{ln}^I/\overline{I_0} = 0.8\,\%$ and $\sigma_{on} = 0.5\,\text{nm}$ (fig. 7.3 blue

squares). Using equation (7.14) the average difference of the force magnitudes of $F^{c}_{tm}(D)$ and $F_{hd}(D)$ was on average

$$\overline{\Delta F} = 10.1\,\% \tag{7.23}$$

and

$$\overline{\Delta F} = 12.3\,\% \tag{7.24}$$

for 0.1 mmol dm^{-3} and 1 mmol dm^{-3}, respectively. Hence, the instrument-noise-corrected force curves were in best agreement with the force curves determined with the hydrodynamic method.

7.4 High Hydrostatic Pressure Experiments

The thermal method of force measurement was applied at a hydrostatic pressure of $p = 1\,\text{kbar}$ (fig. 7.4). In order to account for instrument noise, $\sigma^{I}_{ln}/\overline{I_0} = 0.8\,\%$ and $\sigma_{on} = 0.5\,\text{nm}$ were used to calculate $F^{c}_{tm}(D)$.

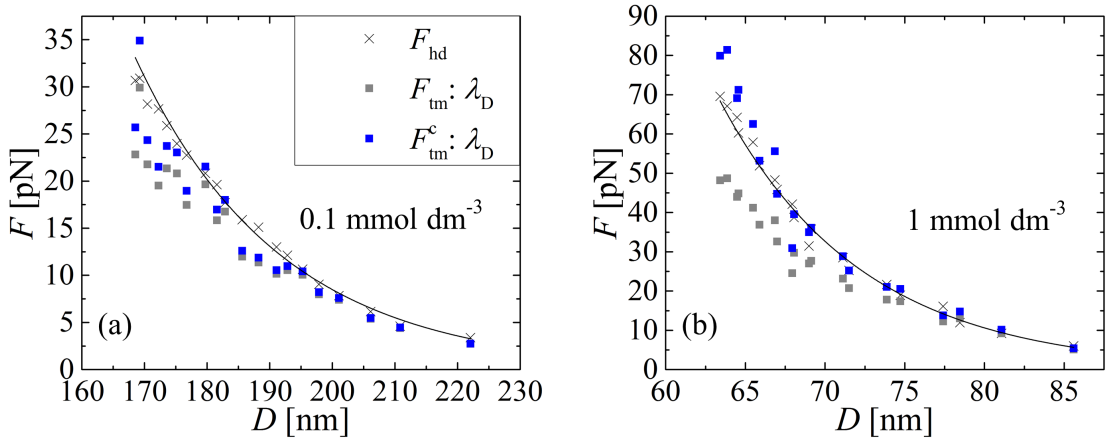

Figure 7.4: Thermal method at high pressure. Data was recorded at $p = 1\,\text{kbar}$, $T = (21 \pm 1)\,°\text{C}$ and $c_0 = 0.1\,\text{mmol dm}^{-3}$ (a) and $c_0 = 1\,\text{mmol dm}^{-3}$ (b). Force curves $F_{tm} : \lambda^{hd}_{D}$ were determined with the thermal method using equation (7.8) with λ^{hd}_{D} (gray squares). Instrument noise corrected force curves $F^{c}_{tm} : \lambda^{hd}_{D}$ were calculated with equation (7.20) using $\sigma^{I}_{ln}/\overline{I_0} = 0.8\,\%$ and $\sigma_{on} = 0.5\,\text{nm}$ (blue squares). For comparison, the force curves determined with the hydrodynamic method were plotted (crosses) with corresponding fit of equation (6.4). Error bars were not plotted for better visibility.

The difference of the force magnitudes of the uncorrected $F_{\mathrm{tm}}(D)$ and $F_{\mathrm{hd}}(D)$ was on average

$$\overline{\Delta F} = 15.5\,\% \tag{7.25}$$

and

$$\overline{\Delta F} = 21.8\,\% \tag{7.26}$$

for 0.1 mmol dm^{-3} and 1 mmol dm^{-3}, respectively. The difference of the force magnitudes of the instrument-noise-corrected $F^{\mathrm{c}}_{\mathrm{tm}}(D)$ and $F_{\mathrm{hd}}(D)$ was on average

$$\overline{\Delta F} = 11.6\,\% \tag{7.27}$$

and

$$\overline{\Delta F} = 10.1\,\% \tag{7.28}$$

for 0.1 mmol dm^{-3} and 1 mmol dm^{-3}, respectively. Thus, the force curves determined with the thermal method at high pressure showed the same agreement as with force curves determined with the hydrodynamic method the ones at ambient pressure. Since for instrument noise correction the parameters determined from ambient pressure experiments were used, it can be seen that there was no additional noise at high pressure compared to ambient pressure.

7.5 Summary

Force curves of the electrostatic double-layer force between the bead and the wall were determined by analysis of the thermal motion of the bead in equilibrium. These force curves were in agreement with the force curves determined by analysis of the hydrodynamic drag on the bead, which is evidence for the accuracy of both both the hydrodynamic and the thermal method for surface force measurement.

It was found that the thermal method is sensitive to instrument noise, unlike the hydrodynamic method. In particular, instrument noise was found to increase the determined decay lengths of the force curves. By comparison of force curves determined with the hydrodynamic and the thermal method it was found that the RMS instrument noise was of the order of approximately 1 nm, which is comparable to noise in other state of the art techniques like total internal reflection microscopy. Although this finding was de-

rived from a statistical treatment of the data, implications for the time-resolved thermal motion of a colloidal bead can be derived. At any given time the position of the bead is determined with nanometer precision.

The measurement of the thermal motion of the bead at pressure up to 1 kbar showed no difference to the measurement at ambient pressure. As in the case of ambient pressure, an RMS instrument noise of approximately 1 nm was found for the high pressure measurements. This means that with the here presented instrument the investigation of the thermal motion of a colloidal bead is possible with nanometer resolution at high hydrostatic pressure.

8 Concluding remarks and Outlook

With my work, I developed a scientific instrument that enables the investigation of surface forces at high hydrostatic pressure. Using this instrument, I measured surface forces at ambient pressure as well as at hydrostatic pressures up to 1 kbar, which is of the order of the highest hydrostatic pressure naturally present on the surface of earth. In particular, I could clarify the pressure dependence of the electrostatic double-layer force between glass surfaces in water. In general, a multitude of surface forces can now be investigated at high pressure, making a deeper insight into physics at extreme conditions possible.

The developed instrument is a combination of a long-working-distance optical trap with a reflection interference technique, based on a method published by Nadal *et al.* [Nad+01]. The performance of the developed instrument exceeds the performance of the previously published one in many ways.

- Force curves were recorded with sub-nanometer distance resolution and maximum exercisable forces of the order 0.1 nN, which is in both cases an improvement of approximately one order of magnitude compared to what was published before. The maximum exercisable force is of the same order as the largest optical forces reported for other optical traps [JZ08].
- By adjusting the geometry of the optical trap and providing computer-controlled adjustment of parameters of the trapping beam, the automated recording of force curves was implemented. The automation significantly reduced the duration of experiments, i.e. a force curve was recorded within minutes. This enabled a statistical treatment of the recorded force curves. In comparison, in the previous work a single force curve consisting of 12 data points was interpreted [Nad+01].
- The repeatability of the recorded force curves was demonstrated and the quantitative agreement of the measured Debye-lengths with values calculated from solution properties was verified.

- It was ascertained that solely optical forces were exerted by the trapping beam and no measurable thermal effects occurred.

Force curves were not recorded directly but were determined by analysis of the trajectory of the colloidal bead. I provided and verified simple methods for the analysis of the hydrodynamic drag on the bead and the thermal motion of the bead. In particular, I demonstrated that an analytical model for the hydrodynamic wall effect suggested by Butt and Kappl led to equivalent results as the exact numerical model. The use of the analytical model enabled the automation of the data analysis and thus increased the number of force curves that could be determined.

The instrument was used for surface force measurements inside an optical high-pressure cell at hydrostatic pressures of up to 1 kbar. By encapsulation of the sample solution and the glass beads into a rectangular glass capillary, the sample solution was separated from the pressure transmitting water. From the repeatability of force curves recorded at alternating pressure it can be concluded, that no irreversible pressure effects occurred. This signifies that the capillary capsule remained intact for the entire experimental procedure. Hence, my method of encapsulation is suitable for providing defined conditions for surface force measurements at high pressure. Furthermore, only a volume $< 1\,\mu$l of the sample dispersion is needed for high pressure experiments, which is multiple orders of magnitude smaller than the total pressurized volume (> 0.1 l).

The electrostatic double-layer force was studied at hydrostatic pressures from 1 bar to 1 kbar. The measured pressure effects could be traced back to the pressure effect of the dielectric constant of water. In particular, I can conclude that the zeta potential of an electric double-layer is not dependent on pressure, especially not as strongly as reported by others [RA06; AOS11]. Overall, the effect of pressure on the electrostatic double-layer force was minor. Therefore I conclude that colloidal stability, governed by the electrostatic double-layer force, is not affected by pressure. Furthermore, since the changes of the force curves due to pressure were minor and explainable, it is assured that the developed instrument works reliably at high hydrostatic pressure. Such reliability is the foundation of future high pressure research, especially on systems with possibly complex pressure effects.

The precision and reliability of the instrument allowed the observation of anisotropic effects of the interaction between the colloidal bead and the wall. During the investigation

of the electrostatic double-layer force, fluctuations of the force between approximately 33 % and 50 % occurred. These fluctuations could be explained with an inhomogeneity of both the shape of the beads and the surface charge distribution. While the inhomogeneity of the shape of the beads was evident from scanning electron microscopy images, charge inhomogeneity on the surface of glass beads has been only hypothesized [Che+09], not proven. The here obtained results are further evidence for the presence of charge inhomogeneity on colloidal beads. Since colloidal particles change orientation due to thermal motion, surface charge inhomogeneity would influence the stability [FV02] and structure of colloids. In particular, since the here used technique, unlike other techniques for surface force measurement, is sensitive to the distribution of surface charges, the technique could be used to investigate the effect of charge inhomogeneity on colloidal stability.

An alternative approach to determine the surface forces experienced by a colloidal bead is the analysis of the bead's thermal motion. I could demonstrate that with the here presented instrument the monitoring of a colloidal bead's thermal motion at high hydrostatic pressure with nanometer resolution is possible. This resolution is comparable to state of the art techniques like total internal reflection microscopy [Vol+10]. Monitoring thermal motion with such distance resolution enables the study of a multitude of interactions, like van der Waals interactions [BP99] or critical Casimir forces [Her+08] at high hydrostatic pressure. Furthermore, by investigation of thermal motion, the force resolution of the developed instrument could be improved down to the femtonewton range [Pri99; Vol+09].

The geometry of the here presented instrument allows the use of a wide variety of optical cells. In particular, diamond anvil cells could be used [MB74; Lov12], thus giving the possibility to exceed the accessible pressure range. Furthermore, other optical high-pressure cells also allow for the control of temperature [ADT01; DT02; Vas+10]. Using such a cell, a long-range repulsion between silica spheres in supercritical ethanol (critical point at 61 bar and 241 °C) was observed by means of optical microscopy [Muk+14]. The here presented instrument could be used to quantify the observed repulsion and overall deepen the insight into colloidal behavior in supercritical fluids.

Bibliography

[ADT01] R. Alargova, S Deguchi, and K Tsujii. "Dynamic light scattering study of polystyrene latex suspended in water at high temperatures and high pressures". English. In: *Colloids and Surfaces A: Physicochemical and Engineering Aspects* 183 (2001), pp. 303–312.

[Ald+88] N. J. Alderman, A. Gavignet, D. Guillot, and G. C. Maitland. "High-Temperature, High-Pressure Rheology of Water-Based Muds". In: *Proceedings of SPE Annual Technical Conference and Exhibition*. Society of Petroleum Engineers, Oct. 1988, pp. 187–195.

[AP87] B. M. Alexander and D. C. Prieve. "A Hydrodynamic Technique for Measurement of Colloidal Forces". In: *Langmuir* 3 (1987), pp. 788–795.

[AOS11] A. Amiri, G. Oye, and J. Sjoblom. "Temperature and pressure effects on stability and gelation properties of silica suspensions". In: *Colloids and Surfaces A: Physicochemical and Engineering Aspects* 378 (2011), pp. 14–21.

[AP93] M. I. Angelova and B. Pouligny. "Trapping and levitation of a dielectric sphere with off-centred Gaussian beams. I. Experimental". In: *Pure and Applied Optics* 2 (1993), pp. 261–276.

[Ash70] A. Ashkin. "Acceleration and Trapping of Particles by Radiation Pressure". In: *Physical Review Letters* 24 (1970), pp. 156–159.

[Ash92] A. Ashkin. "Forces of a single-beam gradient laser trap on a dielectric sphere in the ray optics regime". In: *Biophysical Journal* 61 (1992), pp. 569–582.

[AD71] A. Ashkin and J. M. Dziedzic. "Optical Levitation by Radiation Pressure". In: *Applied Physics Letters* 19 (1971), pp. 283–285.

[Ash+86] A. Ashkin, J. M. Dziedzic, J. E. Bjorkholm, and S. Chu. "Observation of a single-beam gradient force optical trap for dielectric particles". In: *Optics Letters* 11 (1986), pp. 288–290.

[Bao+10] C. M. Bao, Y. Gai, K. K. Lou, C. Y. Jiang, and S. M. Ye. "High-hydrostatic-pressure optical chamber system for cultivation and microscopic observation of deep-sea organisms". In: *Aquatic Biology* 11 (2010), pp. 157–162.

[BVS09] D. P. J. Barz, M. J. Vogel, and P. H. Steen. "Determination of the Zeta Potential of Porous Substrates by Droplet Deflection. I. The Influence of Ionic Strength and pH Value of an Aqueous Electrolyte in Contact with a Borosilicate Surface". In: *Langmuir* 25 (2009), pp. 1842–1850.

[BG01] S. H. Behrens and D. G. Grier. "The charge of glass and silica surfaces". In: *The Journal of Chemical Physics* 115 (2001), pp. 6716–6721.

[BP99] M. A. Bevan and D. C. Prieve. "Direct Measurement of Retarded van der Waals Attraction". In: *Langmuir* 15 (1999), pp. 7925–7936.

[Bow+13a] R. W. Bowman, G. M. Gibson, M. J. Padgett, F. Saglimbeni, and R. Di Leonardo. "Optical Trapping at Gigapascal Pressures". In: *Physical Review Letters* 110 (2013), p. 095902.

[Bow+13b] R. W. Bowman, F. Saglimbeni, G. M. Gibson, R. Di Leonardo, and M. J. Padgett. "Implementing optical tweezers at high pressure in a diamond anvil cell". In: *Proc. of SPIE*. Ed. by J. Glückstad, D. L. Andrews, and E. J. Galvez. Vol. 8637. Complex Light and Optical Forces VII. Mar. 2013, p. 863718.

[Bre61] H. Brenner. "The slow motion of a sphere through a viscous fluid towards a plane surface". In: *Chemical Engineering Science* 16 (1961), pp. 242–251.

[BS90] M. A. Brown and E. J. Staples. "Measurement of absolute particle-surface separation using total internal reflection microscopy and radiation pressure forces". In: *Langmuir* 6 (1990), pp. 1260–1265.

[But91a] H.-J. Butt. "Electrostatic interaction in atomic force microscopy". In: *Biophysical Journal* 60 (1991), pp. 777–785.

[But91b] H.-J. Butt. "Measuring electrostatic, van der Waals, and hydration forces in electrolyte solutions with an atomic force microscope". In: *Biophysical Journal* 60 (1991), pp. 1438–1444.

[BK10] H.-J. Butt and M. Kappl. *Surface and interfacial forces*. Weinheim: Wiley-VCH, 2010.

[CH85] D. Y. C. Chan and R. G. Horn. “The drainage of thin liquid films between solid surfaces”. In: *The Journal of Chemical Physics* 83 (1985), pp. 5311–5324.

[Che+09] W. Chen, S. Tan, Y. Zhou, T.-K. Ng, W. T. Ford, and P. Tong. “Attraction between weakly charged silica spheres at a water-air interface induced by surface-charge heterogeneity”. In: *Physical Review E* 79 (2009), p. 041403.

[Chi+03] E. Y. Chi, S. Krishnan, T. W. Randolph, and J. F. Carpenter. “Physical Stability of Proteins in Aqueous Solution: Mechanism and Driving Forces in Nonnative Protein Aggregation”. In: *Pharmaceutical Research* 20 (2003), pp. 1325–1336.

[CD01] A. R. Clapp, and R. B. Dickinson. “Direct Measurement of Static and Dynamic Forces between a Colloidal Particle and a Flat Surface Using a Single-Beam Gradient Optical Trap and Evanescent Wave Light Scattering”. In: *Langmuir* 17 (2001), pp. 2182–2191.

[CB67] R. G. Cox and H. Brenner. “The slow motion of a sphere through a viscous fluid towards a plane surface - II Small gap widths, including inertial effects”. In: *Chemical Engineering Science* 22 (1967), pp. 1753–1777.

[DB11] M. J. Dabney and F. V. Bright. “High-Pressure Total Internal Reflection Fluorescence Apparatus”. In: *Applied Spectroscopy* 65 (2011), pp. 1233–1239.

[DM09] S. Deguchi and S. A. Mukai. “Comment on "Effect of Pressure on Colloidal Behavior in Hydrothermal Water"”. In: *Journal of Physical Chemistry B* 113 (2009), pp. 3251–3252.

[DT02] S. Deguchi and K. Tsujii. “Flow cell for in situ optical microscopy in water at high temperatures and pressures up to supercritical state”. In: *Review of Scientific Instruments* 73 (2002), pp. 3938–3941.

[Deg+06] S. Deguchi, S. K. Ghosh, R. G. Alargova, and K. Tsujii. “Viscosity measurements of water at high temperatures and pressures using dynamic light scattering”. In: *Journal of Physical Chemistry B* 110 (2006), pp. 18358–18362.

[Dor03] G. Dornheim. *Wear-resistant, progressive working sealing bond for high static and dynamic pressures, comprises a piston and a cylinder tube, piston being drilled at its front so that a desired extension place is formed*. German Gebrauchsmuster DE 202 12 219 U 1. Feb. 2003.

[DSP91] W. A. Ducker, T. J. Senden, and R. M. Pashley. “Direct Measurement of Colloidal Forces Using an Atomic Force Microscope”. In: *Nature* 353 (1991), pp. 239–241.

[Bri] *Encyclopædia Britannica*. "Drilling mud" `http://www.britannica.com/technology/drilling-mud` (retrieved February 12th, 2016). Encyclopædia Britannica Inc., 2016.

[FV02] J. D. Feick and D. Velegol. “Measurements of Charge Nonuniformity on Polystyrene Latex Particles”. In: *Langmuir* 18 (2002), pp. 3454–3458.

[FCBC11] H. P. Fernandes, C. L. Cesar, and M. d. L. Barjas-Castro. “Electrical properties of the red blood cell membrane and immunohematological investigation”. In: *Revista Brasileira de Hematologia e Hemoterapia* 33 (2011), pp. 297–301.

[FN04] W. B. Floriano and M. A. C. Nascimento. “Dielectric constant and density of water as a function of pressure at constant temperature”. In: *Brazilian Journal of Physics* 34 (2004), pp. 38–41.

[FM06] P. F. Fox and P. L. H. McSweeney, eds. *Advanced dairy chemistry*. Vol. 2, Lipids. New York, N.Y.: Springer, 2006.

[Fre+06] B. Frey, M. Hartmann, M. Herrmann, R. Meyer-Pittroff, K. Sommer, and G. Bluemelhuber. “Microscopy under pressure - An optical chamber system for fluorescence microscopic analysis of living cells under high hydrostatic pressure”. In: *Microscopy Research and Technique* 69 (2006), pp. 65–72.

[GXX12] Z. Gan, X. Xing, and Z. Xu. “Effects of image charges, interfacial charge discreteness, and surface roughness on the zeta potential of spherical electric double layers”. In: *The Journal of Chemical Physics* 137, 034708 (2012), pp. –.

[Gho09] S. K. Ghosh. “Reply to "Comment on ’Effect of Pressure on Colloidal Behavior in Hydrothermal Water"’: Role of pK(w) on the Dispersion Stability of Colloids in Hydrothermal Water”. In: *Journal of Physical Chemistry B* 113 (2009), pp. 3253–3255.

[GT08] S. K. Ghosh and K. Tsujii. “Effect of pressure on colloidal behavior in hydrothermal water”. In: *Journal of Physical Chemistry B* 112 (2008), pp. 6906–6913.

[GHD] T. Goulette, C. D. Howard, and M. W. Davidson. *Infinity Optical Systems*. `http://www.microscopyu.com/articles/optics/cfintro.html` (retrieved February 8th, 2016).

[Gri97] D. G. Grier. "Optical tweezers in colloid and interface science". In: *Current Opinion in Colloid & Interface Science* 2 (1997), pp. 264–270.

[HB83] J. Happel and H. Brenner. *Low Reynolds number hydrodynamics : with special applications to particulate media*. The Hague; Boston; Hingham, MA, USA: M. Nijhoff ; Distributed by Kluwer Boston, 1983.

[HKS04] M. Hartmann, M. Kreuss, and K. Sommer. "High pressure microscopy - A powerful tool for monitoring cells and macromolecules under high hydrostatic pressure". In: *Cellular and Molecular Biology* 50 (2004), pp. 479–484.

[Har+03] M. Hartmann, F. Pfeifer, G. Dornheim, and K. Sommer. "High pressure cell for observing microscopic processes under high pressure". In: *Chemie Ingenieur Technik* 75 (2003), pp. 1763–1767.

[Her+08] C. Hertlein, L. Helden, A. Gambassi, S. Dietrich, and C. Bechinger. "Direct measurement of critical Casimir forces". English. In: *Nature* 451 (2008), pp. 172–175.

[HR97] P. C. Hiemenz and R. Rajagopalan. *Principles of Colloid and Surface Chemistry*. Third. New York: Marcel Dekker, 1997.

[IT72] J. N. Israelachvili and D. Tabor. "The Measurement of Van Der Waals Dispersion Forces in the Range 1.5 to 130 nm". In: *Proceedings of the Royal Society of London, Series A* 331 (1972), pp. 19–&.

[Isr11] J. N. Israelachvili. *Intermolecular and surface forces*. San Diego, Calif.: Elsevier Science Publ., 2011.

[JB13] D. L. Jing and B. Bhushan. "Quantification of Surface Charge Density and Its Effect on Boundary Slip". In: *Langmuir* 29 (2013), pp. 6953–6963.

[JZ08] A. Jonáš and P. Zemánek. "Light at work: The use of optical forces for particle manipulation, sorting, and analysis". In: *ELECTROPHORESIS* 29 (2008), pp. 4813–4851.

[KL] G. W. C. Kaye and T. H. Laby. *Tables of Physical & Chemical Constants (16th edition 1995). 2.2.2 Elasticities and strengths.* Kaye & Laby Online. Version 1.0 (2005). `http://www.kayelaby.npl.co.uk/general_physics/2_2/2_2_2.html` (retrieved February 3rd, 2016).

[Kep94] P. E. Kepkay. "Particle aggregation and the biological reactivity of colloids". In: *Marine Ecology Progress Series* 109 (1994), pp. 293–304.

[Köh93] A. Köhler. "Ein neues Beleuchtungsverfahren für mikrophotographische Zwecke". In: *Zeitschrift für wissenschaftliche Mikroskopie und für Mikroskopische Technik* 10 (1893), pp. 433–440.

[KC12] J. Koo and C. Czeslik. "High pressure sample cell for total internal reflection fluorescence spectroscopy at pressures up to 2500 bar". In: *Review of Scientific Instruments* 83 (2012), p. 085109.

[KPD06] P. Kraikivski, B. Pouligny, and R. Dimova. "Implementing both short- and long-working-distance optical trappings into a commercial microscope". In: *Review of Scientific Instruments* 77 (2006), p. 113703.

[Lam+08] F. S. Lameiras, A. L. d. Souza, V. A. R. d. Melo, E. H. M. Nunes, and I. D. Braga. "Measurement of the zeta potential of planar surfaces with a rotating disk". en. In: *Materials Research* 11 (2008), pp. 217 –219.

[LMF] E. Lemmon, M. McLinden, and D. Friend. "Thermophysical Properties of Fluid Systems". In: *NIST Chemistry WebBook, NIST Standard Reference Database Number 69*. Ed. by P. J. Linstrom and W. G. Mallard. `http://webbook.nist.gov` (retrieved March 30, 2015). National Institute of Standards and Technology, Gaithersburg MD, 20899.

[LS09] L. Limozin and K. Sengupta. "Quantitative Reflection Interference Contrast Microscopy (RICM) in Soft Matter and Cell Adhesion". In: *ChemPhysChem* 10 (2009), pp. 2752–2768.

[Lov12] J. Loveday, ed. *High-Pressure Physics*. Boca Raton, FL: CRC Press, 2012.

[MB74] L. Merrill and W. A. Bassett. "Miniature diamond anvil pressure cell for single crystal x-ay diffraction studies". In: *Review of Scientific Instruments* 45 (1974), pp. 290–294.

[MDLP11] M. de Messieres, N. A. Denesyuk, and A. La Porta. "Noise associated with nonconservative forces in optical traps". In: *Physical Review E* 84 (2011), p. 031108.

[MLP12] B. M. Mihiretie, J. C. Loudet, and B. Pouligny. "Optical levitation and long-working-distance trapping: From spherical up to high aspect ratio ellipsoidal particles". In: *Journal of Quantitative Spectroscopy and Radiative Transfer* 126 (2012), pp. 61–68.

[Mih+12] B. M. Mihiretie, P. Snabre, J. C. Loudet, and B. Pouligny. "Radiation pressure makes ellipsoidal particles tumble". In: *EPL (Europhysics Letters)* 100 (2012), p. 48005.

[MP02] J. E. Molloy and M. J. Padgett. "Lights, action: optical tweezers". In: *Contemporary Physics* 43 (2002), pp. 241–258.

[Moz+96] V. V. Mozhaev, K. Heremans, J. Frank, P. Masson, and C. Balny. "High pressure effects on protein structure and function". In: *Proteins-Structure Function and Genetics* 24 (1996), pp. 81–91.

[MDT06] S. Mukai, S. Deguchi, and K. Tsujii. "A high-temperature and -pressure microscope cell to observe colloidal behaviors in subcritical and supercritical water: Brownian motion of colloids near a wall". In: *Colloids and Surfaces A: Physicochemical and Engineering Aspects* 282-283 (2006), pp. 483–488.

[Muk+14] S. Mukai, T. Koyama, K. Tsujii, and S. Deguchi. "Anomalous long-range repulsion between silica surfaces induced by density inhomogeneities in supercritical ethanol". In: *Soft Matter* 10 (2014), pp. 6645–6650.

[Nad+01] F. Nadal, A. Dazzi, F. Argoul, and B. Pouligny. "Probing the confined dynamics of a spherical colloid close to a surface by combined optical trapping and reflection interference contrast microscopy". In: *Applied Physics Letters* 79 (2001), pp. 3887–3889.

[NAB13] M. Nayeri, Z. Abbas, and J. Bergenholtz. "Measurements of screening length in salt solutions by total internal reflection microscopy: Influence of van der Waals forces and instrumental noise". In: *Colloids and Surfaces A: Physicochemical and Engineering Aspects* 429 (2013), pp. 74 –81.

[NB04] K. C. Neuman and S. M. Block. "Optical trapping". In: *Review of Scientific Instruments* 75 (2004), pp. 2787–2809.

[OP04] P. C. Odiachi and D. C. Prieve. "Removing the effects of additive noise from TIRM measurements". In: *Journal of Colloid and Interface Science* 270 (2004), pp. 113–122.

[OW05] R. J. Oetama and J. Y. Walz. "A new approach for analyzing particle motion near an interface using total internal reflection microscopy". In: *Journal of Colloid and Interface Science* 284 (2005), pp. 323–331.

[PG72] V. Parsegian and D. Gingell. "On the Electrostatic Interaction across a Salt Solution between Two Bodies Bearing Unequal Charges". In: *Biophysical Journal* 12 (1972), pp. 1192 –1204.

[PWC14] D. F. Parsons, R. B. Walsh, and V. S. J. Craig. "Surface forces: Surface roughness in theory and experiment". In: *The Journal of Chemical Physics* 140, 164701 (2014), p. 164701.

[Pil+16] D. W. Pilat, B. Pouligny, A. Best, T. A. Nick, R. Berger, and H.-J. Butt. "Surface forces between colloidal particles at high hydrostatic pressure". In: *Physical Review E* 93 (2016), p. 022608.

[PLL87] D. C. Prieve, F. Luo, and F. Lanni. "Brownian Motion of a Hydrosol Particle in a Colloidal Force Field". In: *Faraday Discussions* 83 (1987), pp. 297–307.

[Pri99] D. Prieve. "Measurement of colloidal forces with TIRM." English. In: *Advances in Colloid and Interface Science* 82 (Oct. 1999), pp. 93–125.

[PF90] D. C. Prieve and N. A. Frej. "Total internal reflection microscopy: a quantitative tool for the measurement of colloidal forces". In: *Langmuir* 6 (1990), pp. 396–403.

[Rab+06] E. C. Raber, J. A. Dudley, M. Salerno, and P. Urayama. "Capillary-based, high-pressure chamber for fluorescence microscopy imaging". In: *Review of Scientific Instruments* 77 (2006), p. 096106.

[RS92] J. Radler and E. Sackmann. "On the Measurement of Weak Repulsive and Frictional Colloidal Forces by Reflection Interference Contrast Microscopy". In: *Langmuir* 8 (1992), pp. 848–853.

[Rec+98] T. Reck, E. Sautter, W. Dollhopf, and W. Pechhold. "A high-pressure cell for optical microscopy and measurements on the phase diagram of poly(diethylsiloxane)". In: *Review of Scientific Instruments* 69 (1998), pp. 1823–1827.

[Ren14] K. F. Ren. *ABSPhere Version 1.10*. Computer Program. Available at `https://amocops.univ-rouen.fr/en/content/download`. 2014.

[RGG94] K. F. Ren, G. Gréha, and G. Gouesbet. "Radiation pressure forces exerted on a particle arbitrarily located in a Gaussian beam by using the generalized Lorenz-Mie theory, and associated resonance effects". In: *Optics Communications* 108 (1994), pp. 343–354.

[RA06] K. Rodríuez and M. Araujo. "Temperature and pressure effects on zeta potential values of reservoir minerals". In: *Journal of Colloid and Interface Science* 300 (2006), pp. 788–794.

[Roi+08] Y. Roichman, B. Sun, A. Stolarski, and D. G. Grier. "Influence of Nonconservative Optical Forces on the Dynamics of Optically Trapped Colloidal Spheres: The Fountain of Probability". In: *Physical Review Letters* 101 (2008), p. 128301.

[Sch+90] P. Schiebener, J. Straub, J. M. H. Levelt Sengers, and J. S. Gallagher. "Refractive index of water and steam as function of wavelength, temperature and density". In: *Journal of Physical and Chemical Reference Data* 19 (1990), pp. 677–717.

[SH11] E. Schurtenberger and M. Heuberger. "The extended surface forces apparatus. IV. Precision static pressure control". In: *Review of Scientific Instruments* 82 (2011), p. 103902.

[SH12] E. Schurtenberger and M. Heuberger. "Supercritical Casimir effect in carbon dioxide". In: *The Journal of Supercritical Fluids* 71 (2012), pp. 120–126.

[Sel83] S. A. Self. "Focusing of spherical Gaussian beams". In: *Applied Optics* 22 (1983), pp. 658–661.

[Sho+00] D. S. Sholl, M. K. Fenwick, E. Atman, and D. C. Prieve. "Brownian dynamics simulation of the motion of a rigid sphere in a viscous fluid very near a wall". In: *The Journal of Chemical Physics* 113 (2000), pp. 9268–9278.

[SD] K. R. Spring and M. W. Davidson. *Depth of Field and Depth of Focus*. `http://www.microscopyu.com/articles/formulas/formulasfielddepth.html` (retrieved April 8th, 2016).

[Sur+13] E. Suraniti, F. Kanoufi, C. Gosse, X. Zhao, R. Dimova, and N. Pouligny B.and Sojic. "Electrochemical Detection of Single Microbeads Manipulated by Optical Tweezers in the Vicinity of Ultramicroelectrodes". In: *Analytical Chemistry* 85 (2013), pp. 8902–8909.

[SW97] L. Suresh and J. Y. Walz. "Direct Measurement of the Effect of Surface Roughness on the Colloidal Forces between a Particle and Flat Plate". In: *Journal of Colloid and Interface Science* 196 (1997), pp. 177 –190.

[TS69] D. Tabor and W. H. S. "The Direct Measurement of Normal and Retarded van der Waals Forces". In: *Proceedings of the Royal Society of London, Series A* 312 (1969), pp. 435–450.

[Wor] *The World Factbook*. `https://www.cia.gov/library/publications/the-world-factbook/index.html` (retrieved February 11th, 2016). Washington, DC: Central Intelligence Agency, 2013, 2013-14.

[UF80] M. Uematsu and E. U. Franck. "Static Dielectric Constant of Water and Steam". In: *Journal of Physical and Chemical Reference Data* 9 (1980), pp. 1291–1306.

[Vas+10] H. Vass, S. L. Black, E. M. Herzig, F. B. Ward, P. S. Clegg, and R. J. Allen. "A multipurpose modular system for high-resolution microscopy at high hydrostatic pressure". In: *Review of Scientific Instruments* 81 (2010), p. 053710.

[Vas+13] H. Vass, S. L. Black, C. Flors, D. Lloyd, F. B. Ward, and R. J. Allen. "Single-molecule imaging at high hydrostatic pressure". In: *Applied Physics Letters* 102 (2013), p. 154103.

[VO48] E. J. W. Verwey and J. T. G. Overbeek. *Theory of the stability of lyophobic colloids*. New York: Elsevier Publishing Inc., 1948.

[Vol+09] G. Volpe, T. Brettschneider, L. Helden, and C. Bechinger. "Novel perspectives for the application of total internal reflection microscopy". In: *Optics Express* 17 (2009), pp. 23975–23985.

[Vol+10] G. Volpe, L. Helden, T. Brettschneider, J. Wehr, and C. Bechinger. "Influence of Noise on Force Measurements". In: *Physical Review Letters* 104 (2010), p. 170602.

[WSP99] J. Walz, L. Suresh, and M. Piech. "The Effect of Nanoscale Roughness on Long Range Interaction Forces". In: *Journal of Nanoparticle Research* 1 (1999), pp. 99–113.

[WG93] M. L. Wells and E. D. Goldberg. "Colloid aggregation in seawater". In: *Marine Chemistry* 41 (1993), pp. 353–358.

[WG94] M. L. Wells and E. D. Goldberg. "The distribution of colloids in the North Atlantic and Southern Oceans". In: *Limnology and Oceanography* 39 (1994), pp. 286–302.

[WG91] M. L. Wells and E. D. Goldberg. "Occurrence of small colloids in sea water". In: *Nature* 353 (1991), pp. 342–344.

[Wir+14] F. J. Wirkert, M. Paulus, J. Nase, J. Moller, S. Kujawski, C. Sternemann, and M. Tolan. "X-ray reflectivity measurements of liquid/solid interfaces under high hydrostatic pressure conditions". In: *Journal of Synchrotron Radiation* 21 (2014), pp. 76–81.

[Yan+14] P. H. Yancey, M. E. Gerringer, J. C. Drazen, A. A. Rowden, and A. Jamieson. "Marine fish may be biochemically constrained from inhabiting the deepest ocean depths". In: *Proceedings of the National Academy of Sciences* 111 (2014), pp. 4461–4465.

[ZSB01] Z. Zhou, P. J. Scales, and D. V. Boger. "Chemical and physical control of the rheology of concentrated metal oxide suspensions". In: *Chemical Engineering Science* 56 (2001), pp. 2901–2920.

[Zwo+08] P. J. van Zwol, G. Palasantzas, M. van de Schootbrugge, J. T. M. de Hosson, and V. S. J. Craig. "Roughness of microspheres for force measurements". In: *Langmuir* 24 (2008), pp. 7528–7531.